Investigations of the Electronic, Vibrational and Structural Properties of Single and Few-Layer Graphene

Chun Hung Lui

Submitted in partial fulfillment of the

requirements for the degree

of Doctor of Philosophy

in the Graduate School of Arts and Sciences

COLUMBIA UNIVERSITY

2011

ABSTRACT

Investigations of the Electronic, Vibrational and Structural Properties of
Single and Few-Layer Graphene

Chun Hung Lui

Single and few-layer graphene (SLG and FLG) have stimulated great scientific interest because of their distinctive properties and potential for novel applications. In this dissertation, we investigate the mechanical, electronic and vibrational properties of these remarkable materials by various techniques, including atomic-force microscopy (AFM) and Raman, infrared (IR), and ultrafast optical spectroscopy.

With respect to its mechanical properties, SLG is known to be capable of undergoing significant mechanical deformation. We have applied AFM to investigate how the morphology of SLG is influenced by the substrate on which it is deposited. We have found that SLG is strongly affected by the morphology of the underlying supporting surface. In particular, SLG deposited on atomically flat surfaces of mica substrates exhibits an ultraflat morphology, with height variation essentially indistinguishable from that observed for the surface of cleaved graphite.

One of the most distinctive aspects of SLG is its spectrum of electronic excitations, with its characteristic linear energy-momentum dispersion relation. We have examined the dynamics of the corresponding Dirac fermions by optical emission spectroscopy. By analyzing the spectra of light emission induced in the spectral visible range by 30-femtosecond laser pulses, we find that the charge carriers in graphene cool

by the emission of strongly coupled optical phonons in a few 10's of femtoseconds and thermalize among themselves even more rapidly. The charge carriers and the strongly coupled optical phonons are thus essentially in thermal equilibrium with one another on the picosecond time scale, but can be driven strongly out of equilibrium with the other phonons in the system. Temperatures exceeding 3000 K are achieved for the subsystem of the charge carriers and optical phonons under femtosecond laser excitation.

While SLG exhibits remarkable physical properties, its few-layer counterparts are also of great interest. In particular, FLG can exist in various crystallographic stacking sequences, which strongly influence the material's electronic properties. We have developed an accurate and convenient method of characterizing stacking order in FLG using the lineshape of the Raman 2D-mode. Raman imaging allows us to visualize directly the spatial distribution of Bernal (ABA) and rhombohedral (ABC) stacking in trilayer and tetralayer graphene. We find that 15% of exfoliated graphene trilayers and tetralayers are comprised of micrometer-sized domains of rhombohedral stacking, rather than of usual Bernal stacking.

The accurate identification of stacking domains in FLG allows us to investigate the influence of stacking order on the material's electronic properties. In particular, we have studied by means of IR spectroscopy the possibility of opening a band gap by the application of a strong perpendicular electric field in trilayer graphene. We observe an electrically tunable band gap exceeding 100 meV in ABC trilayers, while no band gap is found for ABA trilayers. We have also studied the influence of layer thickness and stacking order on the Raman response of the out-of-plane vibrations in FLG. We observe a Raman combination mode that involves the layer-breathing vibrations in FLG. This

Raman mode is absent in SLG and exhibits a lineshape that depends sensitively on both the material's layer thickness and stacking sequence.

Contents

iv

List of Figures

List of Tables

Acknowledgements

The experience of my phD program has been sweet and bountiful. Though the training was tough, the process has been enjoyable. I feel satisfied and grateful. I am heartily thankful to my supervisor Prof. Tony Heinz. He has offered me the best environment and supervision to train me as an independent researcher. He not only teaches me much knowledge in physics, but also presents to me a good style and attitude to conduct scientific research. He is very kind and considerate towards me. I feel blessed to have joint his group. I also owe my gratitude to my Mphil supervisor Prof. Michael Loy, who recommended me to the Heinz group. He gives me much scientific as well as spiritual support during my phD program.

I am deeply indebted to Dr. Kin Fai Mak, who is my best friend, colleague and also my mentor. He gives me much encouragement, support and guidance throughout my undergraduate, Mphil and my whole phD program. He has introduced me to the research of graphene and helped me develop an understanding on this subject. He has taught me many important experimental techniques and shared a lot of inspiring ideas on my research. Much of the research in my dissertation has been conducted based on his pioneer works on the optical spectroscopy of graphene.

I feel very fortunate to have collaborated with many talented scientists in Columbia University. I thank Dr. Li Liu for his important technical assistance in the AFM experiments. I am also grateful to his supervisor Prof. George Flynn. Their technical and intellectual support has made my research of ultraflat graphene very successful. This first work, one fortunately published in *Nature*, has been a great

encouragement to me to move on in the research. I am thankful to my long-time collaborator Dr. Zhiqiang Li, who has offered me much help in the sample preparation, experiments, data analysis and writing the manuscripts of the infrared spectroscopy of few-layer graphene. I am grateful to Zheyuan Chen and his supervisor Prof. Louis Brus for their support on the Raman spectroscopy of few-layer graphene. Besides, I would like to thank Prof. Jie Shan, Prof. Davide Boschetto, Dr. Leandro Malard, Dr. Yuhei Miyauchi, Prof. Ernst Knoesel, Prof. Emmanuele Cappelluti and Prof. Riichiro Saito. It has been a happy and fruitful time to work with them together.

I would like to thank my teachers: Prof. Igor Aleiner, Prof. Allan Blaer, Prof. Norman Christ, Prof. Boris Altshuler and Prof. Robert Mawhinney. I have learnt a lot from their classes. I also gratefully acknowledge my phD defense committee: Prof. Philip Kim, Prof. Igor Aleiner, Prof. James Hone and Prof. Richard Osgood.

Further, I would like to thank the following collaborators and colleagues. I cherish my experience with them: Dr. Hugen Yan, Dr. Donghua Song, Dr. Yang Wu, Dr. Joanna Atkin, Hui Zhou, Prof. Zonghai Hu, Prof. Feng Wang, Dr. Stéphane Berciaud, Dr. Ioannis Chatzakis, Dr. Theanne Schiros, Dr. Janina Maultzsch, Dr.Christophe Voisin, Dr. Sami Rosenblatt, Eric Newton, Paul Klimov, Gabriel Lantz, François Laverge, SukHyun Kim, Yilei Li, Dr. Daejin Eom, Dr. Sunmin Ryu, Dr. Shu Li, Naeyoung Jung, Kevin Knox, Dr. Cory Dean, Andrea Young, Yue Zhao, Dmitri Efetov, Dr. Young-Jun Yu, Hechen Ren, Dr. Jun Yan, Zhengyi Zhang, Lei Wang, Dr. Yi Rao, Liuyan Zhao, Dr. Changgu Lee, Dr. Chengguang Lu, Dr. Larry Carr, Randy Smith, Geoff Goold, Linus Fetter, Prof. Jeremy Dodd, Lalla Grimes, Rasma Mednis and Giuseppina Cambareri.

Finally, I owe my gratitude to all the brothers and sisters in the Church. Their love and care towards me has made my life full of joy and grace. I am deeply grateful to my parents and my older brother for their long-lasting love to me. I am especially indebted to my mom, who has raised me up and devoted her life to my education.

Chapter 1

Introduction

Graphene is a single layer of sp^2-bonded carbon atoms arranged in a two-dimensional (2D) honeycomb lattice. This material possesses distinctive electronic, optical, vibrational and mechanical properties and shows huge potential for novel applications [1,2]. In this chapter, I review briefly the history of graphene research and the panoply of distinctive properties of graphene. Afterward, I introduce some elementary electronic and vibrational properties of graphene as well as the ultrafast dynamics of charge carriers in graphene. Finally, I present recent research on the structure of graphene, including the influence of graphene's morphology on the material's physical and chemical properties.

1.1 A Brief History of Graphene

While majority of graphene research were initiated after 2000, pioneer studies of graphene actually date back to more than half a century ago. Wallace's paper in 1947 [3] for the first time calculated the electronic structure of graphene and highlighted its linear dispersion near the K point of the Brillouin zone. Later theoretical studies also remarked on graphene's unusual charge carriers that mimic massless Dirac fermions and predicted relativistic-like effects in this two-dimensional condensed matter system, such as the

unusual landau levels under magnetic field [4,5]. On the other hand, experimental studies of graphene date back to early 1960's. The first observation of single layer graphene can be attributed to Boehm's pioneer work in 1962 [6]. By using reduced graphite oxide, Boehm *et al* produced free-standing ultrathin graphite flakes in solutions, which could be transferred to a thin membrane and visualized directly with a transmission electron microscope (TEM). Some of these graphite flakes were found to be of only few-layer or even single-layer thickness. Boehm also formally defined the term "graphene" in 1994 [7]. Other research groups also observed ultrathin graphite layers under different conditions [8-10]. However, due to various technical difficulties, these early experiments on graphene were mainly observational, and did not reveal substantially the unique electronic properties of graphene. Starting from 2000, several research groups strived to produce graphene samples that could be put into electrical measurements [11-13]. For instance, Walt de Heer and collaborators in Georgia Institute of Technology tried to grow graphene epitaxially from SiC substrates [12]; Philip Kim and collaborators in Columbia University tried to exfoliate graphene by mounting the graphite crystal on an atomic-force-microscope (AFM) tip and dragging it along a surface [14]. The breakthrough finally came in 2005, when the Geim-Novoselov group in Manchester University used a simple adhesive-tape method to successfully isolate the single-layer graphene from bulk graphite [15]. Very importantly, they deposited graphene on silicon substrates with a well-designed 300-nm-thick oxide layer. The optical interference in the oxide layer allowed the one-atom-thick graphene sheet to be visible in the optical microscope (see Figure 1.1, with the STM image of graphene [16]). This extremely simple sample preparation and characterization method significantly accelerated the graphene research.

In 2005, the Manchester group and Columbia group demonstrated unambiguously the two-dimensional massless Dirac fermions in graphene in two back-to-back papers in Nature [17,18], which formally sparked the graphene gold rush. The development of graphene research was rapid. Many breakthroughs were made in a short period of time [1,2]. The experiments had not only confirmed various predictions on graphene's usual electronic properties, but also discovered many unexpected novel characteristics of the material. The Nobel Prize in physics was given to A.K. Geim and K.S. Novoselov in 2010 for their pioneer contributions in graphene research. The award was also the best confirmation on the impact of graphene on science and technology.

(a) (b)
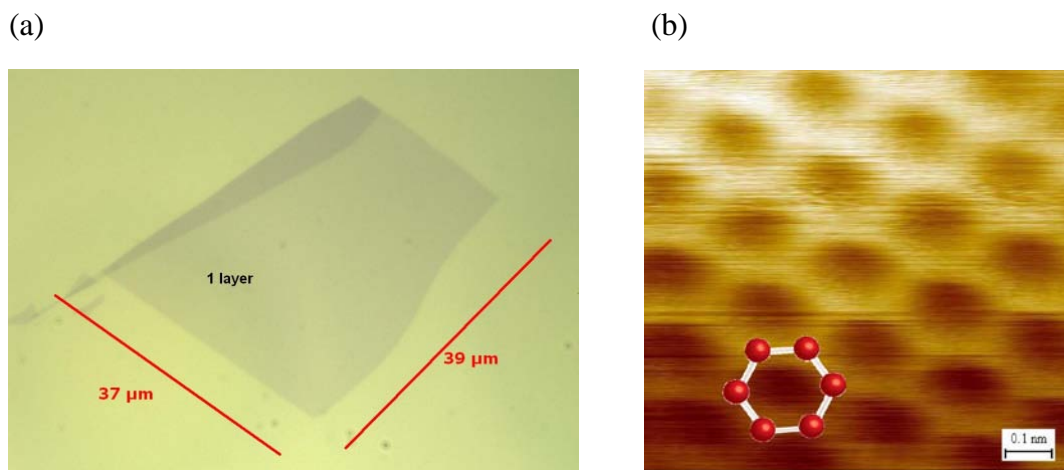
Figure 1.1 (a) Optical image of a single-layer graphene sample deposited on a silicon substrate coated with a 300-nm-thick oxide layer. **(b)** The honeycomb lattice of graphene shown in the topographic image of Scanning Tunneling Microscopy (STM). Figure (b) is adapted from ref.[16] .

1.2 Overview of Graphene's Novelties

Electronic Properties Graphene consists of only one layer of carbon atoms and thus serves as an excellent platform for studies of 2D charge carriers. Beside the special

dimensionality, graphene's low-energy charge carriers are effectively described by a Dirac-like Hamiltonian, instead of the Schrödinger equation in conventional semiconductors. The quasiparticles in graphene are massless Dirac fermions with linear energy dispersion [17-19]. They travel with a constant speed and, thus, behave like "photons" in a solid. The peculiar charge carriers in graphene make some relativistic effects observable even in a condensed-matter system. For instance, graphene exhibits an anomalous quantum Hall effect (QHE) that shows conductivity plateaus at half-integer positions [4,5,17,18], a feature due to the unusual Landau levels of ultra-relativistic particles. In addition, a counter-intuitive phenomenon called Klein tunneling of relativistic particles [20], *i.e.* complete transmission over high and wide potential barriers, can be realized in graphene [21,22]. This makes the charge carriers in graphene insensible to the potentials induced by the impurities and disorder. On the other hand, graphene has excellent crystalline quality, partly due to its strong carbon-carbon bonding that makes defect formation energetically unfavorable. The strong atomic bonds also bestow graphene with high-energy optical phonons (~200 meV), which are mostly frozen in room temperature. The combination of the lack of back scattering, low defect density and the absence of optical phonons bestows graphene with the highest room-temperature carrier transport mobility (μ>200,000 cm^2/Vs) among all the semiconductors [23,24]. The charge carriers in graphene can travel for a few micrometers without any scattering. The carriers' ultrahigh mobility and relativistic-like nature enables integer QHE to be observable in graphene even in room temperature [25] (Figure 1.2), and also enables fractional QHE to be observable in less extreme conditions [26,27]. Finally, the spin-orbit
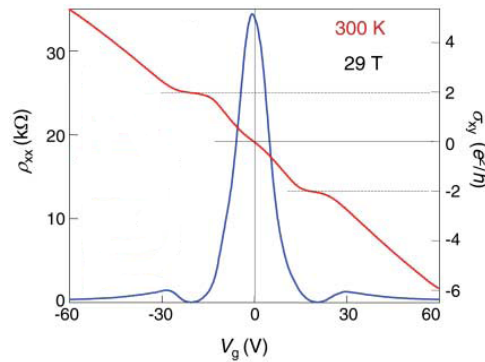
Figure 1.2 Room-temperature Quantum Hall effect in graphene. The figure is adapted from ref.[25].

coupling in graphene is very weak. This makes graphene a good platform to study spin transport and spin precession [28].

Optical Properties Graphene has a particularly simple optical absorption spectrum. In the infrared range, graphene exhibits an almost uniform absorbance of $\pi\alpha=2.3\%$ [29,30], where α is the fine structure constant. Such a universal absorbance, one only depends on the fundamental constant, arises from the conic electronic structure of massless Dirac fermions in graphene. The significant light absorption also allows us to visualize the one-atom-thick graphene even with our naked eyes. In addition, by varying the Fermi level with an electrical gate, graphene's absorption can be tuned significantly in the infrared range by Pauli blocking [31,32].

Mechanical Properties While graphene exhibits remarkable electronic and optical properties, its mechanical properties are equally impressive. In spite of its one-atom thickness, graphene possesses enormous mechanical strength. Graphene is the strongest material ever measured [33]. Its breaking strength is ~ 42N/m, which is more than 100

times larger than that of a hypothetical steel film of the same thickness. Graphene is, on the other hand, also the most flexible elastic membrane. It can sustain more than 20% of local strain without breaking [33]. In addition, graphene is chemically very stable and its melting temperature is high. The excellent mechanical, chemical and thermodynamical stabilities allow graphene to be manipulated in various conditions. For instance, micrometer-sized graphene sheets can be suspended over the holes or trenches on the substrates or over the electrodes in the devices. These free-standing graphene sheets can be used as high-frequency nanoscale electromechanical oscillators [34,35] and also transparent support for imaging tiny objects such as helium atoms by TEM [36]. The graphene membrane can also be used as an ultrathin mask to protect the molecular layers (*e.g.* water) adsorbed on a surface and makes the imaging of the weakly-adsorbed layers possible with a common AFM [37]. In addition, due to graphene's small lattice constant, it is not permeable to even the helium atoms. Graphene can therefore be used to store gas. On the other hand, by drilling a nanometer-sized hole in the graphene membrane, it can be used to filter ions and molecules (*e.g.* DNA) in solutions [38-40]. Such filtering capability makes graphene a promising tool to sequence DNA in the future.

Strain Engineering Recent studies also found that mechanical deformation of the malleable graphene sheet can effectively modify the material's electronic and vibrational properties. In particular, strains in graphene can produce an effect on its charge carriers just like that of a magnetic field [41,42]. Using this method, an unprecedentedly strong pseudo-magnetic field in excess of 300 Tesla was obtained in highly-strained graphene nanobubbles [43]. In the aspect of vibrational properties, uniaxial strain can lower the

crystal symmetry of graphene and lift the degeneracy of certain phonon modes. The split of the phonon energy levels (a few meV) is observable in Raman spectroscopy [44,45].

Band Gap Graphene is a gapless semiconductor. The lack of a band gap limits its applications in electronics, such as field-effect transistors [46] that require a high current on/off ratio. To address this issue, several approaches have been made to create a band gap in graphene. For instance, by interaction with the hydrogen atoms, graphene could be chemically modified and possibly transformed into a new material called "graphane" with a band gap [47]. The band gap can also be produced by confining the charge carriers in graphene nanoribbons. Quasi-one-dimensional graphene ribbons with widths below 50 nm could be produced by various methods, including lithographic patterning of graphene [48], bottom-up fabrication from monomers[49], nanoscale reduction of graphene oxide [50], chemical derivation from graphite solution [51] and unzipping of carbon nanotubes [52,53].

Large-Scale Graphene Besides creating a band gap, industrial applications of graphene require large graphene wafers, on which microscopic circuits and devices can be patterned. To this end, various techniques have been developed to grow large-scale graphene. Notable techniques include epitaxial growth from SiC substrates [12,54,55], chemical vapor deposition (CVD) on metallic surfaces [56,57] and growth from solid carbon sources [58]. CVD graphene films of 30-inch length have now been produced on copper substrates [59] and can be transferred to any other substrates. These large graphene films can be used as the stretchable transparent electrodes [56]. For instance, touch screens using graphene films [59] have recently been demonstrated, and will be the most promising graphene commercial products in the near future. Apart from industrial

applications, CVD graphene is found to exhibit grain boundaries that consist of one-dimensional topological defects [60,61], which are of great interest in basic science research.

Bilayer Graphene   While graphene shows many remarkable properties, its bilayer counterpart is equally interesting. By stacking an extra graphene layer on top of graphene, the interlayer interaction can modify the material's properties significantly. The bilayer possesses the hyperbolic energy bands, in contrast to the linear bands in monolayer. The low-energy charge carriers in bilayer are governed by a peculiar Hamiltonian with combined features of the Dirac and Schrodinger equations [1,2]. The carriers have the chirality of Dirac fermions, but also carry masses as the Schrodinger particles. Such massive chiral fermions have no analogy in other systems. Bilayer graphene exhibits a unique QHE [62,63], one different from that in monolayer graphene and conventional semiconductors. In addition, though bilayer graphene is a gapless semiconductor, the application of a perpendicular electric field can modify its band structure and open a band gap. Bilayer graphene is the first semiconductor with a tunable band gap. Its gap size can be varied from zero up to 250 meV by an electrical gate [64,65].

1.3 Electronic Properties of Graphene

1.3.1 Band Structure of Graphene

Graphene has a hexagonal honeycomb lattice [Figure 1.3(a)] [19]. Its primitive unit cell contains two carbon atoms, denoted as A and B and separated by a distance
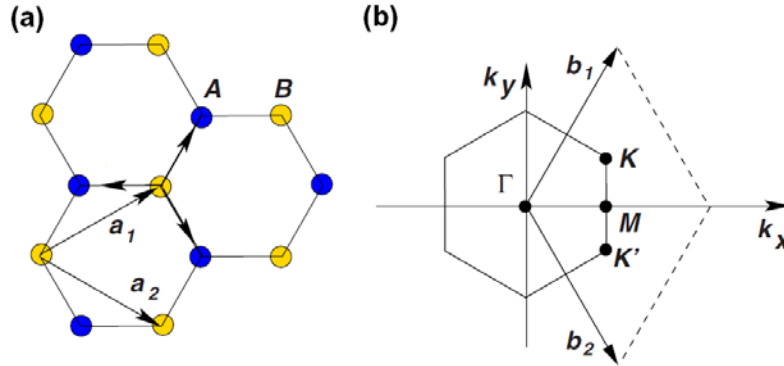
Figure 1.3 (a) The lattice structure of graphene. Blue and yellow dots denote, respectively, the A and B sublattices of the graphene honeycomb lattice. The vector $\mathbf{a_1}$ and $\mathbf{a_2}$ are the lattice unit vectors. **(b)** The corresponding Brillouin zone. The Dirac cones are located at the K and K' points. The figure is adapted from ref.[19].

$a = 1.42 \overset{\circ}{\text{A}}$. The primitive translation vectors $\mathbf{a_1}$ and $\mathbf{a_2}$ have a magnitude of $\sqrt{3}a = 2.46 \overset{\circ}{\text{A}}$. Graphene's crystal structure has a symmetry point group D_{3h}, which contains six-fold rotations, inversion and reflection symmetry. The Brillouin zone of graphene can be obtained by rotating its lattice for 90 degree [Figure 1.3(b)]. The reciprocal vectors $\mathbf{b_1}$ and $\mathbf{b_2}$ have a magnitude of $2/\sqrt{3}a$.

The charge carriers in graphene can be described by a nearest-neighbor tight-binding (TB) Hamiltonian:

$$\hat{H} = -t \sum_{(\vec{R}_A, \vec{R}_B)} \left(\left| \vec{R}_A \right\rangle \left\langle \vec{R}_B \right| + \left| \vec{R}_B \right\rangle \left\langle \vec{R}_A \right| \right) \qquad (1.1)$$

Here $\left| \vec{R} \right\rangle$ is the Wannier wavefunction at the atomic site $\vec{R}$. The summation is over all the pairs of nearest neighbors in the A and B sublattices of graphene. The parameter t represents the hopping integral. Here we have neglected the weak spin-orbit coupling in graphene. By using the Fourier-transformed basis

$$\left| A_{\vec{k}} \right\rangle = \frac{1}{\sqrt{N}} \sum_{\vec{R}_A} e^{i\vec{k}\cdot\vec{R}_A} \left| \vec{R}_A \right\rangle \tag{1.2}$$

$$\left| B_{\vec{k}} \right\rangle = \frac{1}{\sqrt{N}} \sum_{\vec{R}_B} e^{i\vec{k}\cdot\vec{R}_B} \left| \vec{R}_B \right\rangle , \tag{1.3}$$

the Hamiltonian becomes

$$\hat{H}(\vec{k}) = -t \begin{pmatrix} 0 & \alpha(\vec{k}) \\ \alpha^*(\vec{k}) & 0 \end{pmatrix}, \tag{1.4}$$

where

$$\alpha(\vec{k}) = e^{iak_x} + 2e^{-iak_x/2} \cos\left(\sqrt{3}ak_y/2\right) \tag{1.5}$$

The associated energy spectrum is

$$E(\vec{k}) = \pm t \sqrt{1 + 4\cos^2\left(\sqrt{3}ak_y/2\right) + 4\cos\left(\sqrt{3}ak_y/2\right)\cos\left(\sqrt{3}ak_x/2\right)} \tag{1.6}$$
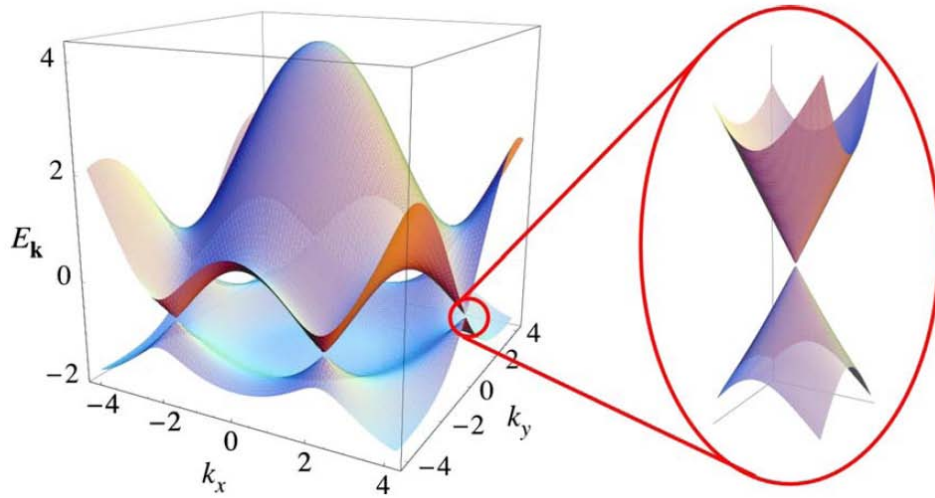
Figure 1.4 Energy spectrum of graphene by a nearest-neighbor tight-binding model (in unit of t). The zoom-in shows the linear dispersion at one Dirac point. The figure is adapted from ref.[19].

The plot of $E(\vec{k})$ is presented in Figure 1.4. Since there is only one valence electron per atom in graphene, the band is half-filled and the Fermi level is at $E=0$. The Fermi surface becomes just two points (*i.e.* the K and K' points) in the Brillouin zone. By expanding $\alpha(\vec{k})$ around the K point and suitably rotating the coordinates, we obtain an effective Hamiltonian for the low-energy charge carriers in graphene:

$$\hat{H}(\vec{k}) = \hbar \upsilon_F \begin{pmatrix} 0 & k_x - ik_y \\ k_x + ik_y & 0 \end{pmatrix}. \tag{1.7a}$$

Here $\upsilon_F = \dfrac{3at}{2\hbar}$ is the Fermi velocity and k_x and k_y are measured from the K point. A similar effective Hamiltonian with a sign change of k_x can be obtained for low-energy charge carriers near the K' point. The energy spectrum and eigenfunctions associated with $\hat{H}(\vec{k})$ is

$$E(\vec{k}) = \pm \hbar \upsilon_F \sqrt{k_x^2 + k_y^2} = \pm \hbar \upsilon_F \left| \vec{k} \right| \tag{1.8}$$

$$\psi_{\pm} = \frac{1}{\sqrt{2}} \begin{pmatrix} 1 \\ \pm e^{i\theta_k} \end{pmatrix}, \tag{1.9}$$

where θ_k is the angle of the vector k with x-axis. By using the momentum operator $\vec{p} = \hbar \vec{k}$ and the Pauli matrices $\vec{\sigma} = \left(\sigma_x, \sigma_y \right)$, Eq 1.7a can be expressed as

$$\hat{H} = \upsilon_F \vec{\sigma} \cdot \vec{p} \tag{1.7b}$$

There are some remarkable characteristics in the Hamiltonian and energy spectrum for graphene's low-energy carriers. First, the energy spectrum has a conical structure (zoom-in in Figure 1.4), in contrast to the parabolic dispersion in conventional semiconductors.

The charge carriers in graphene thus travel with a constant velocity υ_F. For the typical TB hopping parameter $t \sim 3$ eV in graphene, υ_F is about 10^6ms^{-1}, *i.e.* 1/300 of the speed of light. It should be noted that, while the conical energy spectrum of graphene obtained here is derived based on a TB model, detailed analysis based on group theory [66] shows that it is an exact result due to the symmetry of graphene (without spin-orbit coupling) and is therefore independent of the models. Second, the Hamiltonian (Eq. 1.7b) is identical to the two-dimensional Dirac Hamiltonian for massless particles, except that the speed of light c is now replaced by the Fermi velocity υ_F. The low-energy charge carriers in graphene thus behave as the massless Dirac fermions. Third, the eigenfunctions $\psi_\pm$ are spinors with two components that correspond to A and B sublattice. While they are usually called psudospin due to their analog with the electron spin, a recent study [67] showed that the "psudospin" in graphene actually carries intrinsic angular momentum. Fourth, $\hat{H}$ commutes with the charality (or helicity) operator $\hat{h} = \frac{1}{2}\vec{\sigma} \cdot \frac{\vec{p}}{|\vec{p}|}$, which is the projection of pseudospin on the momentum direction.

Therefore, the charge carriers in graphene have a conserved chirality. To change the carriers' chirality, one needs to break the A and B lattice symmetry in graphene, which requires a sharply varying potential that are usually not possible in solids. Therefore, the scattering probability of the charge carriers in graphene is low since the change of momentum must be accompanied with the flip of spin. This is the underlying mechanism for the Klein tunneling [20-22] of the charge carriers in graphene, i.e. absence of back scattering when the carriers meet a potential barrier.

1.3.2 Optical Conductivity of Graphene

An interesting property of graphene that arises from its Dirac Hamiltonian is the uniform and universal optical absorption spectrum, given by $\pi\alpha = 2.3\%$, where α is the fine structure constant [68-72]. By using the Dirac Hamiltonian with miminum coupling

$$\hat{H} = \upsilon_F \vec{\sigma} \cdot \left(\vec{p} - e\vec{A}/c \right),$$
(1.10)

we found that the perturbation for the electron-photon interaction is

$$\hat{H}_{int} = \upsilon_F \frac{e}{i\omega} \vec{\sigma} \cdot \vec{E},$$
(1.11)

where $\vec{E}$ is the electric field of the incoming light. The incoming energy flux is

$$W_{in} = \frac{c}{4\pi} \left| \vec{E} \right|^2.$$
(1.12)

By using Fermi's golden rule, we obtain the absorption energy flux

$$W_{abs} = \frac{2\pi}{\hbar} \left| \langle f | H_{int} | i \rangle \right|^2 \rho \left(\frac{\hbar\omega}{2} \right) \hbar\omega = \frac{e^2}{4\hbar} \left| \vec{E} \right|^2.$$
(1.13)

The absorbance is then

$$\frac{W_{abs}}{W_{in}} = \pi \frac{e^2}{\hbar c} = \pi\alpha = 2.3\%.$$
(1.14)

Here $\alpha = \frac{e^2}{\hbar c} \approx 1/137$ is the fine structure constant. The absorbance corresponds to an optical conductivity of $\sigma = \frac{\pi}{4} G_0$, where $G_0 = 2e^2/h$ is the quantum conductance. The result shows that the absorbance of graphene depends only on the fundamental constant of the electron-photon interaction, and is entirely independent of the details of the band structures as well as the photon energy of the incoming light. This particularly simple

result arises from the complete cancellation between the energy dependence of the electron-photon coupling matrix elements and of the density of state in graphene.

Experimentally, the predicted uniform absorption for graphene was confirmed in the mid-infrared range (Figure 1.5) [30]. However, deviations exist in the high and low energy limits. The absorption is found to increase in the visible-to-ultraviolet range due to
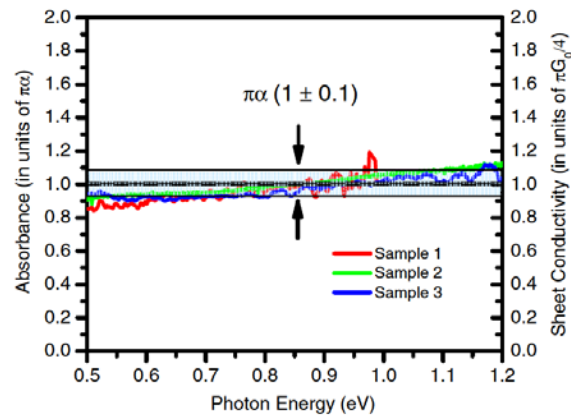
Figure 1.5 Absorption spectra for three different graphene samples over the spectral range of 0.5 - 1.2 eV. The left scale gives the absorbance in units of $\pi\alpha$, while the right scale gives the corresponding optical sheet conductivity in units of $\pi G_0/4$. The black horizontal line corresponds to the predicted universal absorbance of 2.3%. The figure is adapted from ref.[30].
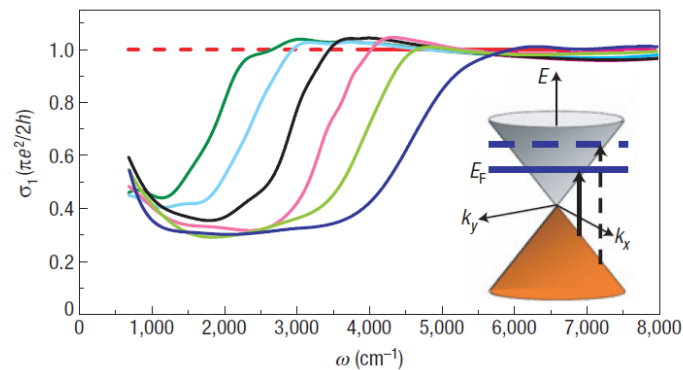
Figure 1.6 The optical conductivity of graphene at different voltages of a SiO_2 back gate. The gate voltages with respect to the charge neutrality point are 10, 17, 28, 40, 54 and 71 V for the conductivity spectra from left to right. The inset shows the band structure of graphene near the Dirac point and the interband transition at $2E_F$. The figure is adapted from ref.[32].

the trigonal warping and the excitonic effects [73-75], which have been neglected in the simple model for non-interacting massless Dirac fermions. On the other hand, the graphene samples are usually unintentionally doped by the substrates and adsorbed molecules. The associated finite Fermi level in graphene suppresses of absorption of low-energy photons by Paul's exclusion principle [30]. By varying the doping level with an electrical gate, graphene's absorption and optical conductivity can be tuned in the infrared range (Figure 1.6) [31,32].

1.3.3 Landau Levels of Graphene

Now let's consider the Landau levels of graphene under a perpendicular magnetic field. By using the Landau gauge with a magnetic vector potential of $\vec{A} = -By\hat{x}$, and the Hamiltonian becomes

$$\hat{H} = \upsilon_F \begin{pmatrix} 0 & p_x - ip_y - eBy/c \\ p_x + ip_y - eBy/c & 0 \end{pmatrix}. \tag{1.15}$$

Since there is no explicit x dependence in the Hamiltonian, we can change the operator p_x into a scalar by using the ansatz eigenfunction $\psi(x, y) = f_n(y)e^{ixp_x/\hbar}$. By introducing a dimensionless variable $\xi = y/l_B - q_x l_B$, where $l_B = \sqrt{\hbar c/eB}$, we can simplify Eq. 1.15 as

$$\hat{H} = \hbar\omega_c \begin{pmatrix} 0 & a_- \\ a_+ & 0 \end{pmatrix}, \tag{1.16}$$

where $a_{\pm} = \frac{1}{\sqrt{2}}\left(\xi \mp \frac{\partial}{\partial \xi}\right)$ and $\omega_c = \sqrt{2}\upsilon_F / l_B$. The operator $a_{\pm}$ can be shown to satisfy the

commutation relation $[a_-, a_+] = 1$ and are, thus, like the raising and lowering operator of

a one-dimensional Harmonic oscillator. It can also be shown that the eigenstates are:

$$f_n = \begin{pmatrix} |n-1\rangle \\ \pm|n\rangle \end{pmatrix}, \tag{1.17}$$

where $|n\rangle$ satisfies $a_+|n\rangle = \sqrt{n+1}|n\rangle$ and $a_-|n\rangle = \sqrt{n}|n-1\rangle$. The corresponding energy

eigen values are [4]

$$E_n = \pm\hbar\omega_c\sqrt{n}. \tag{1.18}$$

Eq. 1.18 is remarkably different from the conventional Landau-level spectrum

$E_n = \pm\hbar\omega(n+1/2)$ derived from the Schrödinger equation. First, there is a zero-energy

Landau level in graphene, which cannot be obtained by any semi-classical methods, but
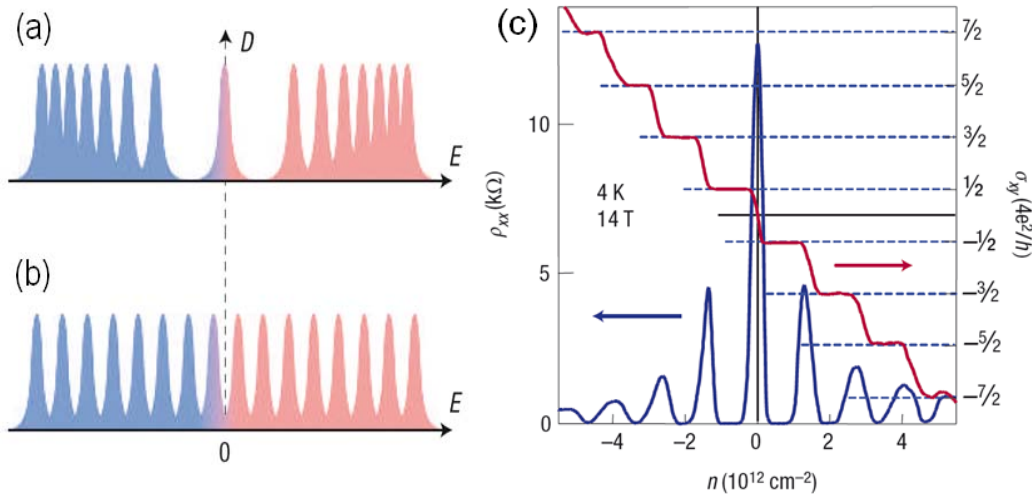
Figure 1.7 (a) (b) Schematics of density of state of the massless Dirac fermions in graphene (a) and the massive Schrödinger charge carriers in conventional semiconductors (b) under a perpendicular magnetic field. **(c)** Half-integer quantum Hall effect in graphene. The figures are adapted from ref.[1].

is due to pure quantum effects [Figure 1.7 (a)]. Second, the energy levels follow a square-root relation, instead of the conventional equal-spacing relation [Figure 1.7 (a, b)]. Third, the constant ½ is missed in Eq. 1.18. This results in an unusual quantum Hall effect in graphene that shows the plateaus of the Hall conductivity at half-integer positions instead of the standard integer positions [Figure 1.7 (c)] [1,17,18].

1.4 Electronic Properties of Bilayer Graphene

A bilayer graphene is obtained by stacking two graphene layers together. The simplest stacking sequence in bilayer is AA stacking, in which one layer is placed directly on top of the other. This arrangement is, however, known to be less stable than the Bernal AB stacking [76], in which one layer is displaced along the direction of the honey comb lattice by a carbon-carbon bond length (Figure 1.8). The Bernal-stacked bilayer graphene, which is mostly studied in the literature, has lower crystal symmetry than the monolayer graphene. It has the symmetry point group D_{3d}, which contains the
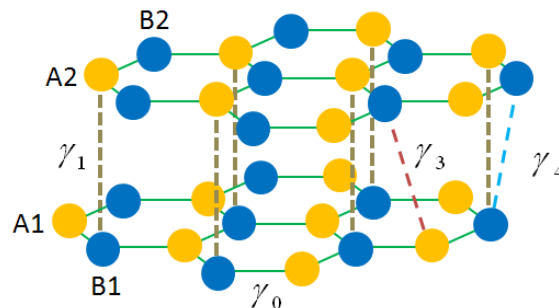
Figure 1.8 Lattice structure of bilayer graphene with the relevant tight-binding (TB) parameters shown. The yellow and blue dots represent carbon atoms in the A and B sub-lattices of the graphene honeycomb structure. γ_0 is the TB hopping parameter between two nearest-neighbor atoms in the same graphene layer. γ_1, γ_3 and γ_4 are three TB hopping parameters between atoms in different graphene plane.

inversion symmetry, but no reflection symmetry. The interlayer spacing is $3.37\overset{\circ}{A}$.

The coupling between two graphene layers can change the electronic structure of bilayer significantly [19,63,76,77]. In a tight-binding (TB) model, the charge carriers of a Bernal-stacked bilayer graphene near the K point in the Brillouin zone can be described by an effective Hamiltonian in the basis (A1, B1, A2, B2)

$$H_{bilayer} = \begin{pmatrix} U/2 & \upsilon_F\pi^{\dagger\dagger} & -v_4\pi & v_3\pi \\ \upsilon_F\pi & U/2+\delta & \gamma_1 & -v_4\pi^{\dagger} \\ -v_4\pi & \gamma_1 & -U/2+\delta & v_F\pi^{\dagger} \\ v_3\pi^{\dagger} & -v_4\pi & \upsilon_F\pi & -U/2 \end{pmatrix}.$$ (1.19)

Here $\pi = p_x + ip_y$ and $\gamma_1 \sim 390$ meV is the nearest-neighbor interlayer hopping parameter. If we only consider γ_1 for the interlayer coupling, the bilayer band structures consist two hyperbolic conduction bands, separated by γ_1, and two valence bands that are inversely identical to the conduction bands [red lines in Figure 1.9(a)]. Based on this symmetric band structure, the parameter $v_3 = \gamma_3/\gamma_0$ introduces small trigonal-warping effects and $v_4 = \gamma_4/\gamma_0$ introduces an electron-hole asymmetry effect in the band structure [77]. U is the potential difference between the two graphene layers, and δ is the potential difference between two nonequivalent atoms in the individual graphene layer. To illustrate the effect of U, let's consider a simplified Hamiltonian with only γ_1 and U, at the K point where π=0

$$H_{bilayer} = \begin{pmatrix} U/2 & 0 & 0 & 0 \\ 0 & U/2 & \gamma_1 & 0 \\ 0 & \gamma_1 & -U/2 & \upsilon 0 \\ 0 & 0 & 0 & -U/2 \end{pmatrix}.$$

(1.20)

The eigenenergies are

$$E_{c1,v1} = \pm U/2,$$
$$E_{c2,v2} = \pm\sqrt{\gamma_1^2 + U^2/4} \approx \pm\gamma_1.$$

(1.21)

Here $c1$, $c2$, $v1$ and $v2$ denote the first and second conduction bands and valence bands [green lines in Figure 1.9(a)]. We found that the interlayer potential difference U breaks the inversion symmetry of bilayer and lifts up the degeneracy at the K point. As the conduction and valence bands are split, a band gap is opened in bilayer [63,76-81]. Experimentally, the band gap can be realized in bilayer with the application of a
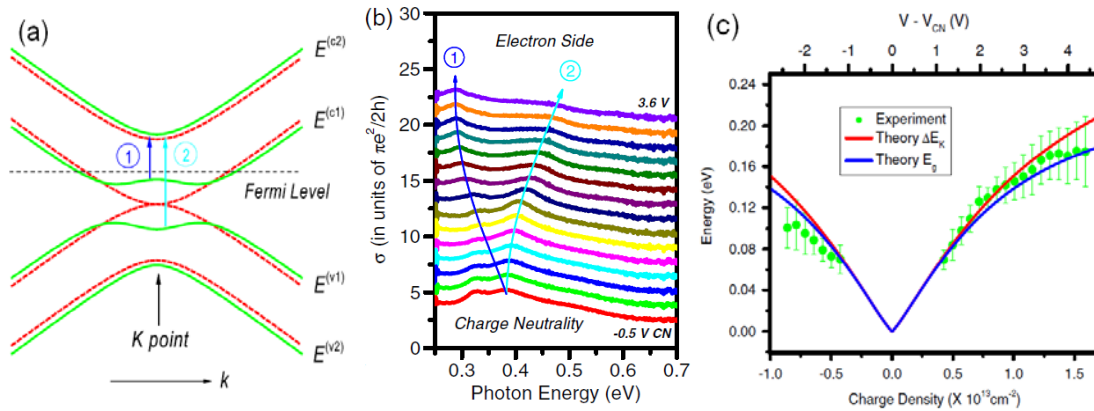
Figure 1.9 (a) Band gap opening in bilayer graphene due to interlayer potential difference induced by the shift of Fermi level. The red (green) line represents the band structure at zero (finite) doping level. **(b)** The optical conductivity measured in bilayer graphene with different doping level under an electrolyte top gate. The absorption peak 1 and 2 correspond to the transition 1 and 2 in (a). **(c)** The extracted band gap from (b) and the comparison with the theoretical prediction of the band gap (E_g) and the energy gap at K point (ΔE_K). The figures are adapted from ref.[63].

perpendicular electric field using double-gate devices [65,82-85], in which the back and top gates are applied with opposite voltages. On the other hand, due to the self-consistent charge distribution in doped bilayer graphene, the band gap can also be induced in single-gate bilayer device [64] or chemically doped bilayer samples [80,86]. Infrared spectroscopy serves as an excellent means of identifying the band gap in bilayer graphene [64,65]. As shown in Figure 1.9(b), new absorption peaks (peak 1 and 2) emerge when the band gap opens in high doping charge density. They correspond to the optical transitions from states on both sides of the energy gap to the common higher-lying conduction band [transition 1 and 2 in Figure 1.9(a)]. The size of the induced band gap can be deduced directly from experiment and compared with the predictions based on TB model. A band gap approaching 200 meV can be opened in bilayer when an electric field of 1 V/nm is applied, inducing a carrier density of about 10^{13} cm^{-2} [Figure 1.9 (c)].

The TB parameters v_4 and δ introduce electron-hole asymmetry effects on the bilayer band structure [Figure 1.10 (a)] [77,87]. The on-site energy difference δ modifies the energy gap between the two conduction bands and between the two valence bands. The next-nearest-neighbor coupling v_4 modifies the slope of the dispersion differently in the conduction and valence bands. This asymmetric band structure gives rise to different optical transition behaviors on the electron and hole side, which can be probed experimentally by infrared spectroscopy [87]. Figure 1.10 (b) shows the optical transition energies in graphene bilayer doped with a SiO$_2$/Si back gate. The observed asymmetric

behaviors on the electron and hole side can be accounted quantitatively based on the TB

band structure in Figure 1.10 (a).
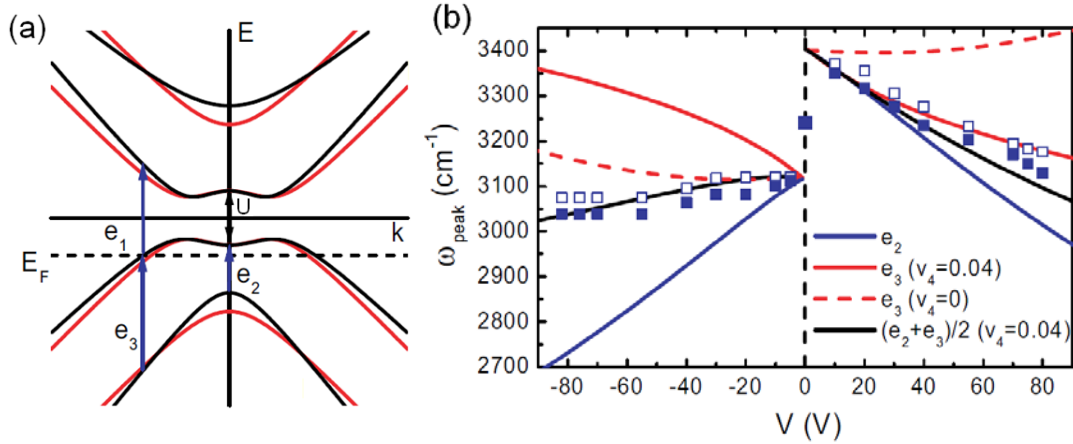
Figure 1.10 (a) Schematics of the band structure of bilayer graphene with zero (red) and finite (black) values of δ and υ_F, together with the allowed interband transitions. **(b)** Comparison with the experimental optical absorption peaks and the theoretical predictions. The solid and open symbols are experimental data from the conductivity and transmission spectra, respectively. Solid lines are theoretical values of the transition at e_2, $e3$ and their average values with $\upsilon_F=1.1 \times 10^6$ m/s, $\gamma_1=404$ meV and δ=18 meV and $v_4=0.04$. Red dashed line is the transition value of e_3 with similar parameters except $v_4=0$. The figures are adapted from ref.[87].

1.5 Electronic Properties of Trilayer Graphene

We can obtain a trilayer graphene by stacking another graphene layer on top of

the Bernal-stacked bilayer. There are two possible ways to stacking the third layer, which

resulted in two types of trilayer that are thermodynamically stable [76]. Let's denote two

neighbor atoms in the first (bottom) graphene layer as position A and B and the center of

the hexagon as position C [Figure 1.11(a)]. To obtain the stable Bernal stacking in bilayer,

the second graphene layer should be translated from position A to B. By placing another

layer on this AB bilayer, we have either a Bernal stacked (ABA) trilayer if the third layer

is translated back to position A [Figure 1.11(b)], or a rhombohedrally stacked (ABC)

trilayer if the third layer is translated to position C [Figure 1.11(c)]. The ABA trilayer graphene has the symmetry point group D_{3h}, which contains the mirror symmetry with respect to the reflection of the middle plane. The ABC trilayer has the symmetry point group D_{3d} that contains the spatial inversion symmetry.

(a)   (b)   (c)
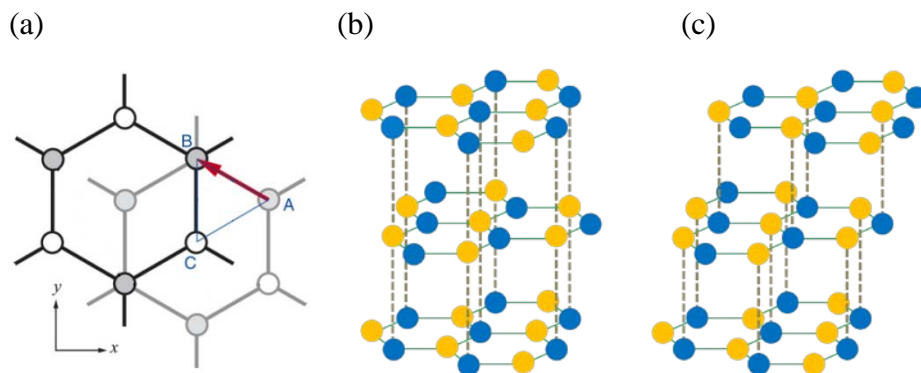
Figure 1.11 (a) In-plane translations (A to B, A to C) of an upper graphene layer relative to the bottom layer. **(b, c)** Two different structures of trilayer graphene with ABA (b) and ABC (c) stacking sequence. The yellow and blue dots represent carbon atoms in the A and B sub-lattices of the graphene honeycomb structure. Figure (a) is adapted from ref.[76].
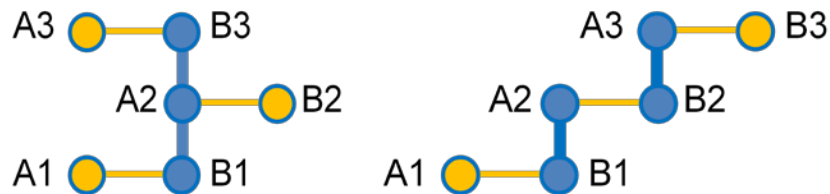
Figure 1.12 Tight-binding diagrams from ABA (left) and ABC (right) trilayer graphene. The yellow and blue lines represent intra- and inter-layer nearest-neighbor coupling. At the K point, the intralayer coupling becomes zero. The atoms in yellow then become non-bonding monomers and the atoms in blue form a trimer in ABA trilayer and two dimers in ABC trilayer.

The different symmetry of the crystal structure results in distinct electronic structure in ABA and ABC trilayer graphene. In a simple TB calculation that considers only the nearest intra- and inter-layer neighbors (Figure 1.12), the electronic structure of

ABA and ABC trilayer graphene can be described by the following Hamiltonian in the basis of (A1, B1, A2, B2, A3, B3)

$$
H_{ABA} = \begin{pmatrix}
0 & \upsilon_F \pi^{\dagger} & 0 & 0 & 0 & 0 \\
\upsilon_F \pi & 0 & \gamma_1 & 0 & 0 & 0 \\
0 & \gamma_1 & 0 & \upsilon_F \pi^{\dagger} & 0 & \gamma_1 \\
0 & 0 & \upsilon_F \pi & 0 & 0 & 0 \\
0 & 0 & 0 & 0 & 0 & \upsilon_F \pi^{\dagger} \\
0 & 0 & \gamma_1 & 0 & \upsilon_F \pi & 0
\end{pmatrix},
\tag{1.22}
$$

$$
H_{ABC} = \begin{pmatrix}
0 & \upsilon_F \pi^{\dagger} & 0 & 0 & 0 & 0 \\
\upsilon_F \pi & 0 & \gamma_1 & 0 & 0 & 0 \\
0 & \gamma_1 & 0 & \upsilon_F \pi^{\dagger} & 0 & 0 \\
0 & 0 & \upsilon_F \pi & 0 & \gamma_1 & 0 \\
0 & 0 & 0 & \gamma_1 & 0 & \upsilon_F \pi^{\dagger} \\
0 & 0 & 0 & 0 & \upsilon_F \pi & 0
\end{pmatrix}.
\tag{1.23}
$$

The corresponding band structure of ABA and ABC trilayer are shown in Figure 1.13. We find that the low-energy band structure of ABA and ABC trilayers is very different. ABA trilayer has four low-energy bands that follow either linear or quadratic dispersion, while ABC trilayer has only two low-energy bands that follow the cubic dispersion.

At the K point where the intralayer coupling is zero, the ABA Hamiltonian can be further simplified in the basis (A1, B2, A3, B1, A2, B3) as

$$
H_{ABA} = \begin{pmatrix} M_1 & 0 \\ 0 & T \end{pmatrix},
\tag{1.24}
$$

where

$$M_1 = \begin{pmatrix} 0 & 0 & 0 \\ 0 & 0 & 0 \\ 0 & 0 & 0 \end{pmatrix}, \tag{1.25}$$

$$T = \begin{pmatrix} 0 & \gamma_1 & 0 \\ \gamma_1 & 0 & \gamma_1 \\ 0 & \gamma_1 & 0 \end{pmatrix}. \tag{1.26}$$

From Eq. 1.24, we see that the ABA trilayer consist of three monomers (M) and one
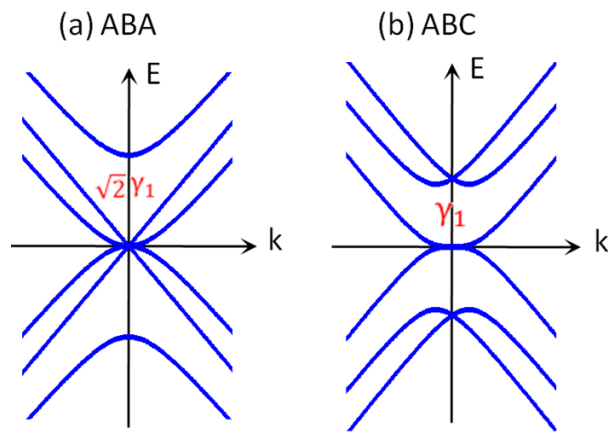
Figure 1.13 Band structure of trilayer graphene with ABA and ABC stacking order. $\sqrt{2}\gamma_1$ and γ_1 are the energy spacing between the low- and high-lying energy bands at the K point for ABA and ABC trilayer, respectively.
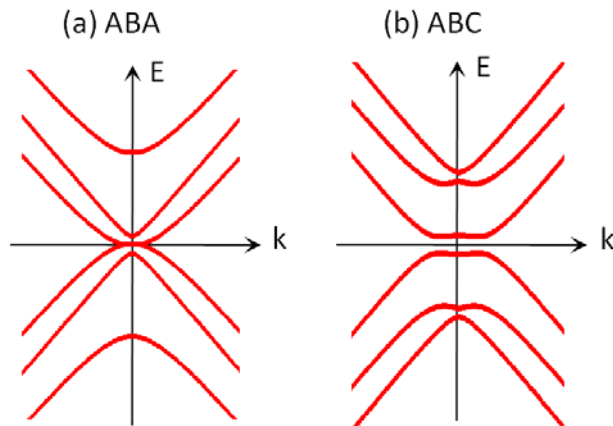
Figure 1.14 Band structure of trilayer graphene with ABA and ABC stacking order with the application of a uniform perpendicular electric field.

trimer (T). The bonding and antibonding states of the trimer give rise to two bands with energy $\pm\sqrt{2}\gamma_1$. The non-bonding state of the trimer and all the monomers have zero energy.

On the other hand, the ABC Hamiltonian at the K point can be written in the basis (A1, B3, B1, A2, B2, A3) as:

$$H_{ABC} = \begin{pmatrix} M_2 & 0 & 0 \\ 0 & D_1 & 0 \\ 0 & 0 & D_2 \end{pmatrix}, \tag{1.27}$$

where

$$M_2 = \begin{pmatrix} 0 & 0 \\ 0 & 0 \end{pmatrix} \tag{1.28}$$

$$D_1 = D_2 = \begin{pmatrix} 0 & \gamma_1 \\ \gamma_1 & 0 \end{pmatrix}. \tag{1.29}$$

The ABC trilayer consists of two monomer states at zero energy and four dimer states at energies $\pm\gamma_1$.

ABA and ABC trilayers have different response to the electric field due to their distinct crystalline and electronic structure [76]. Let's consider the application of a uniform and perpendicular electric field that induces opposite potentials ($\pm U/2$) on the top and bottom layer but zero penitential on the middle layer. By solving the corresponding TB Hamiltonian in ABA and ABC trilayers, we find that a band gap is opened in ABC trilayer while no band gap exists in ABA trilayer. To understand this distinctive behavior,

let's consider the ABA and ABC Hamiltonian at the K point, where the band-gap opening occurs. For ABA trilayer, Eq. 1.25 and 1.26 become

$$M_1 = \begin{pmatrix} U/2 & 0 & 0 \\ 0 & 0 & 0 \\ 0 & 0 & -U/2 \end{pmatrix}, \tag{1.30}$$

$$T = \begin{pmatrix} U/2 & \gamma_1 & 0 \\ \gamma_1 & 0 & \gamma_1 \\ 0 & \gamma_1 & -U/2 \end{pmatrix}. \tag{1.31}$$

We find that the two monomers (at A1 and A3) are split away for an energy spacing of U, and the middle monomer (at B2) is still of zero energy. On the other hand, the trimer states have energies $E = 0$ and $E = \pm\sqrt{2\gamma_1^2 + U^2/4} \approx \pm\left(\sqrt{2}\gamma_1 + U^2/8\right)$ (the approximation is made for small U). Therefore, the zero energy states are doubly degenerate. There is no band gap in ABA trilayer with the application of a uniform electric field [Figure 1.14(a)].

On the other hand, the corresponding monomers and dimers in the ABC Hamiltonian are $M_2 = \begin{pmatrix} U/2 & 0 \\ 0 & -U/2 \end{pmatrix}$, $D_1 = \begin{pmatrix} U/2 & \gamma_1 \\ \gamma_1 & 0 \end{pmatrix}$ and $D_2 = \begin{pmatrix} 0 & \gamma_1 \\ \gamma_1 & -U/2 \end{pmatrix}$. We find that the electric field split the monomer states by an energy gap of U, which constitutes a band gap in ABC trilayers [Figure 1.14(b)]. The electric field also breaks the degeneracy of the high- and low-lying energy levels of the two dimmers, which now have energies $E = \pm\sqrt{\gamma_1^2 + U^2/16} \pm U/4 \approx \pm\gamma_1 \pm U/4$.

1.6 Vibrational Properties of Graphene

1.6.1 Phonon Band Structure of Graphene
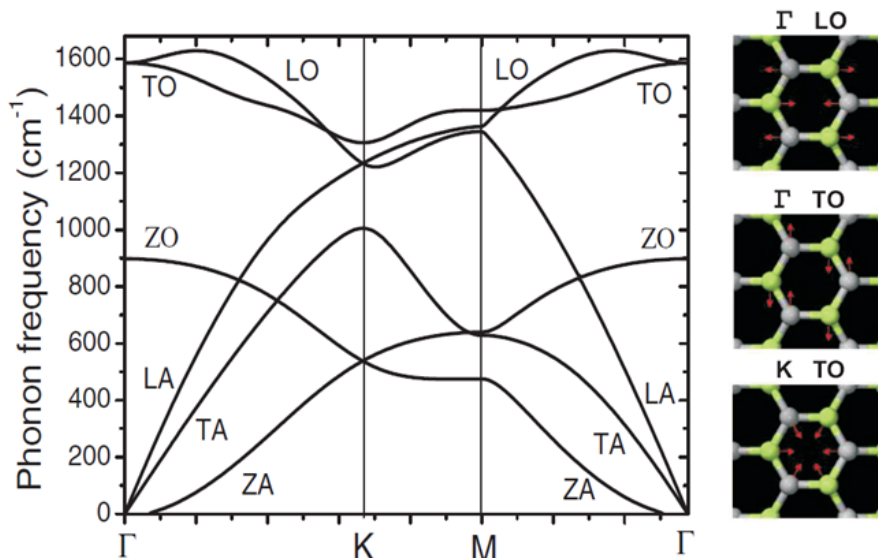
Figure 1.15 Phonon band structure of graphene (left panel) and schematics of LO and TO phonons at Γ and K point (right panel).

Graphene has totally six phonon branches, including three acoustic branches and three optical branches (Figure 1.15). The acoustic branches include the in-plane longitudinal (LA) and transverse (TA) acoustic phonons and the out-of-plane acoustic phonons (ZA). The optical branches include the in-plane longitudinal (LO) and transverse (TO) optical phonons and the out-of-plane optical phonons (ZO). The LO and TO modes are degenerate at the Γ-point due to the symmetry of graphene. In graphene, we are interested in the Γ-point phonons at the zone center and the K-point phonons at the zone edge for two reasons. First, they are Raman active and give rise to strong Raman lines, *e.g.* G, D, and 2D (G') Raman modes [88,89], which carry important information of the graphene samples. Second, they are coupled strongly to the electrons in graphene. The

electron-phonon interaction not only induces a significant renormalization of phonon energy near the Γ and K points, *i.e.* the so-called Kohn anomaly [90], but also plays a critical role in the carrier dynamics of graphene in high-field transport and ultrafast phenomena [91-93].
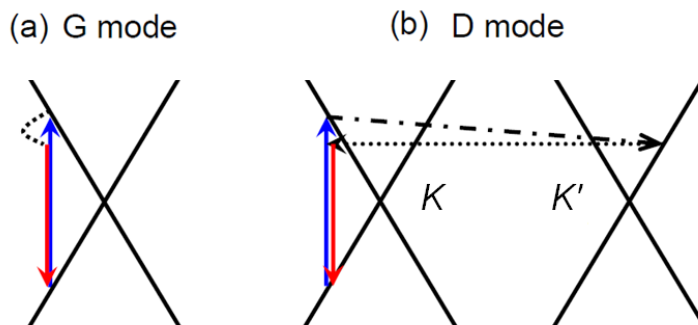
Figure 1.16 Raman processes of G-mode (a) and D-mode (b) in graphene.

1.6.2 Raman G mode

In the Raman spectroscopy of graphene, the G line is associated with the zero-momentum Γ-point LO and TO phonons [Figure 1.16 (a)]. The LO and TO modes are degenerate at Γ-point due to the symmetry of graphene. The degeneracy can be lifted by
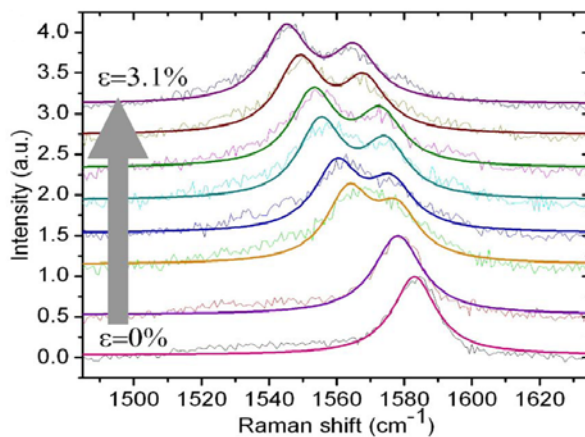
Figure 1.17 Evolution of the spectra of the G band of graphene under strain (ε). The spectra are fit by 2 Lorentz peaks of fixed width 16 cm^{-1}. The figure is adapted from ref.[44].

breaking graphene's crystal symmetry by the application of uniaxial strain. The split of the LO and TO phonon energies can be revealed as the split of the G line in the Raman spectrum (Figure 1.17) [44,45].

Due to the gapless conical electronic structure in graphene, The Γ-point LO and TO phonons can decay into electron-hole pairs. This leads to strong electron-phonon interaction in graphene. On the other hand, the electron-phonon coupling strength can be controlled by varying the Fermi level of graphene [94-96]. When the Fermi level is above half of the phonon energy, the creation of electron-hole pairs are forbidden by Paul blocking, leading to an enhanced energy and longer life time of the phonon, which are reflected, respectively, by the frequency and width of the G line in the Raman spectrum (Figure 1.18).
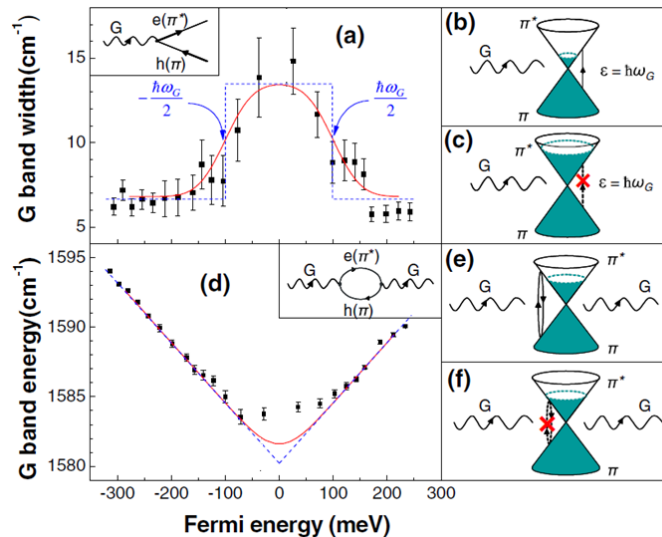
Figure 1.18 (a)–(c) Graphene G band damping and **(d) –(f)** energy renormalization in graphene with a SiO_2 back gate. In (a) and (d), dashed blue lines and solid red lines are the fits for ideal and nonuniform graphene, respectively. The insets are Feynman diagrams for electron-phonon coupling applicable to the case of the G phonon. (b) represents the broadening of the G phonon due to decay into electron-hole pairs. (c) indicates that the G-phonon decay into the electron-hole pair is forbidden by the Pauli principle at high doping charge densities. (e) is for the renormalization of the G-phonon energy by interaction with virtual electron-hole pairs. (f) shows that virtual electron-hole pair transitions are forbidden. The figure is adapted from ref.[96].

1.6.3 Raman D and 2D Modes
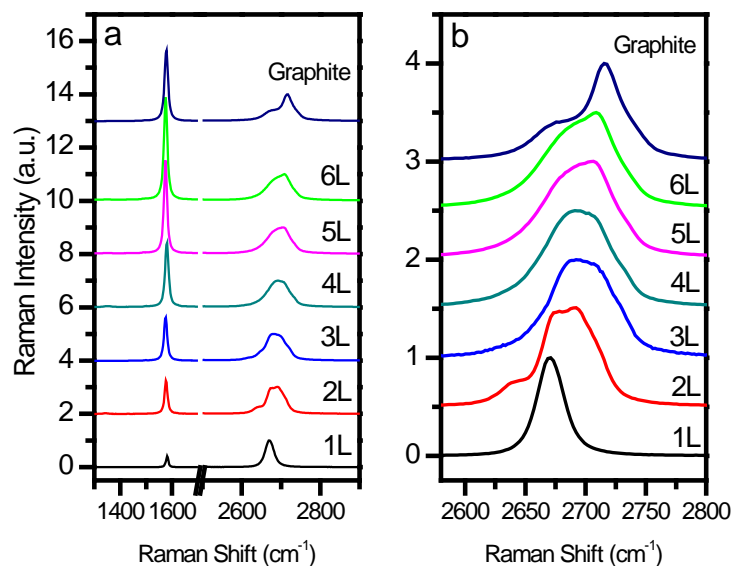
Figure 1.19 (a) The Raman G-mode and 2D-mode in graphite and graphene samples with layer thickness from 1 to 6. **(b)** Zoom-in of the 2D-mode in (a).

In the Raman spectroscopy of graphene, the D line and its overtone (2D) arise from the emission of K-point TO phonons [88,89]. As the K-point phonons carries finite momentum, the first-order D mode can only be activated with defects. This makes the intensity of D mode a good indicator of the concentration of atomic defects in graphene. In graphene and graphite, the D and 2D mode show several anomalous features. First, their frequencies blue-shift with the increase of excitation photon energy. Second, the intensity of the second-order 2D mode is comparable to that of the first-order G mode [Figure 1.19 (a)]. These two peculiar features arise from a double-resonance process [97], in which the photo-excited electrons emit a K-point phonon and jump to another state in the other Dirac cone [Figure 1.16 (b)]. The electrons can be scattered back to the original

cone by scattering with defects (D mode), or emitting another *K*-point phonon (2D mode). The phonon-mediated resonance between two real electronic states strongly enhances the probability of the process and, hence, the corresponding Raman signal.

Since the 2D-mode involves electronic resonance in graphene, its lineshape is therefore sensitive to the electronic structure of the material. In particular, the 2D mode can be used as an accurate means of identifying the layer thickness of monolayer and bilayer graphene [98]. As shown in Figure 1.19, the 2D mode in monolayer shows a particularly narrow Lorentzian lineshape compared to the multi-featured lineshapes in samples of greater thickness. The simple 2D lineshape in graphene arises from its simple electronic structure, which minimizes the number of phonon wavevectors that satisfy the double-resonance conditions. In addition, the 2D-mode in bilayer graphene shows a shoulder that can be used as a fingerprint of the bilayer thickness. In few-layer graphene samples, the 2D lineshape become more ambiguous because of the more complicated electronic structures.

1.7 Vibrational Properties of Bilayer Graphene

Bilayer graphene has twelve phonon branches, including nine optical branches and three acoustic branches. Since the interlayer coupling is weak, the high-energy optical phonon branches (LO, TO and ZO) are almost degenerated and hence similar to the phonon modes in monolayer (Figure 1.20). The low-energy acoustic phonons (LA, TA ZA) are, however, distinctive from those in monolayer. In particular, three new inter-layer vibration modes emerge in bilayer: two layer-shearing modes (LO' and TO') and

one layer-breathing mode (ZO'), in which the two graphene layers vibrate out of phase in the lateral and vertical direction, respectively, as shown in Figure 1.21.
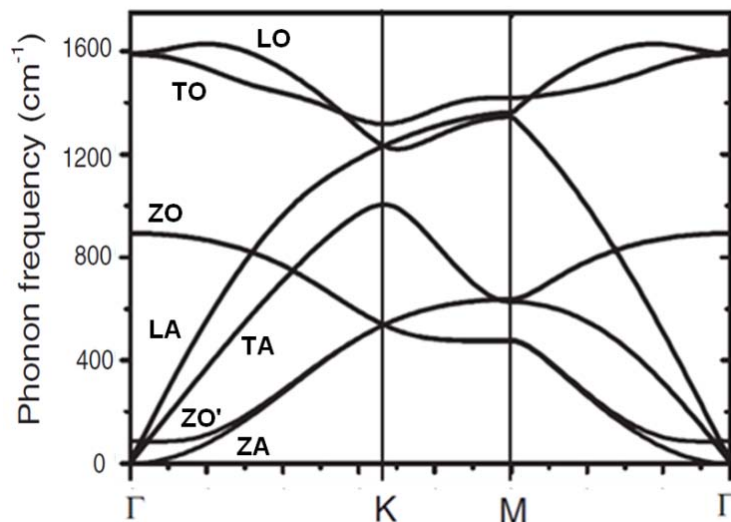
Figure 1.20 Phonon band structure of graphene bilayer.
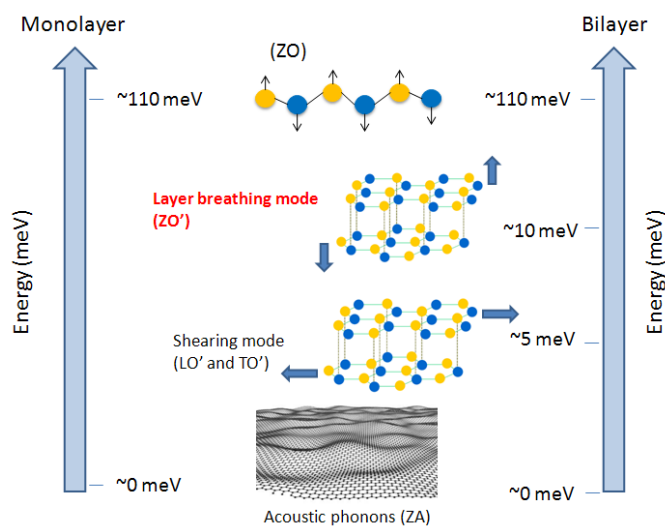
Figure 1.21 Out-of-plane phonon modes in graphene monolayer and bilayer. The layer-breathing mode (ZO') and shearing mode (LO' and TO') are absent in monolayer.

1.8 **Ultrafast Carrier and Phonon Dynamics in Graphene**

The interactions between the charge carriers in graphene and the strongly coupled optical phonons (SCOP) at Γ and K points in the Brillouin zone have significant influence on the carrier dynamics of graphene. In particular, the strong electron-SCOP interactions play an important role in the decay dynamics of carriers with the excitation of femtosecond laser. Studies based on time-resolved Raman spectroscopy have shown that the photo-excited electrons equilibrate with the SCOPs in a time scale of 100 fs in graphene (Figure 1.22) [99], graphite [91,92,100] and also carbon nanotubes [101]. Due to the large specific heat of the SCOP, over 90% of the excitation energies are transferred into the SCOP system. This carrier-SCOP equilibrium subsystem stays out of equilibrium with the rest of the system, and cools down by anharmonic decay into the acoustic
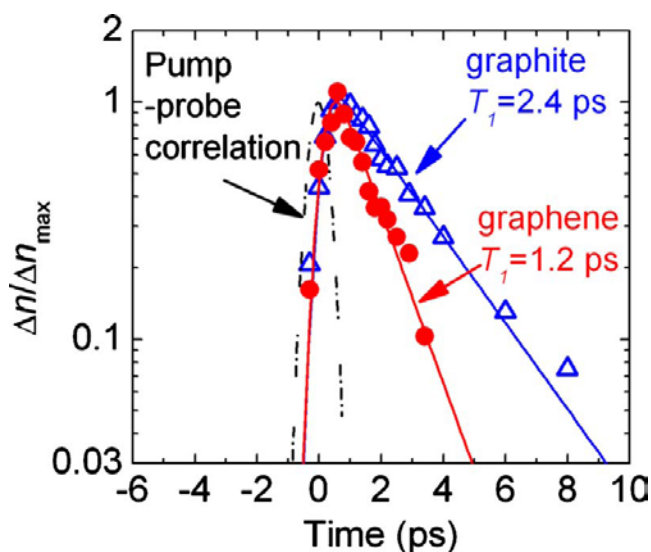
Figure 1.22 Normalized intensity change of anti-Stokes G band Raman scattering in graphite and monolayer graphene at room temperature as a function of delay time t. The intensity of Raman signal is proportional to the G-phonon population. Symbols and solid lines are experimental data and model fits, respectively. The extracted exponential relaxation times for graphite and monolayer graphene from these fits are 2.4 and 1.2 ps, respectively. The black dashed-dot line is the time correlation between the pump and probe pulses. The figure is adapted from ref.[99].
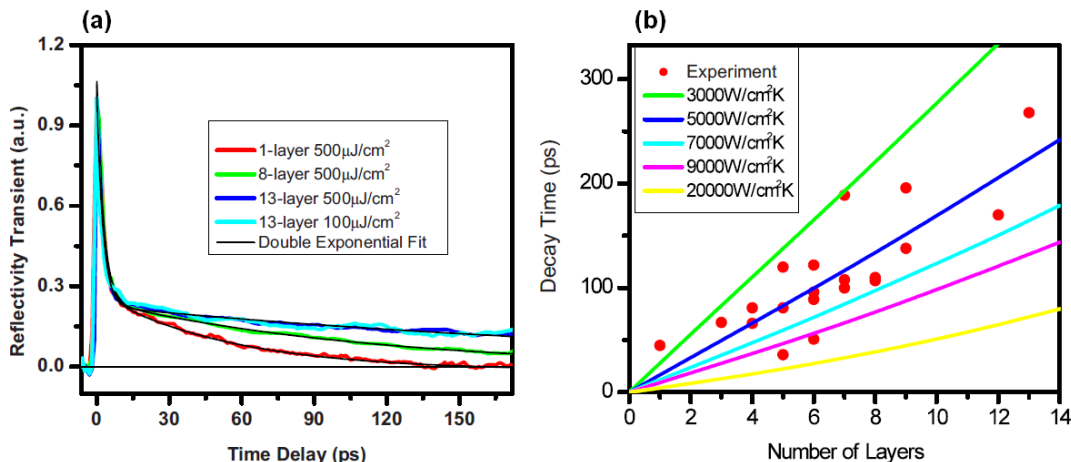
Figure 1.23 (a) Transient reflectivity decay dynamics of mono-, 8- and 13-layer graphene samples, together with double exponential fits to the data. The decay dynamics for the 13-layer graphene sample is plotted for two different pump fluences. After rescaling, identical decay dynamics are observed. **(b)** Decay time for interfacial heat flow as a function of graphene layer thickness. Dots: experimental data, with multiple points corresponding to values for different samples of the given thickness. Lines: numerical simulations, for different values of the interfacial thermal conductance. The figures are adapted from ref.[102].

phonons in the time scale of a few picoseconds.

After the charge carriers and SCOP reach equilibrium with the lattice, the whole graphene system will cool down slowly by heat diffusion into the substrate in a time scale of 10's picoseconds. This relaxation process can be probed by measuring graphene's transient reflectivity [Figure 1.23(a)] [102]. Lateral heat diffusion is negligible in this time scale due to the large laser spot (a few micrometers) in the pump-probe experiment. In addition, since the heat is dissipated across the interface between graphene and the substrate, thicker graphene samples usually needs a longer time to cool down. By analyzing the layer-thickness dependence of the relaxation time based on a model of heat diffusion across an interface, we can extract the interfacial thermal conductance between graphene and the substrate. For graphene deposited on SiO_2 substrates, the average interfacial thermal conductance is found to be 5,000 W/cm^{2}K [Figure 1.23 (b)].

1.9 Morphology of Graphene

While much of the graphene research has been directed to investigate its electronic and vibrational properties, the structural aspect of this two-dimensional material is also of interest and importance. The morphology of graphene started to attract attention in 2007, when Mayer *et al* [103] reported the presence of nanometer-sized ripples in single-layer graphene by an electron diffraction study on the suspended graphene membranes [Figure 1.24]. They found that the electron diffraction pattern becomes blurred when the incident angle of the electron beam increases. Such broadening of diffraction peaks with the tilt angle can be understood as a result of microscopic corrugations on the graphene plane. They further deduced that the graphene ripples have an average height of ~1nm and lateral dimension of 10~25 nm. The rippling
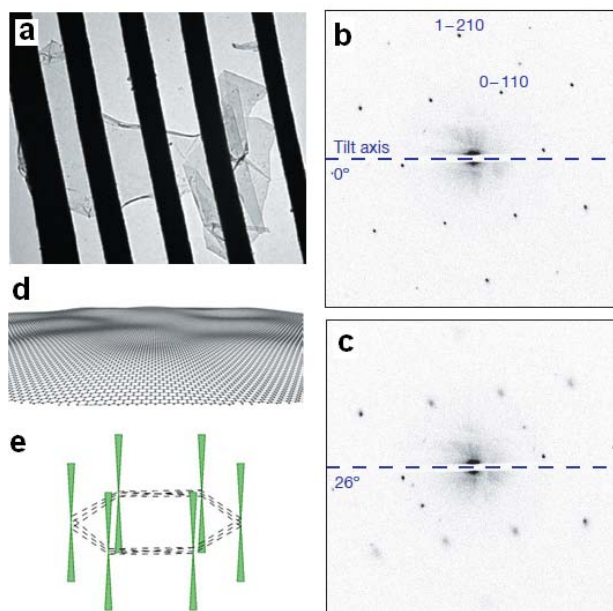
Figure 1.24 (a) TEM image of a suspended graphene membrance. **(b) (c)** Electronc diffraction patterns from a graphene monolayer under incidence angles of 0 (b) and 26 (c) degree. The peaks become broader with increasing tilt angle. **(d)** Schematic for a corrugated graphene. **(e)** For the corrugated sheet, a superposition of the diffracting beams from microscopic flat areas effectively turns the rods into cone-shaped volumes so that diffration spots become blurred at large angles. The figure is adapted from ref.[103].

was found to be suppressed in graphene samples with greater thickness. The nanoscale rippling has been argued to be an intrinsic feature of graphene, which is necessary to maintain the stability of graphene's 2D structure [103,104].

In addition to the studies of free-standing graphene layers, the vast majority of investigations have been conducted for single-layer graphene crystals deposited on silicon wafers with SiO_2 epilayers. These graphene samples also display nanometer roughness over a lateral scale of a few 10's of nanometers [16,105], features comparable to those found in free-standing graphene layers. It has been an issue of controversy whether these corrugations arise from the effects of the rough underlying substrates or they are the intrinsic features of graphene.

The existence of microscopic rippling of the 2D graphene sheets, either in free-standing form or supported on substrates, has attracted intense scientific interest. Beside its importance for the fundamental questions concerning the stability of 2D systems, the ripples are understood to define a diverse set of the observed properties of graphene. The higher chemical reactivity seen in single layer graphene compared with bi- or multilayer
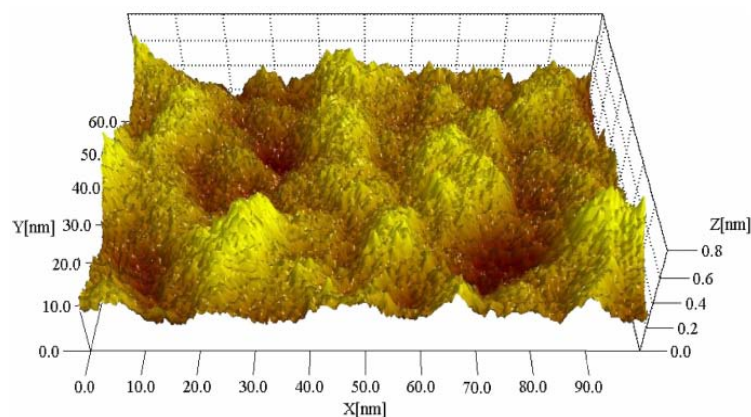
Figure 1.25 Stereographic plot of a large-scale (100 x 62 nm) STM image of a single-layer graphene film on the SiO_2 surface. The height variation on graphene is ~0.5nm over a lateral distance of 10~20 nm. The figure is adapted from ref.[16].

graphene has, for instance, been attributed to changes in chemical bonding caused by ripples. In addition, ripples can induce additional scattering processes and charge inhomogeneities that limit the ultimate carrier mobility in graphene [106]. Furthermore, various theoretical studies have predicted that the ripples can induce a zero-energy landau level in graphene [42,107]. The associated energy states, i.e. the so called mid-gap states, can localize the charge carriers and increase the resistance of the graphene sheets.

1.10 Structure of the thesis

This thesis is devoted to investigating the electronic, vibrational and structural properties of single and few layer graphene. The thesis can be divided into three sections.

The first section includes chapter 1 and 2 and introduces background information of the thesis. Chapter 1 overviews related graphene research in the literature. Chapter 2 presents experimental techniques and apparatuses that are applied in the research of the thesis.

The second section includes chapter 3 and 4 and is devoted to the investigations of single-layer graphene (SLG). Chapter 3 mainly focuses on the structural properties of SLG. We compare graphene's morphology on different substrates and demonstrate how to produce ultraflat graphene by using the atomically flat mica substrates. Chapter 4 focuses on the electronic and optical properties of SLG. We study the ultrafast carrier dynamics in graphene by using the optical emission of the hot carriers in graphene with the excitation of femtosecond laser.

The third second includes chapter 5, 6 and 7 and is devoted to the studies of few-layer graphene (FLG). In Chapter 5, we demonstrate how to characterize the stacking

order of FLG by Raman imaging. In chapter 6, we investigate the influence of stacking order on the possibility of opening a band gap in ABA and ABC stacked trilayer graphene. Finally, we investigate the influence of stacking order on the Raman response of FLG in chapter 7.

References

[1]   A. K. Geim & K. S. Novoselov. "The rise of graphene", *Nat. Mater.* **6**, 183, (2007).

[2]   A. K. Geim. "Graphene: Status and Prospects", *Science* **324**, 1530-1534, (2009).

[3]   P. R. Wallace. "The band theory of graphite", *Physical Review* **71**, 622-634, (1947).

[4]   F. D. M. Haldane. "Model for a Quantum Hall Effect without Landau Levels: Condensed-Matter Realization of the "Parity Anomaly"", *Phys. Rev. Lett.* **61**, 2015, (1988).

[5]   Y. Zheng & T. Ando. "Hall conductivity of a two-dimensional graphite system", *Phys. Rev. B* **65**, 245420, (2002).

[6]   H. P. Boehm, A. Clauss, U. Hofmann & G. O. Fischer. "Dunnste kohlenstoff-folien", *Zeitschrift Fur Naturforschung* **B 17**, 150, (1962).

[7]   H. P. Boehm, R. Setton & E. Stumpp. "Nomenclature and terminology of graphite-intercalation compounds", *Pure Appl. Chem.* **66**, 1893, (1994).

[8]   I. Forbeaux, J. M. Themlin & J. M. Debever. "Heteroepitaxial graphite on 6H-SiC(0001): Interface formation through conduction-band electronic structure", *Phys. Rev. B* **58**, 16396, (1998).

[9]   A. J. Vanbommel, J. E. Crombeen & A. Vantooren. "LEED and Auger electron observations of the SiC(0001) surface ", *Surface Science* **48**, 463, (1975).

[10]   C. Oshima, A. Itoh, E. Rokuta, T. Tanaka, K. Yamashita & T. Sakurai. "A hetero-epitaxial-double-atomic-layer system of monolayer graphene/monolayer h-BN on Ni(111)", *Solid State Commun.* **116**, 37-40, (2000).

[11]   K. S. Novoselov, A. K. Geim, S. V. Morozov, D. Jiang, Y. Zhang, S. V. Dubonos, I. V. Grigorieva & A. A. Firsov. "Electric field effect in atomically thin carbon films", *Science* **306**, 666-669, (2004).

[12]   C. Berger, Z. M. Song, T. B. Li, X. B. Li, A. Y. Ogbazghi, R. Feng, Z. T. Dai, A. N. Marchenkov, E. H. Conrad, P. N. First & W. A. de Heer. "Ultrathin epitaxial graphite: 2D electron gas properties and a route toward graphene-based nanoelectronics", *J. Phys. Chem. B* **108**, 19912-19916, (2004).

[13]   Y. B. Zhang, J. P. Small, M. E. S. Amori & P. Kim. "Electric field modulation of galvanomagnetic properties of mesoscopic graphite", *Phys. Rev. Lett.* **94**, (2005).

[14]   Y. Zhang, J. P. Small, M. E. S. Amori & P. Kim. "Electric Field Modulation of Galvanomagnetic Properties of Mesoscopic Graphite", *Phys. Rev. Lett.* **94**, 176803, (2005).

[15]   K. S. Novoselov, D. Jiang, F. Schedin, T. J. Booth, V. V. Khotkevich, S. V. Morozov & A. K. Geim. "Two-dimensional atomic crystals", *Proc. Natl. Acad. Sci. U. S. A.* **102**, 10451-10453, (2005).

[16]   E. Stolyarova, K. T. Rim, S. M. Ryu, J. Maultzsch, P. Kim, L. E. Brus, T. F. Heinz, M. S. Hybertsen & G. W. Flynn. "High-resolution scanning tunneling microscopy imaging of mesoscopic graphene sheets on an insulating surface", *Proc. Natl. Acad. Sci. U. S. A.* **104**, 9209-9212, (2007).

[17]   K. S. Novoselov, A. K. Geim, S. V. Morozov, D. Jiang, M. I. Katsnelson, I. V. Grigorieva, S. V. Dubonos & A. A. Firsov. "Two-dimensional gas of massless Dirac fermions in graphene", *Nature* **438**, 197-200, (2005).

[18]   Y. B. Zhang, Y. W. Tan, H. L. Stormer & P. Kim. "Experimental observation of the quantum Hall effect and Berry's phase in graphene", *Nature* **438**, 201-204, (2005).

[19]   A. H. Castro Neto, F. Guinea, N. M. R. Peres, K. S. Novoselov & A. K. Geim. "The electronic properties of graphene", *Rev. Mod. Phys.* **81**, 109, (2009).

[20]   O. Klein. "Die reflexion von elektronen an einem potentialsprung nach der relativistischen dynamik von Dirac.", *Z Phys.* **53**, 157-165, (2009).

[21]   A. F. Young & P. Kim. "Quantum interference and Klein tunnelling in graphene heterojunctions", *Nat. Phys.* **5**, 222-226, (2009).

[22]   M. I. Katsnelson, K. S. Novoselov & A. K. Geim. "Chiral tunnelling and the Klein paradox in graphene", *Nat. Phys.* **2**, 620-625, (2006).

[23]   K. I. Bolotin, K. J. Sikes, Z. Jiang, M. Klima, G. Fudenberg, J. Hone, P. Kim & H. L. Stormer. "Ultrahigh electron mobility in suspended graphene", *Solid State Commun.* **146**, 351-355, (2008).

[24]   X. Du, I. Skachko, A. Barker & E. Y. Andrei. "Approaching ballistic transport in suspended graphene", *Nat. Nanotechnol.* **3**, 491-495, (2008).

[25]   K. S. Novoselov, Z. Jiang, Y. Zhang, S. V. Morozov, H. L. Stormer, U. Zeitler, J. C. Maan, G. S. Boebinger, P. Kim & A. K. Geim. "Room-temperature quantum hall effect in graphene", *Science* **315**, 1379-1379, (2007).

[26]   X. Du, I. Skachko, F. Duerr, A. Luican & E. Y. Andrei. "Fractional quantum Hall effect and insulating phase of Dirac electrons in graphene", *Nature* **462**, 192-195, (2009).

[27]   K. I. Bolotin, F. Ghahari, M. D. Shulman, H. L. Stormer & P. Kim. "Observation of the fractional quantum Hall effect in graphene", *Nature* **462**, 196-199, (2009).

[28]   N. Tombros, C. Jozsa, M. Popinciuc, H. T. Jonkman & B. J. van Wees. "Electronic spin transport and spin precession in single graphene layers at room temperature", *Nature* **448**, 571-574, (2007).

[29]   R. R. Nair, P. Blake, A. N. Grigorenko, K. S. Novoselov, T. J. Booth, T. Stauber, N. M. R. Peres & A. K. Geim. "Fine structure constant defines visual transparency of graphene", *Science* **320**, 1308-1308, (2008).

[30]   K. F. Mak, M. Y. Sfeir, Y. Wu, C. H. Lui, J. A. Misewich & T. F. Heinz. "Measurement of the Optical Conductivity of Graphene", *Phys. Rev. Lett.* **101**, 196405, (2008).

[31]   F. Wang, Y. B. Zhang, C. S. Tian, C. Girit, A. Zettl, M. Crommie & Y. R. Shen. "Gate-variable optical transitions in graphene", *Science* **320**, 206-209, (2008).

[32]   Z. Q. Li, E. A. Henriksen, Z. Jiang, Z. Hao, M. C. Martin, P. Kim, H. L. Stormer & D. N. Basov. "Dirac charge dynamics in graphene by infrared spectroscopy", *Nat. Phys.* **4**, 532-535, (2008).

[33]   C. Lee, X. D. Wei, J. W. Kysar & J. Hone. "Measurement of the elastic properties and intrinsic strength of monolayer graphene", *Science 321*, 385, (2008).

[34]   J. S. Bunch, A. M. van der Zande, S. S. Verbridge, I. W. Frank, D. M. Tanenbaum, J. M. Parpia, H. G. Craighead & P. L. McEuen. "Electromechanical resonators from graphene sheets", *Science* **315**, 490-493, (2007).

[35]   C. Y. Chen, S. Rosenblatt, K. I. Bolotin, W. Kalb, P. Kim, I. Kymissis, H. L. Stormer, T. F. Heinz & J. Hone. "Performance of monolayer graphene nanomechanical resonators with electrical readout", *Nat. Nanotechnol.* **4**, 861-867, (2009).

[36]   J. C. Meyer, C. O. Girit, M. F. Crommie & A. Zettl. "Imaging and dynamics of light atoms and molecules on graphene", *Nature* **454**, 319-322, (2008).

[37]   K. Xu, P. G. Cao & J. R. Heath. "Graphene Visualizes the First Water Adlayers on Mica at Ambient Conditions", *Science* **329**, 1188-1191, (2010).

[38]   H. W. C. Postma. "Rapid Sequencing of Individual DNA Molecules in Graphene Nanogaps", *Nano Lett.* **10**, 420-425, (2010).

[39]   S. Garaj, W. Hubbard, A. Reina, J. Kong, D. Branton & J. A. Golovchenko. "Graphene as a subnanometre trans-electrode membrane", *Nature* **467**, 190, (2010).

[40]   C. A. Merchant, K. Healy, M. Wanunu, V. Ray, N. Peterman, J. Bartel, M. D. Fischbein, K. Venta, Z. T. Luo, A. T. C. Johnson & M. Drndic. "DNA Translocation through Graphene Nanopores", *Nano Lett.* **10**, 2915-2921, (2010).

[41]   F. Guinea, M. I. Katsnelson & A. K. Geim. "Energy gaps and a zero-field quantum Hall effect in graphene by strain engineering", *Nat. Phys.* **6**, 30-33, (2010).

[42]   F. Guinea, M. I. Katsnelson & M. A. H. Vozmediano. "Midgap states and charge inhomogeneities in corrugated graphene", *Phys. Rev. B* **77**, 8, (2008).

[43]   N. Levy, S. A. Burke, K. L. Meaker, M. Panlasigui, A. Zettl, F. Guinea, A. H. C. Neto & M. F. Crommie. "Strain-Induced Pseudo-Magnetic Fields Greater Than 300 Tesla in Graphene Nanobubbles", *Science* **329**, 544-547, (2010).

[44]   M. Y. Huang, H. G. Yan, C. Y. Chen, D. H. Song, T. F. Heinz & J. Hone. "Phonon softening and crystallographic orientation of strained graphene studied by Raman spectroscopy", *Proc. Natl. Acad. Sci. U. S. A.* **106**, 7304-7308, (2009).

[45]   T. M. G. Mohiuddin, A. Lombardo, R. R. Nair, A. Bonetti, G. Savini, R. Jalil, N. Bonini, D. M. Basko, C. Galiotis, N. Marzari, K. S. Novoselov, A. K. Geim & A. C. Ferrari. "Uniaxial strain in graphene by Raman spectroscopy: G peak splitting, Gruneisen parameters, and sample orientation", *Phys. Rev. B* **79**, 8, (2009).

[46]   F. Schwierz. "Graphene transistors", *Nat. Nanotechnol.* **5**, 487-496, (2010).

[47]   D. C. Elias, R. R. Nair, T. M. G. Mohiuddin, S. V. Morozov, P. Blake, M. P. Halsall, A. C. Ferrari, D. W. Boukhvalov, M. I. Katsnelson, A. K. Geim & K. S. Novoselov. "Control of Graphene's Properties by Reversible Hydrogenation: Evidence for Graphane", *Science* **323**, 610-613, (2009).

[48]   M. Y. Han, B. Ozyilmaz, Y. B. Zhang & P. Kim. "Energy band-gap engineering of graphene nanoribbons", *Phys. Rev. Lett.* **98**, 4, (2007).

[49]   J. M. Cai, P. Ruffieux, R. Jaafar, M. Bieri, T. Braun, S. Blankenburg, M. Muoth, A. P. Seitsonen, M. Saleh, X. L. Feng, K. Mullen & R. Fasel. "Atomically precise bottom-up fabrication of graphene nanoribbons", *Nature* **466**, 470-473, (2010).

[50]   Z. Q. Wei, D. B. Wang, S. Kim, S. Y. Kim, Y. K. Hu, M. K. Yakes, A. R. Laracuente, Z. T. Dai, S. R. Marder, C. Berger, W. P. King, W. A. de Heer, P. E. Sheehan & E. Riedo. "Nanoscale Tunable Reduction of Graphene Oxide for Graphene Electronics", *Science* **328**, 1373-1376, (2010).

[51]   X. L. Li, X. R. Wang, L. Zhang, S. W. Lee & H. J. Dai. "Chemically derived, ultrasmooth graphene nanoribbon semiconductors", *Science* **319**, 1229-1232, (2008).

[52]   D. V. Kosynkin, A. L. Higginbotham, A. Sinitskii, J. R. Lomeda, A. Dimiev, B. K. Price & J. M. Tour. "Longitudinal unzipping of carbon nanotubes to form graphene nanoribbons", *Nature* **458**, 872-875, (2009).

[53]   L. Y. Jiao, L. Zhang, X. R. Wang, G. Diankov & H. J. Dai. "Narrow graphene nanoribbons from carbon nanotubes", *Nature* **458**, 877-880, (2009).

[54]   G. M. Rutter, J. N. Crain, N. P. Guisinger, T. Li, P. N. First & J. A. Stroscio. "Scattering and interference in epitaxial graphene", *Science* **317**, 219-222, (2007).

[55]   C. Berger, Z. M. Song, X. B. Li, X. S. Wu, N. Brown, C. Naud, D. Mayou, T. B. Li, J. Hass, A. N. Marchenkov, E. H. Conrad, P. N. First & W. A. de Heer. "Electronic confinement and coherence in patterned epitaxial graphene", *Science* **312**, 1191-1196, (2006).

[56]   K. S. Kim, Y. Zhao, H. Jang, S. Y. Lee, J. M. Kim, J. H. Ahn, P. Kim, J. Y. Choi & B. H. Hong. "Large-scale pattern growth of graphene films for stretchable transparent electrodes", *Nature* ***457***, 706, (2009).

[57]   X. S. Li, W. W. Cai, J. H. An, S. Kim, J. Nah, D. X. Yang, R. Piner, A. Velamakanni, I. Jung, E. Tutuc, S. K. Banerjee, L. Colombo & R. S. Ruoff. "Large-Area Synthesis of High-Quality and Uniform Graphene Films on Copper Foils", *Science* ***324***, 1312, (2009).

[58]   Z. Sun, Z. Yan, J. Yao, E. Beitler, Y. Zhu & J. M. Tour. "Growth of graphene from solid carbon sources", *Nature* **468**, 549-552, (2010).

[59]   S. Bae, H. Kim, Y. Lee, X. F. Xu, J. S. Park, Y. Zheng, J. Balakrishnan, T. Lei, H. R. Kim, Y. I. Song, Y. J. Kim, K. S. Kim, B. Ozyilmaz, J. H. Ahn, B. H. Hong & S. Iijima. "Roll-to-roll production of 30-inch graphene films for transparent electrodes", *Nat. Nanotechnol.* **5**, 574-578, (2010).

[60]   J. Lahiri, Y. Lin, P. Bozkurt, Oleynik, II & M. Batzill. "An extended defect in graphene as a metallic wire", *Nat. Nanotechnol.* **5**, 326-329, (2010).

[61]   P. Y. Huang, C. S. Ruiz-Vargas, A. M. van der Zande, W. S. Whitney, M. P. Levendorf, J. W. Kevek, S. Garg, J. S. Alden, C. J. Hustedt, Y. Zhu, J. Park, P. L. McEuen & D. A. Muller. "Grains and grain boundaries in single-layer graphene atomic patchwork quilts", *Nature* **469**, 389-392, (2011).

[62]   K. S. Novoselov, E. McCann, S. V. Morozov, V. I. Fal'ko, M. I. Katsnelson, U. Zeitler, D. Jiang, F. Schedin & A. K. Geim. "Unconventional quantum Hall effect and Berry's phase of 2 pi in bilayer graphene", *Nat. Phys.* **2**, 177-180, (2006).

[63]   E. McCann & V. I. Fal'ko. "Landau-level degeneracy and quantum hall effect in a graphite bilayer", *Phys. Rev. Lett.* **96**, (2006).

[64]   K. F. Mak, C. H. Lui, J. Shan & T. F. Heinz. "Observation of an Electric-Field-Induced Band Gap in Bilayer Graphene by Infrared Spectroscopy", *Phys. Rev. Lett.* **102**, 256405, (2009).

[65]   Y. B. Zhang, T. T. Tang, C. Girit, Z. Hao, M. C. Martin, A. Zettl, M. F. Crommie, Y. R. Shen & F. Wang. "Direct observation of a widely tunable bandgap in bilayer graphene", *Nature **459***, 820, (2009).

[66]   J. C. Slonczewski & P. R. Weiss. "Band structure of graphite", *Physical Review* **109**, 272-279, (1958).

[67]   M. Mecklenburg & B. C. Regan. *arXiv:1003.3715v3*, (2010).

[68]   V. P. Gusynin, S. G. Sharapov & J. P. Carbotte. "Unusual microwave response of Dirac quasiparticles in graphene", *Phys. Rev. Lett.* **96**, (2006).

[69]   T. Ando, Y. S. Zheng & H. Suzuura. "Dynamical conductivity and zero-mode anomaly in honeycomb lattices", *J. Phys. Soc. Jpn.* **71**, 1318-1324, (2002).

[70]   D. S. L. Abergel & V. I. Fal'ko. "Optical and magneto-optical far-infrared properties of bilayer graphene", *Phys. Rev. B* **75**, (2007).

[71]   V. P. Gusynin & S. G. Sharapov. "Transport of Dirac quasiparticles in graphene: Hall and optical conductivities", *Phys. Rev. B* **73**, (2006).

[72]   T. Stauber, N. M. R. Peres & A. K. Geim. "Optical conductivity of graphene in the visible region of the spectrum", *Phys. Rev. B* **78**, 085432, (2008).

[73]   L. Yang, J. Deslippe, C. H. Park, M. L. Cohen & S. G. Louie. "Excitonic Effects on the Optical Response of Graphene and Bilayer Graphene", *Phys. Rev. Lett.* **103**, (2009).

[74]   K. F. Mak. *Probing the electronic properties of atomically thin graphitic layers with optical spectroscopy (phD dissertation)*, Columbia University (2010).

[75]   V. G. Kravets, A. N. Grigorenko, R. R. Nair, P. Blake, S. Anissimova, K. S. Novoselov & A. K. Geim. "Spectroscopic ellipsometry of graphene and an exciton-shifted van Hove peak in absorption", *Phys. Rev. B* **81**, 155413, (2010).

[76]   M. Aoki & H. Amawashi. "Dependence of band structures on stacking and field in layered graphene", *Solid State Commun.* **142**, 123, (**2007**).

[77]   L. M. Zhang, Z. Q. Li, D. N. Basov, M. M. Fogler, Z. Hao & M. C. Martin. "Determination of the electronic structure of bilayer graphene from infrared spectroscopy", *Phys. Rev. B* **78**, 11, (2008).

[78]   H. Min, B. Sahu, S. K. Banerjee & A. H. MacDonald. "Ab initio theory of gate induced gaps in graphene bilayers", *Phys. Rev. B* **75**, 155115, (2007).

[79]   E. McCann. "Asymmetry gap in the electronic band structure of bilayer graphene", *Phys. Rev. B* **74**, (2006).

[80]   E. V. Castro, K. S. Novoselov, S. V. Morozov, N. M. R. Peres, J. M. B. L. dos Santos, J. Nilsson, F. Guinea, A. K. Geim & A. H. C. Neto. "Biased Bilayer Graphene: Semiconductor with a Gap Tunable by the Electric Field Effect", *Phys. Rev. Lett.* **99**, 216802, (2007).

[81]   E. J. Nicol & J. P. Carbotte. "Optical conductivity of bilayer graphene with and without an asymmetry gap", *Phys. Rev. B* **77**, 155409, (2008).

[82]   L. Jing, J. Velasco, P. Kratz, G. Liu, W. Z. Bao, M. Bockrath & C. N. Lau. "Quantum Transport and Field-Induced Insulating States in Bilayer Graphene pnp Junctions", *Nano Lett.* **10**, 4000-4004, (2010).

[83]   J. B. Oostinga, H. B. Heersche, X. L. Liu, A. F. Morpurgo & L. M. K. Vandersypen. "Gate-induced insulating state in bilayer graphene devices", *Nat. Mater.* **7**, 151-157, (2008).

[84]   F. N. Xia, D. B. Farmer, Y. M. Lin & P. Avouris. "Graphene Field-Effect Transistors with High On/Off Current Ratio and Large Transport Band Gap at Room Temperature", *Nano Lett.* **10**, 715-718, (2010).

[85]   R. T. Weitz, M. T. Allen, B. E. Feldman, J. Martin & A. Yacoby. "Broken-Symmetry States in Doubly Gated Suspended Bilayer Graphene", *Science* **330**, 812-816.

[86]   T. Ohta, A. Bostwick, T. Seyller, K. Horn & E. Rotenberg. "Controlling the electronic structure of bilayer graphene", *Science* **313**, 951-954, (2006).

[87]   Z. Q. Li, E. A. Henriksen, Z. Jiang, Z. Hao, M. C. Martin, P. Kim, H. L. Stormer & D. N. Basov. "Band Structure Asymmetry of Bilayer Graphene Revealed by Infrared Spectroscopy", *Phys. Rev. Lett.* **102**, 4, (2009).

[88]   A. C. Ferrari. "Raman spectroscopy of graphene and graphite: Disorder, electron-phonon coupling, doping and nonadiabatic effects", *Solid State Commun.* **143**, 47, (2007).

[89]   L. M. Malard, M. A. Pimenta, G. Dresselhaus & M. S. Dresselhaus. "Raman spectroscopy in graphene", *Phys. Rep.* **473**, 51, (2009).

[90]   S. Piscanec, M. Lazzeri, F. Mauri, A. C. Ferrari & J. Robertson. "Kohn anomalies and electron-phonon interactions in graphite", *Phys. Rev. Lett.* **93**, 185503, (2004).

[91]   T. Kampfrath, L. Perfetti, F. Schapper, C. Frischkorn & M. Wolf. "Strongly coupled optical phonons in the ultrafast dynamics of the electronic energy and current relaxation in graphite", *Phys. Rev. Lett.* **95**, 187403, (2005).

[92]   H. G. Yan, D. H. Song, K. F. Mak, I. Chatzakis, J. Maultzsch & T. F. Heinz. "Time-resolved Raman spectroscopy of optical phonons in graphite: Phonon anharmonic coupling and anomalous stiffening", *Phys. Rev. B* **80**, 121403, (2009).

[93]   C. H. Lui, K. F. Mak, J. Shan & T. F. Heinz. "Ultrafast Photoluminescence from Graphene", *Phys. Rev. Lett.* **105**, 4, (2010).

[94]   A. Das, S. Pisana, B. Chakraborty, S. Piscanec, S. K. Saha, U. V. Waghmare, K. S. Novoselov, H. R. Krishnamurthy, A. K. Geim, A. C. Ferrari & A. K. Sood. "Monitoring dopants by Raman scattering in an electrochemically top-gated graphene transistor", *Nat. Nanotechnol.* **3**, 210, (2008).

[95]   S. Pisana, M. Lazzeri, C. Casiraghi, K. S. Novoselov, A. K. Geim, A. C. Ferrari & F. Mauri. "Breakdown of the adiabatic Born-Oppenheimer approximation in graphene", *Nat. Mater.* **6**, 198-201, (2007).

[96]   J. Yan, Y. B. Zhang, P. Kim & A. Pinczuk. "Electric field effect tuning of electron-phonon coupling in graphene", *Phys. Rev. Lett.* **98**, 166802, (2007).

[97]   C. Thomsen & S. Reich. "Double resonant Raman scattering in graphite", *Phys. Rev. Lett.* **85**, 5214, (2000).

[98]   A. C. Ferrari, J. C. Meyer, V. Scardaci, C. Casiraghi, M. Lazzeri, F. Mauri, S. Piscanec, D. Jiang, K. S. Novoselov, S. Roth & A. K. Geim. "Raman spectrum of graphene and graphene layers", *Phys. Rev. Lett.* **97**, (2006).

[99]   K. Kang, D. Abdula, D. G. Cahill & M. Shim. "Lifetimes of optical phonons in graphene and graphite by time-resolved incoherent anti-Stokes Raman scattering", *Phys. Rev. B* **81**, 6, (2010).

[100]   K. Ishioka, M. Hase, M. Kitajima, L. Wirtz, A. Rubio & H. Petek. "Ultrafast electron-phonon decoupling in graphite", *Phys. Rev. B* **77**, 121402, (2008).

[101]   D. H. Song, F. Wang, G. Dukovic, M. Zheng, E. D. Semke, L. E. Brus & T. F. Heinz. "Direct measurement of the lifetime of optical phonons in single-walled carbon nanotubes", *Phys. Rev. Lett.* **100**, 225503, (2008).

[102]   K. F. Mak, C. H. Lui & T. F. Heinz. "Measurement of the thermal conductance of the graphene/SiO2 interface", *App. Phys. Lett.* **97**, 221904 (2010).

[103]   J. C. Meyer, A. K. Geim, M. I. Katsnelson, K. S. Novoselov, T. J. Booth & S. Roth. "*The structure of suspended graphene sheets*", *Nature* **446**, 60 - 63, (2007).

[104]   A. Fasolino, J. H. Los & M. I. Katsnelson. "Intrinsic ripples in graphene", *Nature Mater.* **6**, 858-861, (2007).

[105]   M. Ishigami, J. H. Chen, W. G. Cullen, M. S. Fuhrer & E. D. Williams. "Atomic structure of graphene on SiO$_2$", *Nano Lett.* **7**, 1643-1648, (2007).

[106]   M. I. Katsnelson & A. K. Geim. "Electron scattering on microscopic corrugations in graphene", *Phil. Trans. R. Soc. A* **366**, 195-204, (2008).

[107]   F. Guinea, B. Horovitz & P. Le Doussal. "Gauge field induced by ripples in graphene", *Phys. Rev. B* **77**, 205421, (2008).

Chapter 2

Experimental Techniques and Apparatuses

In this chapter, I introduce some techniques and apparatuses for the experiments in this thesis. The techniques include the isolation of single-layer and few-layer graphene (SLG and FLG) from graphite and characterization of the sample thickness. I also explain the experimental setups of Raman, infrared (IR) and photoluminescence spectroscopy on graphene.

2.1 Graphene Sample Preparations

All the graphene samples used in the experiments in this thesis are produced by mechanical exfoliation of kish graphite, which is also called the scotch-tape method [1]. This technique has been widely applied in the graphene community. Though other methods such as chemical vapour deposition have been developed for the massive production of large-scale graphene samples, the scotch-tape method remains as a vital technique in graphene research because it is very simple and the graphene samples thus produced has the highest quality among all the sample preparation methods.

In the scotch-tape method, a piece of kish graphite flake is put on the tape and peeled with another tape. Since the graphene layers in graphite are bonded only weakly by the van der Waals force, they can be readily separated. The peeling process is repeated until the tape is full of thin graphite flakes. Afterward, the tape is transferred onto a

substrate. After being rubbed softly against the substrate surface for about one minute, the tape is removed and some graphene flakes will remain on the substrate.

The yield of graphene sheets is mainly determined by two factors in the sample preparation process. The first one is the distribution of graphite flakes on the tape. To obtain large-area graphene sheets, the graphite flakes on the tape should be thin, large and dense. During the peeling process, the graphite distribution should be monitored continuously by checking the tape under the light. Graphite thin films appear to be half-transparent. Overdoing the peeling process usually results in powder-like graphite distribution on the tape, which would not be able to produce large graphene samples. The second factor is a clean substrate. We usually clean the quartz substrates and silicon wafer by etching in nano-strip or piranha for half an hour. Methanol is sometimes used to clean the substrates, but it appears to be less effective.

After the exfoliation of graphite, we search the graphene flakes on the substrates under an optical microscope. When graphene is deposited on the silicon substrates with a 300-nm oxide layer, it appears to have different color from the substrate and hence can be visualized easily [Figure 2.1(a)]. Such a color contrast is induced by the extra optical path that graphene adds on the interference process in the oxide layer of the silicon substrate [1]. On the other hand, because graphene is very absorptive, it can also be inspected on the transparent substrates, such as quartz and mica, by using the optical intensity contrast of reflection (~8%) between graphene and the substrate [Figure 2.1(b)].
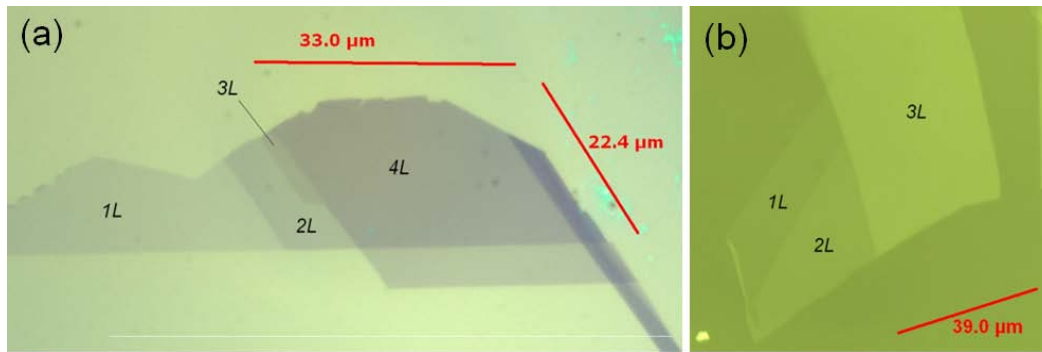
Figure 2.1 Optical images of single and few layer graphene on SiO$_2$/Si (**a**) and bulk SiO$_2$ (**b**) substrates.

Different kinds of substrates are used for different experimental purposes. The SiO$_2$/Si substrates are used most often in the graphene community because graphene can be visualized most easily by color contrast in these substrates and the oxide layer can be used as a gate to tune the doping level of graphene. However, SiO$_2$/Si substrates have some disadvantages in the optical measurement. First, the thin oxide layer complicated the optical problem in the graphene/substrate interface, which makes the extraction of optical conductivity less straightforward than in the case of bulk substrates. Second, silicon is opaque in wavelengths below 1.1 μm, resulting in difficulties in optical measurements in this spectral range. For instance, in the pump-probe experiment of graphene with Ti:sapphire laser as the excitation source, silicon will give a strong background response due to its absorption of the 800-nm incident laser. Therefore, we often use bulk substrates, such as quartz and mica that are transparent from IR to ultraviolet, in these optical measurements. Graphene on mica has ultraflat morphology and it can be produced with higher yield than on quartz because cleaved mica surface in

dry environment is very clean and adhesive. However, graphene on mica is often strongly

and inhomogeneously doped by the substrate as well as the adsorbates on the substrate.

The thickness of the graphene samples can be characterized accurately by several

methods, including atomic force microscopy (AFM), Raman spectroscopy and optical

absorption. AFM served as a vital tool to identify the graphene thickness in early

graphene research. In the AFM topological images, SLG exhibits a thickness of ~0.7-nm.

Each additional layer will add ~0.4 nm in the sample thickness. The larger thickness of

the first graphene layer is attributed to the graphene/substrate spacing. While the AFM

technique is accurate, it is not efficient and convenient. The AFM scanning can also

occasionally damage the graphene samples. Optical techniques have been developed to

characterize the graphene layer thickness in a more efficient way. In particular, Raman

spectroscopy can identify monolayer and bilayer graphene accurately by using their

unique Raman 2D-mode lineshapes (Figure 1.19) [2]. The Raman technique has been

used widely in the graphene community due to its simplicity. Its application is, however,

limited in FLG with layer thickness greater than two. For the thicker samples, we can

measure their layer number by optical absorption [3-5]. Because each graphene layer

absorbs about 2.3% of incident light in the near-infrared-to-visible range, we can deduce

the layer number of the FLG samples by the corresponding absorbance [Figure 2.2]. In

addition, graphene's reflectance is proportional to its absorption when it is deposited on

bulk transparent substrates. We can therefore also characterize FLG's layer number by

measuring the intensity of the reflected light [Figure 2.2(b)]. Similar techniques can be

used to identify the thickness of FLG in electron spectroscopy [6]. In some transport

experiments, the half-integer quantum Hall effect that is unique to monolayer graphene has also been used to identify the layer thickness of graphene [7,8].
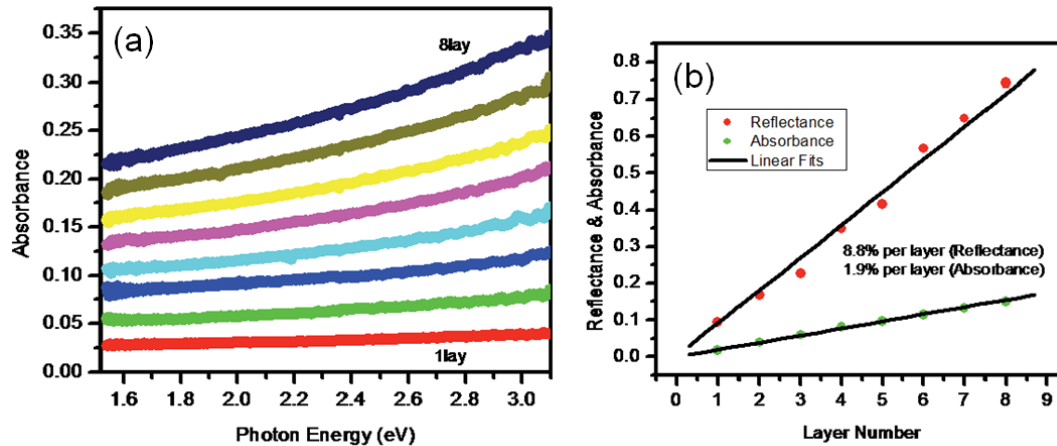
Figure 2.2 **(a)** Optical absorption spectra of FLG samples with layer number N from 1 to 8. **(b)** Average reflectance and absorbance of FLG as a function of layer number. The data can be described well with linear functions. The figures are adopted from ref.[5].

2.2 Raman Spectroscopy

In our experiments, Raman spectroscopy has been used extensively to study the electronic and vibrational properties of graphene samples. When the incident light is scattered from a crystal, most of the scattered photons have the same energy as the incident photons. This elastic scattering is called Rayleigh scattering. A tiny fraction of scattered photons have, however, lower energies than the incident photons because the scattering involves the excitation of some vibrational modes in the crystal. This inelastic scattering is called Raman scattering. Light sources in the infrared-to-ultraviolet spectral range are usually applied in Raman spectroscopy. Photons in this spectral range have very high energy, but negligible momentum compared to the phonons in the crystals. In order to conserve the total momentum in the scattering, the Raman process usually

involves only the emission of single phonons with zero momentum, i.e. zone-center phonons, or multiple phonons with total zero momentum. Exceptional cases happen when the crystals contain defects and disorders.

A typical Raman set up is shown schematically in Figure 2.3. The incident light, which is usually a 532-nm laser in our experiment, is focused on the sample with spot size of a few micrometers by a microscope objective. The scattered light from the sample is collected by the same objective and directed by a beam splitter to the spectrometer. A short-pass edge filter is used to block the strong elastically scattered light (Rayleigh-scattering) and pass only the weak Raman signals with lower photon energies. The spectrometer is coupled with a charge-coupled device (CCD) array detector, which is cooled either thermoelectrically or by liquid nitrogen. Figure 2.4 displays a typical Raman spectrum from SLG. The G and 2D line corresponds, respectively, to the emission of single zone-center phonons and two zone-edge phonons in graphene.
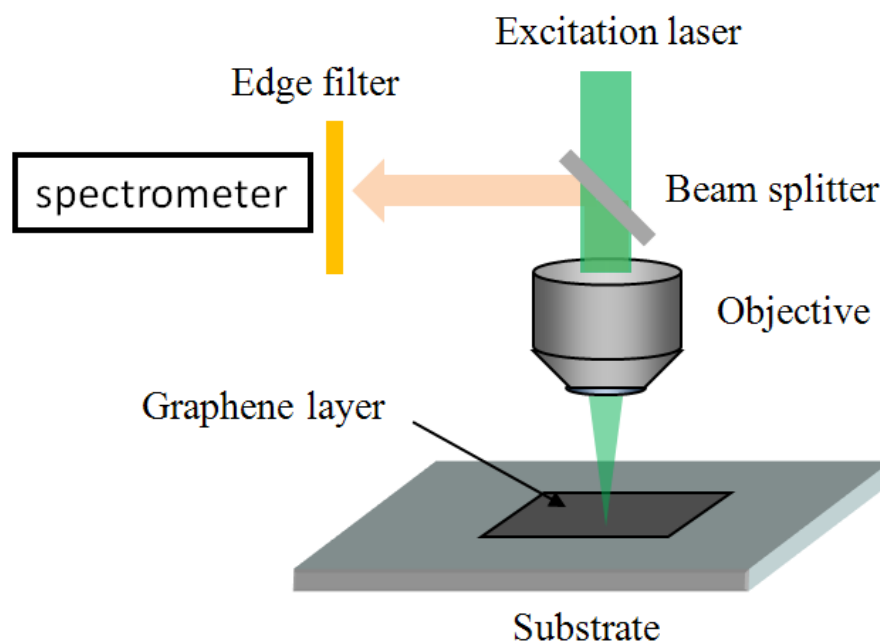
Figure 2.3 Schematic diagram of Raman measurement on graphene.
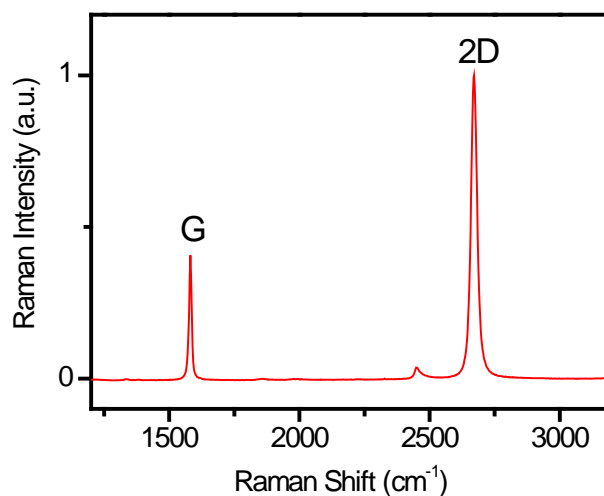
Figure 2.4 Raman spectrum of a single layer graphene.

2.3 Infrared Spectroscopy

In our experiments, we have studied the electronic structure of FLG by infrared (IR) spectroscopy. The IR measurements were performed by using either the Globar source or the U12 IR beam line of the National Synchrotron Light Source at Brookhaven national Laboratory. The optical radiation passing through or reflected by the sample was detected with a micro-Fourier Transform Infrared apparatus equipped with a liquid-nitrogen cooled MgCdTe detector under nitrogen purge.

A typical set up to measure the transmission of graphene samples is shown schematically in Figure 2.5. Since the exfoliated graphene samples are of length scale below 50 μm, the incident IR beam is focused on the sample with spot size about 10 μm by a reflective objective (x32). The transmission and reflectance spectra of the sample are obtained by normalizing the sample spectrum with that from the bare substrate. In my

experiment, I used both bulk SiO_2 substrates and silicon substrates with an oxide epilayer. They are both transparent in the infrared spectral range.
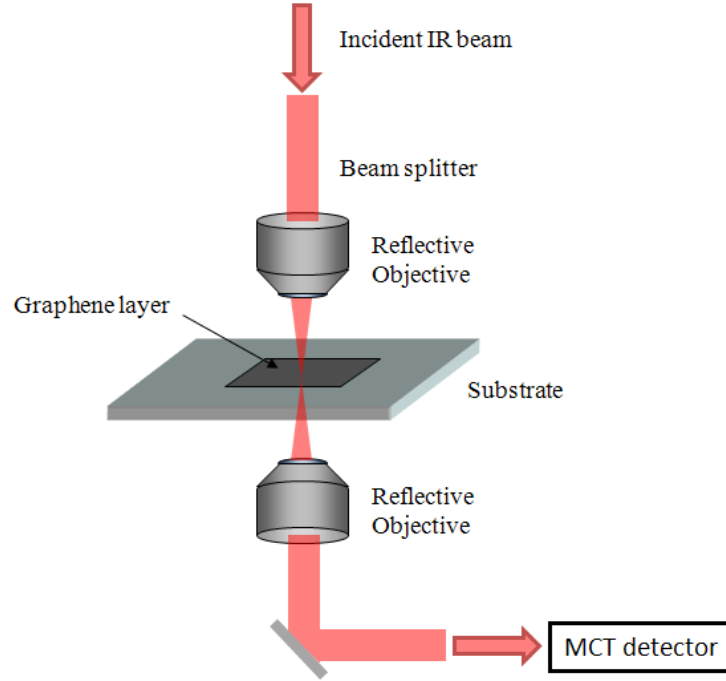
Figure 2.5 Schematic diagram of infrared measurement on graphene.

The optical sheet conductivity $\sigma(\hbar\omega)$ of the FLG samples can be calculated from the transmittance and reflectance by considering the boundary conditions in the graphene/substrate interface [9]. In the case of SiO_2/Si substrates, the calculations are somewhat complicated due to the interference in the oxide layer. However, in the case of bulk SiO_2 and mica substrates, the optical conductivity can be obtained from the fractional change of either the reflectance or transmittance using a simple formula [3]:

$$\delta_R = \frac{R_{FLG} - R_{sub}}{R_{sub}} = \frac{4}{n_{sub}^2 - 1}\frac{4\pi}{c}\sigma .$$
(3.1)

$$\delta_T = \frac{T_{FLG} - T_{sub}}{T_{sub}} = \frac{2}{n_{sub} + 1}\frac{4\pi}{c}\sigma .$$
(3.2)

Here R_{FLG} (T_{FLG}) and R_{sub} (T_{sub}) are the reflectance (transmittance) spectra of the FLG films on the quartz substrate and of the bare substrate, respectively. c denotes the speed of light in vacuum and n_{sub} is the frequency-dependent refractive index of the substrate. Figure 2.6 displays the IR optical conductivity of SLG and Bernal stacked bilayer and trilayer graphene on bulk quartz substrates. All samples exhibit relatively flat spectra in the high-energy spectral range. The conductivity value in this range is found to be proportional to the number of graphene layers and hence provides a precise identification of FLG thickness. On the other hand, the low-energy (< 0.7 eV) conductivity reflects the details of electronic structure and doping level [4,10,11].
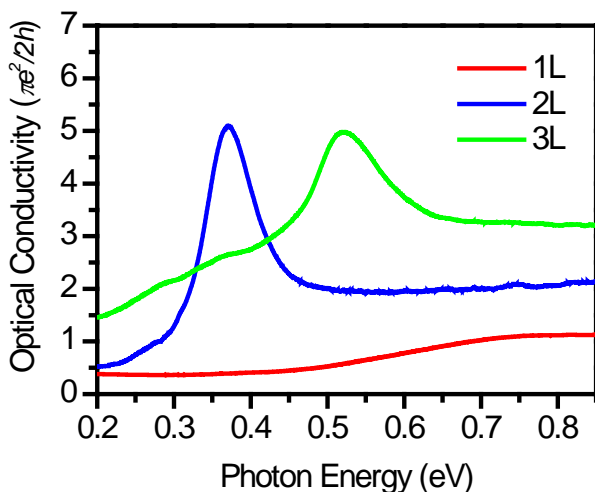
Figure 2.6 IR Optical conductivity of graphene samples with layer thickness N from 1 to 3.

2.4 Photoluminescence Spectroscopy and Two-Pulse Correlation Measurements

Apart from the Raman scattering and IR absorption, graphene also shows interesting properties in photoluminescence. Normally graphene does not emit any light due to the absence of band gap in this material. Any excited electron-hole pairs in graphene can relax and recombine rapidly through the emission of phonons. However, hot luminescence can occur in graphene with the excitation of femtosecond laser pulses. Investigation of the hot luminescence allows us to understand the ultrafast dynamics of excited carriers in graphene.

Figure 2.7 shows schematically the experimental setup for measuring optical emission from graphene. In our experiment, the laser pulses were generated from an 80-MHz modelocked Ti:sapphire oscillator. The central wavelength of the laser pulse was 830 nm. The spectral profile was Gaussian-shape with a spectral width of 27 nm [Figure 2.8(a)]. We measured the light emission from SLG under excitation both by individual pulses and by pairs of pulses. For the latter case, we recorded the light emission as a function of the temporal separation between two equivalent excitation pulses, which were orthogonally polarized to eliminate interference effects. In this two-pulse correlation measurement, the incident laser beam was split into two beams with different paths and recombined on the sample. One of the split beams was synchronized with another by a delay time, which was controlled by a translation stage equipped with a step motor of step size of 0.1 μm. In both single- and double-pulse excitation measurements, the light emission was collected in either transmission or reflection geometries and analyzed by a spectrometer coupled to a cooled CCD array detector.

To increase the time resolution of the measurement, we used a pair of prisms outside the oscillation cavity to compensate the dispersion in the optical path and

optimized the pulse duration at the sample position. We produced ultrashort pulses of duration ~30 fs in our experiment. The pulse duration was measured by using the intensity correlation of Second Harmonic Generation from a BBO crystal placed at the sample position [Figure 2.8(b)]. On the other hand, the beam on the sample plane was determined by scanning a sharp edge of a graphite flake across the laser spot. By differentiating the intensity of the reflected light with respect to the scan distance, we extracted the laser spot profile, which could be fit well with a Gaussian function and gave a spot diameter of ~ 5μm [Figure 2.9].
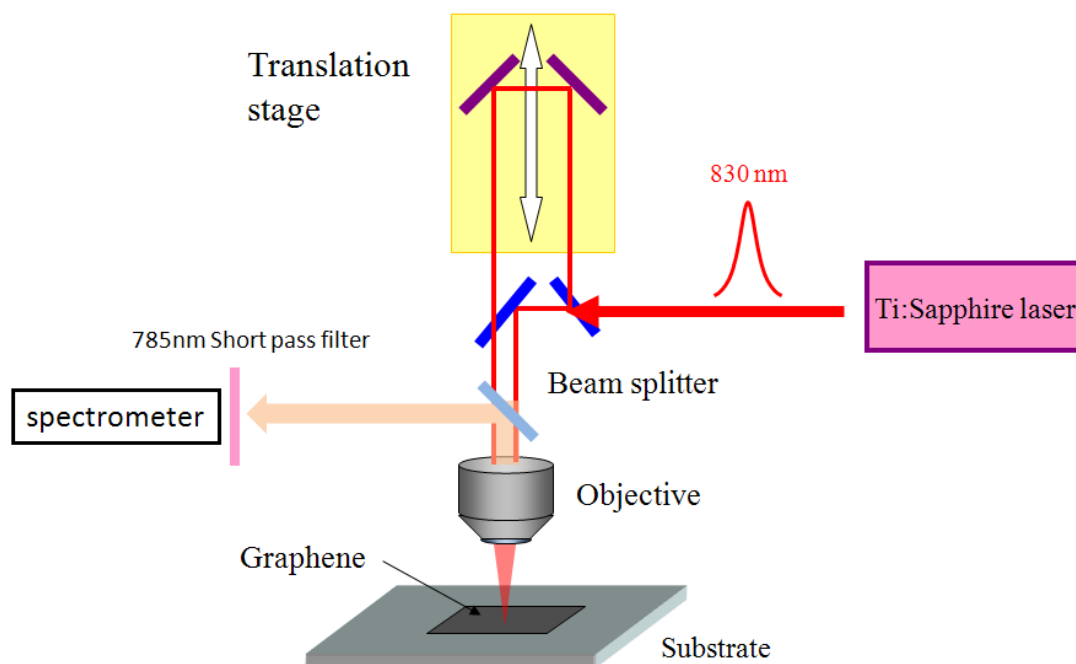
Figure 2.7 Schematic diagram of the setup for the two-pulse correlation measurement on the photoluminescence from graphene.
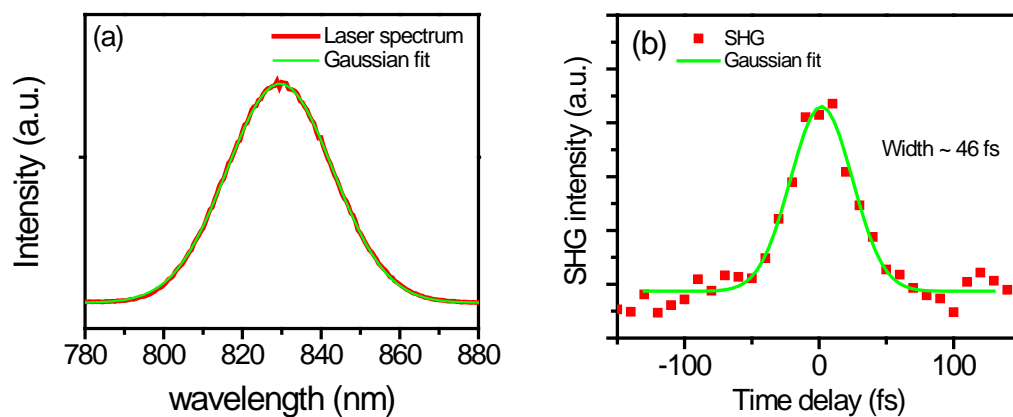
Figure 2.8 (a) Spectrum of the excitation laser (red line). The central wavelength is 830 nm and the spectral width is 27 nm with a Gaussian fit (green line). **(b)** The intensity of Second Harmonic Generation (SHG) as a function of temporal separation between two equivalent laser pulses (red squares). The correlation time is 46 fs by a Gaussian fit (green line). The pulse duration of each laser pulse is deduced to be $46/\sqrt{2}$ ~30 fs.
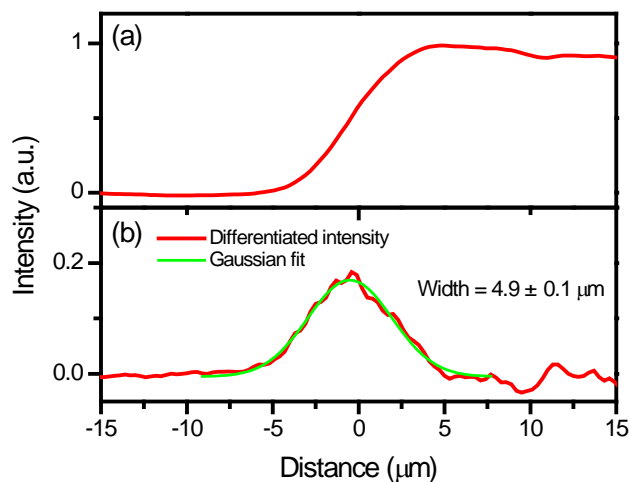
Figure 2.9 (a) Intensity of the reflected light as the edge of a graphite flake is scanned across the laser spot. **(b)** Differentiation of the intensity profile in (a). The spot diameter is estimated to be ~ 5 μm by a Gaussian fit (green line).

References

[1] K. S. Novoselov, D. Jiang, F. Schedin, T. J. Booth, V. V. Khotkevich, S. V. Morozov & A. K. Geim. "Two-dimensional atomic crystals", *Proc. Natl. Acad. Sci. U. S. A.* **102**, 10451-10453, (2005).

[2] A. C. Ferrari, J. C. Meyer, V. Scardaci, C. Casiraghi, M. Lazzeri, F. Mauri, S. Piscanec, D. Jiang, K. S. Novoselov, S. Roth & A. K. Geim. "Raman spectrum of graphene and graphene layers", *Phys. Rev. Lett.* **97**, (2006).

[3] K. F. Mak, M. Y. Sfeir, Y. Wu, C. H. Lui, J. A. Misewich & T. F. Heinz. "Measurement of the Optical Conductivity of Graphene", *Phys. Rev. Lett.* **101**, 196405, (2008).

[4] K. F. Mak, M. Y. Sfeir, J. A. Misewich & T. F. Heinz. "The evolution of electronic structure in few-layer graphene revealed by optical spectroscopy", *Proc. Natl. Acad. Sci. U. S. A. **107**, 14999, (**2010**).

[5] K. F. Mak. *Probing the electronic properties of atomically thin graphitic layers with optical spectroscopy (phD dissertation)*, Columbia University (2010).

[6] K. R. Knox, S. C. Wang, A. Morgante, D. Cvetko, A. Locatelli, T. O. Mentes, M. A. Nino, P. Kim & R. M. Osgood. "Spectromicroscopy of single and multilayer graphene supported by a weakly interacting substrate", *Phys. Rev. B* **78**, 201408, (2008).

[7] K. S. Novoselov, A. K. Geim, S. V. Morozov, D. Jiang, M. I. Katsnelson, I. V. Grigorieva, S. V. Dubonos & A. A. Firsov. "Two-dimensional gas of massless Dirac fermions in graphene", *Nature* **438**, 197-200, (2005).

[8] Y. B. Zhang, Y. W. Tan, H. L. Stormer & P. Kim. "Experimental observation of the quantum Hall effect and Berry's phase in graphene", *Nature* **438**, 201-204, (2005).

[9] E. Hecht. *Optics*. 3 edn, 419-420 (Addison Wesley, 1998).

[10] K. F. Mak, J. Shan & T. F. Heinz. "Electronic Structure of Few-Layer Graphene: Experimental Demonstration of Strong Dependence on Stacking Sequence", *Phys. Rev. Lett. **104**, 176404, (2010).

[11] K. F. Mak, C. H. Lui, J. Shan & T. F. Heinz. "Observation of an Electric-Field-Induced Band Gap in Bilayer Graphene by Infrared Spectroscopy", *Phys. Rev. Lett. **102**, 256405, (2009).

Chapter 3

Ultraflat Graphene on Mica Substrates

The morphology of high-quality graphene crystals has been the subject of much attention in graphene research. In this chapter, I present our investigation of the structure of single-layer graphene deposited on substrates with different flatness. We find that graphene is flexible and largely follows the morphology of the underlying supporting surface. In particular, graphene on the atomically flat surface of mica substrates exhibits an ultraflat morphology [1], one that is comparable to the morphology of cleaved graphite surface, indicating the suppression of any intrinsic corrugations of graphene.

3.1 Introduction

Graphene has stimulated intense scientific interest recently. While much of the research on graphene has been directed towards exploration of its novel electronic properties [2], the structural aspects of this model two-dimensional (2-D) system are also of great interest and importance. In particular, microscopic corrugations have been observed on all suspended [3] and supported [4-9] graphene sheets studied so far. Detailed electron-diffraction studies of free-standing graphene monolayers [3] indicate the presence of an intrinsic rippling, with ~1 nm high corrugations normal to the surface appearing over a characteristic lateral scale of 10 – 25 nm. It has been argued that these corrugations are necessary to stabilize the suspended graphene sheets against thermal instabilities present in ideal 2-D systems [10]. A comparable degree of height variation

has also been reported in several studies of graphene monolayers deposited on insulating substrates [4-9]. This rippling has been invoked to explain many phenomena observed in graphene, such as the formation of electron-hole puddles [11,12], the suppression of weak localization [13], decreased carrier mobility [14] and enhanced chemical reactivity [15-17]. In addition, theoretical studies of graphene have predicted that graphene ripples will induce fascinating new phenomena, including the enhancement of spin-orbit coupling [18], the generation of an inhomogeneous density of states and the formation of zero-energy Landau levels in the absence of magnetic fields [19-25]. While theoretical studies have been advanced, direct experimental study of such novel ripple physics has, however, been hindered by the lack of flat graphene layers.

In this chapter, we demonstrate the fabrication and characterization of high-quality ultraflat graphene monolayers by making use of a mica support that provides atomically flat terraces over large areas [1]. Using high-resolution, non-contact mode AFM to characterize the morphology, we find that graphene on mica approaches the limit of atomic flatness. The apparent height variation of graphene on mica is found to be < 25 pm over micron lateral length scales. This flatness, measured with a lateral spatial resolution of 7 nm, appears to be limited by instrument noise and is essentially identical (within 5 pm) to that observed for the surface of cleaved graphite crystals. Our results show that any intrinsic instability of graphene can be fully suppressed by deposition on an appropriate substrate. The availability of such a flat substance provides insight into questions of thermodynamic stability for this model 2-D system and a reference material to determine the role of ripples in the panoply of observed and predicted phenomena.

3.2 Experiment

3.2.1 Sample Preparation and Optical Characterization

The key to our experiments was the preparation of an atomically flat substrate for deposition of single-layer graphene crystals. For this purpose, we chose mica, a material composed of negatively charged aluminosilicate layers that are linked by single layers of potassium ions [26]. Since cleavage takes place readily along the potassium layer, atomically smooth surfaces with lateral dimensions as large as 100 μm can be routinely produced. In our study we made use of grade V-1 muscovite mica substrates (15x15 mm^2, from Structure Probe, Inc) and produced graphene layers by the standard method of mechanical exfoliation of kish graphite [27]. Mica surfaces are known to be hydrophilic and readily adsorb water and carbon dioxide, as well as hydrocarbons. To minimize the adsorbates at the graphene-mica interface, sample preparation was carried out in a glove box with water and oxygen concentrations below 1 ppm. For comparative studies, graphene monolayers were also prepared on bulk SiO_2 substrates. The SiO_2 substrates were carefully cleaned by sonication in methanol and the graphene samples were deposited by the same method of exfoliation of kish graphite, in this instance under ambient conditions. None of samples described in this chapter was subjected to any thermal processing.

Graphene monolayers were identified on the mica substrate by optical microscopy, which was performed under ambient conditions. Although more difficult than for graphene samples deposited on an optimized SiO_2 overlayer on a silicon substrate, we were able to identify graphene monolayers directly by visual inspection. The modulation in reflectivity from a graphene monolayer still amounts to ~ 8% (Figure 3.1). Raman

spectroscopy was applied for further characterization of the graphene samples [28] (Figure 3.2). From examination of the 2D Raman line, we confirmed the single-layer thickness of all the samples investigated in this chapter. Also the Raman spectra do not show any measurable D peak, indicating the high crystalline order of our samples. Our method of sample preparation was found to produce a significant yield of large graphene monolayers, with characteristic lateral dimensions ranging from tens of microns up to ~0.2 mm. The efficient deposition of large graphene single layers is attributed to the flat and clean surface of freshly cleaved mica.
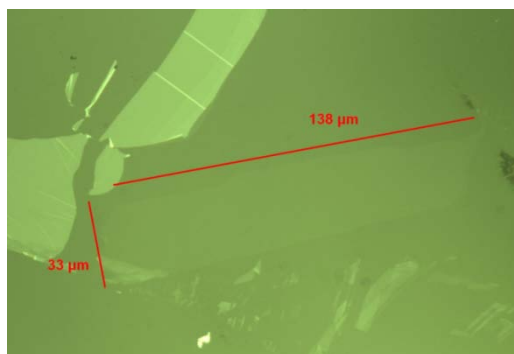
Figure 3.1 Image of a monolayer graphene sample on a mica substrate viewed by optical microscopy.
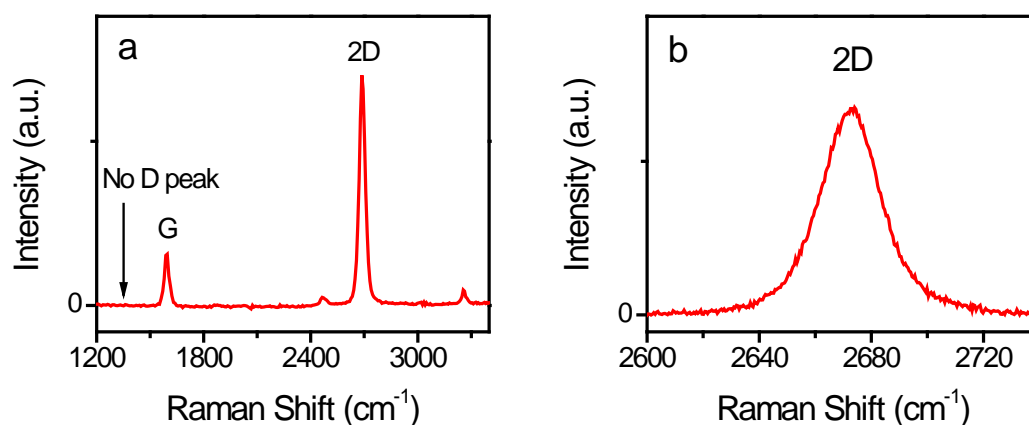
Figure 3.2 Raman spectra of the graphene monolayer in Figure 3.1 for an excitation wavelength of 532 nm. **(a)** The Raman spectrum does not show any measurable D peak, indicating the high crystalline order of the sample. **(b)** The 2D peak shows a narrow and symmetric profile, confirming that the sample is of monolayer thickness.

3.2.2 AFM Imaging

We employed amplitude-modulation AFM in non-contact mode to characterize the topography of the graphene samples. The measurements were performed under ambient conditions using an ultrasharp AFM tip (DP14/Hi'Res-C/AIBS from MikroMasch) that consisted of a silicon cantilever with hydrophobic diamond-like spikes at the apex of a silicon tip. Typical values for the force constant, resonant frequency, and probe tip radius were, respectively, 5 N/m, 200 kHz, and 1 nm. The AFM lateral resolution was determined experimentally by characterizing the edges of graphene monolayers on the mica substrate. The height profile of the edge was fit by a step function convoluted with a Gaussian instrumental response function. We defined the AFM lateral resolution as the full width at half maximum (FWHM) of this response function. For the images presented in this chapter, the instrumental resolution was found to be 7 nm. The height resolution was determined from residual noise in the AFM measurements. Using graphite surfaces as a reference, we found for our scanning conditions a root mean square height uncertainty of 23 pm.

In our quantitative analysis of the images, we have consistently used areas of $200{\times}200$ nm^2 size. The AFM topographic images displayed in this chapter are presented without filtering or smoothing. A third-order line and plane subtraction correction was applied to compensate for scanning drift and image bow. The roughness of the surface was characterized by the standard deviation σ of height distribution and the height correlation length l. We characterized the roughness of AFM topographic images by constructing a histogram of the measured heights and calculating the standard deviation σ of this distribution. These histograms could be fit well by single Gaussian functions (for

which the FWHM of the distribution is 2.36σ). Another useful description of the sample

topography was given by the correlation length *l* of the height profile. This parameter,

which defines the characteristic length of features observed in the AFM spatial images, is

determined using the height correlation function

$$C(r) = \frac{1}{2\pi} \int h(x', y') h(x' + r\cos\theta, y' + r\sin\theta) dx' dy' d\theta \qquad (3.1)$$

Where $h(x,y)$ denotes the height of the AFM image at location (x,y); and contributions

from different angles have been equally weighted. In evaluating this expression, we chose

the scale of the height function $h(x,y)$ so that its mean value vanishes, in which case

$\sigma = C(0)^{1/2}$. We then defined the correlation length *l* by requiring the correlation function

to drop to e^{-1} of its peak value at a displacement of half of a correlation length, *i.e., C(l/2)*

$= e^{-1}C(0)$.

3.3 Ultraflat Graphene on Mica Substrates

3.3.1 Morphology of Graphene on SiO$_2$ and Mica Substrates

AFM topographic images acquired for regions surrounding the edges of graphene

samples on both SiO$_2$ and mica substrates are shown in Figure 3.3(a, b). Histograms of

the corresponding height distribution over the 200x200 nm^2 regions of the surfaces are

presented in Figure 3.3(c). The height correlation functions of graphene on SiO$_2$ and

graphene on mica in the 200x200 nm^2 regions are presented in Figure 3.4. For the bare

SiO$_2$ surface, the parameters describing the height variation and correlation length (Table

3.1) are, respectively, σ = 168 pm and *l* = 16 nm. For the graphene monolayer on SiO$_2$,

we find a comparable (or slightly diminished) degree of roughness, with σ = 154 pm and

l = 22 nm, indicating that graphene monolayers largely follow the underlying substrate morphology.

In sharp contrast to these results, our AFM images on the mica substrate exhibit a much smoother landscape. For the bare mica surface, we obtain (Table 3.1) σ = 34.3 pm and l = 2 nm. (As discussed below, we attribute the low value of l to residual AFM noise, rather than to physically meaningful features.) Taking the measured value of σ as a guide, the surface of mica is seen to be at least 5 times smoother than that of the SiO_2 substrate.
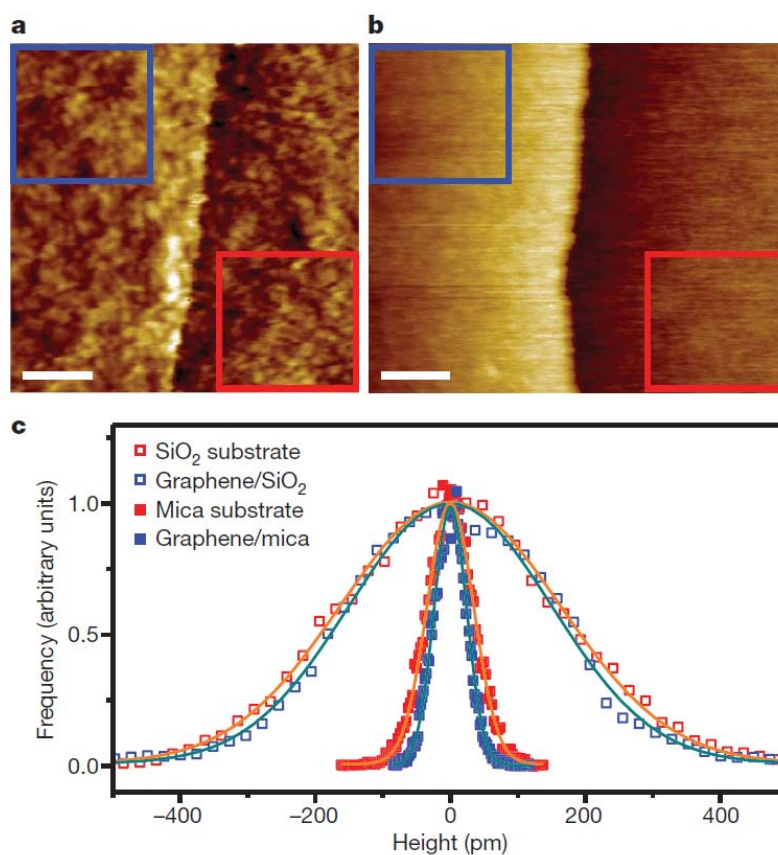
Figure 3.3 AFM topographic images of different samples and the corresponding histograms of height. **(a)** AFM image of a boundary between a graphene monolayer and a SiO_2 substrate. Graphene occupies the left hand side of the image and the scale bar is 100 nm in length. **(b)** As in (a) for a graphene monolayer on a mica substrate. **(c)** Height histograms for graphene on mica (solid blue squares), the mica substrate (solid red squares), graphene on SiO_2 (open blue squares), and the SiO_2 substrate (open red squares). The data, corresponding to the regions designated by the squares in the images of (a) and (b), are described by Gaussian distributions (solid lines) with standard deviations σ of 24.1 pm, 34.3 pm, 154 pm, and 168 pm, respectively.

When placed on such a flat mica terrace, graphene monolayers display an exceedingly flat structure, one quite different from that observed for graphene/SiO$_2$. This difference can be seen immediately by comparing the 3D presentation of the AFM topographic images in Figure 3.5(a, b). More quantitatively, for graphene on mica, we obtain σ = 24.1 pm and l = 2 nm. This topography is at least 5 times smoother than that of graphene on SiO$_2$. Since the interlayer distance in bulk graphite is 340 pm, with an observed height variation of only 24.1 pm, we can consider graphene on mica as having reached the limit of atomic flatness with respect to ripples, *i.e.,* a height variation far below the diameter of an atom when probed with our lateral resolution of 7 nm.
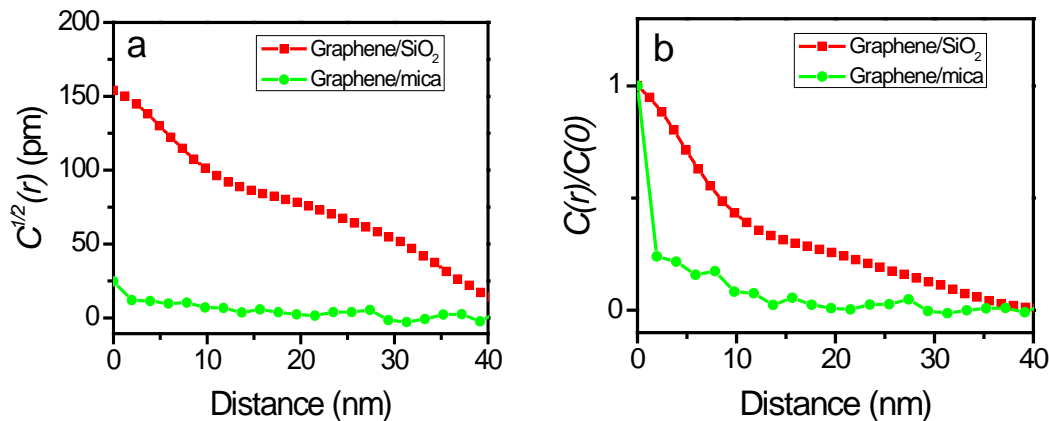
Figure 3.4 (a) Square root of the height correlation function [$C^{1/2}(r)$] for graphene/SiO$_2$ and graphene/mica. **(b)** Normalized height correlation function [$C(r)/C(0)$] for graphene/SiO$_2$ and graphene/mica.

Table 3.1 Summary of standard deviation (σ) of height distribution and correlation length (l) of the images for different surfaces

	SiO$_2$	Graphene/SiO$_2$	Mica	Graphene/mica	Graphite
σ (pm)	168	154	34.3	24.1	22.6
l (nm)	16	22	2	2	2
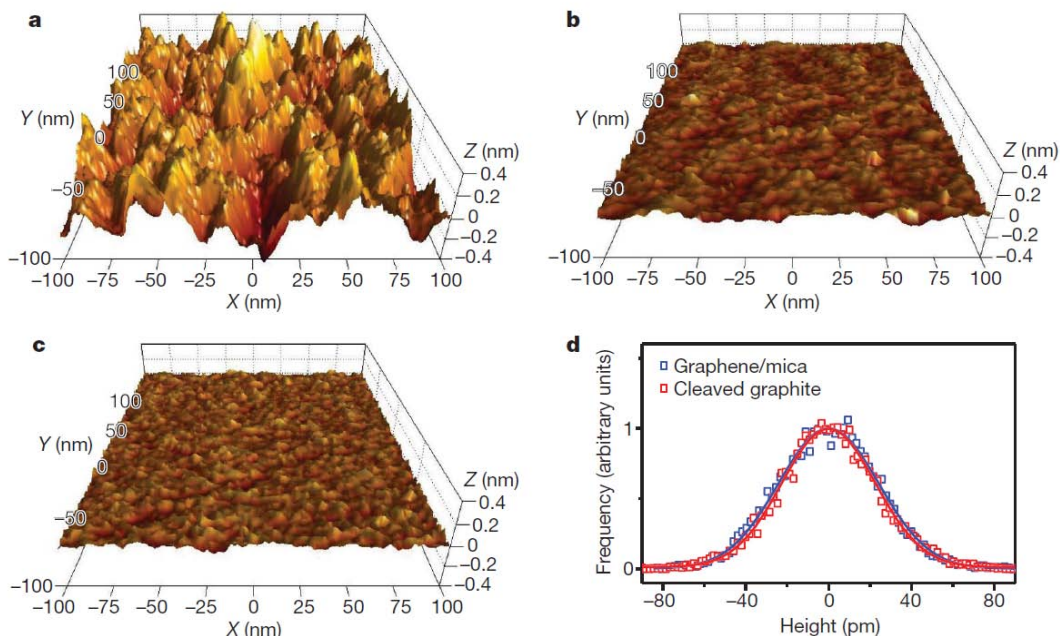
Figure 3.5 Comparison of surface roughness for graphene on SiO_2 and on mica, and for cleaved graphite. **(a, b)** 3-D representations of the AFM topographic data for graphene on SiO_2 (a), and on mica (b) substrates. The images correspond to the regions in Figure 3.3a, b designated by the blue squares. **(c)** AFM image of the surface of a cleaved kish graphite sample. Images a, b, c correspond to 200nm x 200nm areas and are presented with the same height scale. **(d)** Height histograms of the data in (b) as blue squares and in (c) as red squares. The histograms are described by Gaussian distributions (solid lines) with standard deviations σ of 24.1 pm and 22.6 pm, respectively.

We would like to make two observations about the topography of graphene monolayers on mica. First, although the graphene samples are very flat over areas on the sub-micron scale, variations in the topography can be seen when surveying the surface over distances of several microns. In particular, we have observed the presence of flat plateaus in the graphene topography, which rise abruptly by a height of ~0.4 nm above the lower regions. We attribute these elevated regions to the formation of islands of molecular adlayers on the mica surface under the graphene sample [29]. The presence of adsorbates may contribute to the observed slight local roughness. We find that σ varies from 20.8 to 24.1 pm for different regions of the graphene sample on mica. Second,

given the limit of our AFM lateral resolution (7 nm), we cannot exclude the existence of sub-nanometre corrugation features (*e.g*., atomic defects and vacancies) on the graphene surface. Based on modelling using the 7-nm AFM spatial resolution, the observed bound on the height variation of $\sigma < 25$ pm for graphene on mica allows us to exclude any periodic corrugations with a peak to trough separation greater than 5 nm (and an assumed amplitude of at least 100 pm). Further, isolated features of lateral extent greater than 1.5 nm (and a height of at least 100 pm) are also incompatible with our observed topography.

3.3.2 Comparison of Graphene on Mica and on Graphite Surface

The discussion of the flatness of the graphene/mica surface given above has been conservative in not attributing any of the observed height variation in the AFM images to instrumental noise. In fact, the results indicate that AFM noise is significant in measurements of flat surfaces. In particular, the correlation length of $l \sim 2$ nm calculated for the mica and the graphene/mica surfaces must arise largely from AFM noise, since any true physical features could only contribute to a correlation length comparable to or greater than the AFM spatial resolution of 7 nm. To address this issue, we made AFM measurements of the topography of cleaved kish graphite [Figure 3.5(c)]. The observed topography for the cleaved graphite surface is very similar to that of graphene/mica. Figure 3.5(d) compares the height histograms for graphite and graphene/mica. The widths of the distributions are, respectively, $\sigma = 22.6$ pm and $\sigma = 24.1$ pm. If we treat the graphite surface as entirely flat, then the measured standard deviation reflects the instrumental noise. Under the assumption that the instrumental noise adds in quadrature

to any true height fluctuations, the values given above constrain the actual roughness of the graphene/mica sample to < 8.5 pm.

3.3.3 AFM Images after Fourier Filtering

Beyond the direct comparative study of topography of graphene/mica and the cleaved graphite surface, we also consider briefly the use of Fourier filtering to eliminate noise from the AFM images. Given the measured AFM lateral spatial resolution of 7 nm, we may safely remove any apparent spatial variation in the AFM images below this length scale without altering the actual physical content of the data. We carry out this procedure by applying a low-pass filter to the two-dimensional Fourier transform of the AFM topographic images. For our analysis, we apply a 6th-order Butterworth low pass filter with a cut-off wavelength at 10 nm, which suppresses features in the images with a characteristic length scale below 5 nm. The suitability of this filtering procedure is confirmed by noting that it introduces only minimal broadening in the AFM image of the abrupt step at the graphene-mica edge. Using this low-pass filtering procedure for the graphite surface, we find that σ decreases significantly (from 22.6 pm to 12.4 pm). For graphene/SiO$_2$, on the other hand, σ drops only slightly (from 154 pm to 148 pm). This behavior is consistent with our expectation that AFM noise dominates on flat surfaces, but has relatively little effect for the more corrugated case of the SiO$_2$ substrate. For the sample of graphene/mica presented above, σ decreases from 24.1 pm to 16.1 pm. In some of the interior regions of the graphene/mica sample, σ is found after filtering to be as low as 11.4 pm.

3.3.4 Characterization of Tip-Sample Interactions

Finally, in assessing the flatness of graphene, possible perturbations in its topography from tip-sample interactions must also be considered. To exclude possible perturbations in topography of the graphene layer from tip-sample interactions, we scanned our samples repeatedly under different conditions. Free amplitudes of the AFM cantilever from 30 nm down to 4.5 nm and amplitude set points ranging from 40% to 90% of the free amplitude were examined. No significant changes in the topography of graphene on mica were observed under any of these conditions. In all measurements, the phase shift between the driving force and the cantilever response was larger than 90°, indicating that the AFM is operating in the regime where the average tip-sample force is attractive [30]. To treat these interactions in more detail, we examined the AFM tip motion on a graphite surface using the established VEDA simulation software [31]. We found that the tip-sample force remains attractive for the full period of cantilever vibration whenever the cantilever free amplitude is less than 8 nm and the amplitude set point lies in the range from 40% to 90% of the free amplitude. Therefore, our AFM measurements in the lower range of cantilever amplitudes were carried out strictly in the attractive regime, and the possibility of tip-sample interactions leading to an artificially smoothed topography can be excluded.

3.4 Conclusion

We have demonstrated the fabrication of graphene monolayers that are flat down to the atomic level. These samples are produced by deposition on the atomically flat terraces of cleaved mica surfaces. The apparent height variation in the graphene layers observed by

high-resolution AFM is less than 25 pm, indicating the suppression of any existing intrinsic ripples in graphene. Since the discovery of intrinsic ripples in free-standing graphene, there has been considerable discussion on the role of substrate corrugation in determining the morphology of supported graphene monolayers [4-9]. While the observed corrugation of supported graphene might well be an intrinsic feature [3,10] of the graphene monolayers in the experiments performed to date, a different explanation is equally possible. The roughness of the graphene surfaces may simply reflect the contours of the underlying substrates, which typically exhibit corrugation comparable to that observed in the supported graphene monolayers. Our measurements demonstrate unambiguously that intrinsic ripples in graphene, even if they exist, can be strongly suppressed by interfacial van der Waals interactions when this material is supported on an appropriate atomically flat substrate.

References

[1]   C. H. Lui, L. Liu, K. F. Mak, G. W. Flynn & T. F. Heinz. "Ultraflat graphene", *Nature* **462**, 339-341, (2009).

[2]   A. K. Geim & K. S. Novoselov. "The rise of graphene", *Nat. Mater.* **6**, 183, (2007).

[3]   J. C. Meyer, A. K. Geim, M. I. Katsnelson, K. S. Novoselov, T. J. Booth & S. Roth. "The structure of suspended graphene sheets", *Nature* **446**, 60-63, (2007).

[4]   E. Stolyarova, K. T. Rim, S. M. Ryu, J. Maultzsch, P. Kim, L. E. Brus, T. F. Heinz, M. S. Hybertsen & G. W. Flynn. "High-resolution scanning tunneling microscopy imaging of mesoscopic graphene sheets on an insulating surface", *Proc. Natl. Acad. Sci. U. S. A.* **104**, 9209-9212, (2007).

[5]   M. Ishigami, J. H. Chen, W. G. Cullen, M. S. Fuhrer & E. D. Williams. "Atomic structure of graphene on SiO$_2$", *Nano Lett.* **7**, 1643-1648, (2007).

[6]   T. J. Booth, P. Blake, R. R. Nair, D. Jiang, E. W. Hill, U. Bangert, A. Bleloch, M. Gass, K. S. Novoselov, M. I. Katsnelson & A. K. Geim. "Macroscopic graphene membranes and their extraordinary stiffness", *Nano Lett.* **8**, 2442-2446, (2008).

[7]   K. R. Knox, S. C. Wang, A. Morgante, D. Cvetko, A. Locatelli, T. O. Mentes, M. A. Nino, P. Kim & R. M. Osgood. "Spectromicroscopy of single and multilayer graphene supported by a weakly interacting substrate", *Phys. Rev. B* **78**, 201408, (2008).

[8]   U. Stoberl, U. Wurstbauer, W. Wegscheider, D. Weiss & J. Eroms. "Morphology and flexibility of graphene and few-layer graphene on various substrates", *Appl. Phys. Lett.* **93**, 051906, (2008).

[9]   V. Geringer, M. Liebmann, T. Echtermeyer, S. Runte, M. Schmidt, R. Ruckamp, M. C. Lemme & M. Morgenstern. "Intrinsic and extrinsic corrugation of monolayer graphene deposited on SiO2", *Phys. Rev. Lett.* **102**, 076102, (2009).

[10]   A. Fasolino, J. H. Los & M. I. Katsnelson. "Intrinsic ripples in graphene", *Nature Mater.* **6**, 858-861, (2007).

[11]   J. Martin, N. Akerman, G. Ulbricht, T. Lohmann, J. H. Smet, K. Von Klitzing & A. Yacoby. "Observation of electron-hole puddles in graphene using a scanning single-electron transistor", *Nature Phys.* **4**, 144-148, (2008).

[12]   A. Deshpande, W. Bao, F. Miao, C. N. Lau & B. J. LeRoy. "Spatially resolved spectroscopy of monolayer graphene on SiO$_2$", *Phys. Rev. B* **79**, 205411, (2009).

[13]   S. V. Morozov, K. S. Novoselov, M. I. Katsnelson, F. Schedin, L. A. Ponomarenko, D. Jiang & A. K. Geim. "Strong suppression of weak localization in graphene", *Phys. Rev. Lett.* **97**, 016801, (2006).

[14]   M. I. Katsnelson & A. K. Geim. "Electron scattering on microscopic corrugations in graphene", *Phil. Trans. R. Soc. A* **366**, 195-204, (2008).

[15]   L. Liu, S. M. Ryu, M. R. Tomasik, E. Stolyarova, N. Jung, M. S. Hybertsen, M. L. Steigerwald, L. E. Brus & G. W. Flynn. "Graphene oxidation: Thickness-dependent etching and strong chemical doping", *Nano Lett.* **8**, 1965-1970, (2008).

[16]   S. Ryu, M. Y. Han, J. Maultzsch, T. F. Heinz, P. Kim, M. L. Steigerwald & L. E. Brus. "Reversible Basal Plane Hydrogenation of Graphene", *Nano Lett.* **8**, 4597-4602, (2008).

[17]   D. C. Elias, R. R. Nair, T. M. G. Mohiuddin, S. V. Morozov, P. Blake, M. P. Halsall, A. C. Ferrari, D. W. Boukhvalov, M. I. Katsnelson, A. K. Geim & K. S. Novoselov. "Control of Graphene's Properties by Reversible Hydrogenation: Evidence for Graphane", *Science* **323**, 610-613, (2009).

[18]   D. Huertas-Hernando, F. Guinea & A. Brataas. "Spin-orbit coupling in curved graphene, fullerenes, nanotubes, and nanotube caps", *Phys. Rev. B* **74**, 155426, (2006).

[19]   F. de Juan, A. Cortijo & M. A. H. Vozmediano. "Charge inhomogeneities due to smooth ripples in graphene sheets", *Phys. Rev. B* **76**, 165409, (2007).

[20] L. Brey & J. J. Palacios. "Exchange-induced charge inhomogeneities in rippled neutral graphene", *Phys. Rev. B* **77**, 041403, (2008).

[21] F. Guinea, B. Horovitz & P. Le Doussal. "Gauge field induced by ripples in graphene", *Phys. Rev. B* **77**, 205421, (2008).

[22] F. Guinea, M. I. Katsnelson & M. A. H. Vozmediano. "Midgap states and charge inhomogeneities in corrugated graphene", *Phys. Rev. B* **77**, 075422, (2008).

[23] E. A. Kim & A. H. C. Neto. "Graphene as an electronic membrane", *Europhys. Lett.* **84**, 57007, (2008).

[24] M. A. H. Vozmediano, F. de Juan & A. Cortijo. "Gauge fields and curvature in graphene", *J. Phys.: Conf. Ser.* **129**, 012001, (2008).

[25] T. O. Wehling, A. V. Balatsky, A. M. Tsvelik, M. I. Katsnelson & A. I. Lichtenstein. "Midgap states in corrugated graphene: Ab initio calculations and effective field theory", *Europhys. Lett.* **84**, 17003, (2008).

[26] S. L. Bragg & G. F. Claringbull. *Crystal Structures of Minerals*. Vol. 4 (G. Bell and Sons, LTD, 1965).

[27] K. S. Novoselov, D. Jiang, F. Schedin, T. J. Booth, V. V. Khotkevich, S. V. Morozov & A. K. Geim. "Two-dimensional atomic crystals", *Proc. Natl. Acad. Sci. U. S. A.* **102**, 10451-10453, (2005).

[28] A. C. Ferrari, J. C. Meyer, V. Scardaci, C. Casiraghi, M. Lazzeri, F. Mauri, S. Piscanec, D. Jiang, K. S. Novoselov, S. Roth & A. K. Geim. "Raman spectrum of graphene and graphene layers", *Phys. Rev. Lett.* **97**, 187401, (2006).

[29] K. Xu, P. G. Cao & J. R. Heath. "Graphene Visualizes the First Water Adlayers on Mica at Ambient Conditions", *Science* **329**, 1188.

[30] R. Garcia & A. San Paulo. "Attractive and repulsive tip-sample interaction regimes in tapping-mode atomic force microscopy", *Phys. Rev. B* **60**, 4961-4967, (1999).

[31] J. Melcher, S. Q. Hu & A. Raman. "Invited Article: VEDA: A web-based virtual environment for dynamic atomic force microscopy", *Review of Scientific Instruments* **79**, 061301, (2008).

Chapter 4

Ultrafast Photoluminescence from Graphene

After addressing the issue of graphene's morphology in Chapter 3, I present our investigation of graphene's electronic and optical properties in this chapter. In particular, we study the dynamics of graphene's excited carriers by using their spontaneous light emission [1]. Since graphene has no band gap, photoluminescence is not expected from relaxed charge carriers. We have, however, observed significant light emission from graphene under excitation by ultrashort laser pulses. Light emission is found to occur across the visible spectral range, with emitted photon energies exceeding that of the excitation laser. The emission exhibits a nonlinear dependence on the laser fluence. In two-pulse correlation measurements, a dominant relaxation time of tens of femtoseconds is observed. These experimental observations can be accounted by a two-temperature model describing the electrons and their interaction with strongly coupled optical phonons (SCOP).

4.1 Introduction

The optical properties of graphene have attracted attention because of the insight they provide into the excited states of this remarkable material, and because of the potential that they offer for novel applications. Among the striking results is the absorbance of single-layer graphene of magnitude $\pi\alpha$, where α is the fine structure constant, in the near-infrared to visible spectral range [2,3]. The possibility of tuning this

absorption in the infrared by Pauli blocking has also been demonstrated [4,5]. Optical measurements with ultrafast excitation pulses have provided means of probing electron and phonon dynamics in graphene [6-16]. To date, however, all investigations have been confined to probing the *light absorption* in graphene. Aside from the weak inelastic scattering associated with vibrations through the Raman process, there have been no reports of *light emission* from graphene. The lack of observable emission can be readily understood from the absence of a band gap in graphene. Carriers can fully relax through rapid electron-electron and electron-phonon interactions before the relatively slow process of light emission is possible. Thus, photoluminescence has only been reported in chemically modified graphene [17-23], where the electronic structure has been modified and longer lived states may be present.

In this chapter, we investigate an unusual photoluminescence phenomenon in graphene [1]. Under excitation by ultrashort (30-fs) laser pulses, we observed significant light emission over a broad spectral range (1.7 - 3.5 eV) from pristine single-layer graphene. This light emission process differs from conventional hot luminescence: it has a nonlinear dependence on the pump excitation and also appears at photon energies well above that of the excitation laser. We have characterized this emission process by measurements of the emission spectra and their dependence on pump fluence. We have also performed two-pulse correlation measurements of the emission process, which reveal a dominant response on the time scale of 10's of femtoseconds. These observations can be understood in a model in which the electronic excitations are largely thermalized among themselves, but are only partially equilibrated with strongly coupled optical phonons (SCOPs) and essentially decoupled from the other lattice vibrations. The

femtosecond pump excitation can thus produce carriers with transient temperatures above 3000 K that give rise to readily observable emission in the visible range. In addition to revealing a new physical process in graphene, these measurements provide insight into carrier and phonon dynamics in graphene. The results indicate that electron-electron scattering under our experimental conditions is efficient on the 10-fs time scale, that coupling with the SCOPs is strong on a time scale below 100 fs, and that equilibration with other phonons occurs on a time scale approaching 1 ps.

4.2 Experiment

In our experiment, we investigated single-layer graphene samples exfoliated from kish graphite (Toshiba) and deposited on freshly cleaved mica substrates. Information about the sample preparation and characterization has been presented in chapter 2 and 3. The graphene samples were excited by ultrashort laser pulses with a photon energy of 1.5 eV from an 80-MHz modelocked Ti:sapphire oscillator. The pulse FWHM at the sample was 30 fs, as determined by a second-harmonic autocorrelation measurement. The spatial profile of the focused laser beam was characterized by scanning a sharp edge across the beam in the plane of the sample. The effective spot size was then determined by weighting this profile using the measured nonlinear fluence dependence of luminescence discussed below. The absorbed laser fluence F was measured directly under the experimental excitation conditions [3]. It includes a modest absorption saturation effect observed at high fluences [11]. We measured the light emission under excitation both by individual pulses and by pairs of pulses. For the latter case, we recorded the light emission as a function of the temporal separation between two equivalent excitation

pulses, which were orthogonally polarized to eliminate interference effects. The emission was collected in both transmission and reflection geometries and analyzed by a spectrometer coupled to a cooled charge-coupled device (CCD) array detector. The emission spectra were calibrated with a quartz tungsten halogen lamp. The emission strength is presented in terms of the spectral fluence $\mathcal{F}(\hbar\omega)$, i.e., total radiant energy emitted in all directions per unit area per unit photon energy as a function of the photon energy $\hbar\omega$. There is an estimated uncertainty of a factor of 10 in the absolute calibration of the emission strength. All measurements were performed under ambient conditions at room temperature. More details of the experimental techniques and apparatus can be found in Chapter 2.
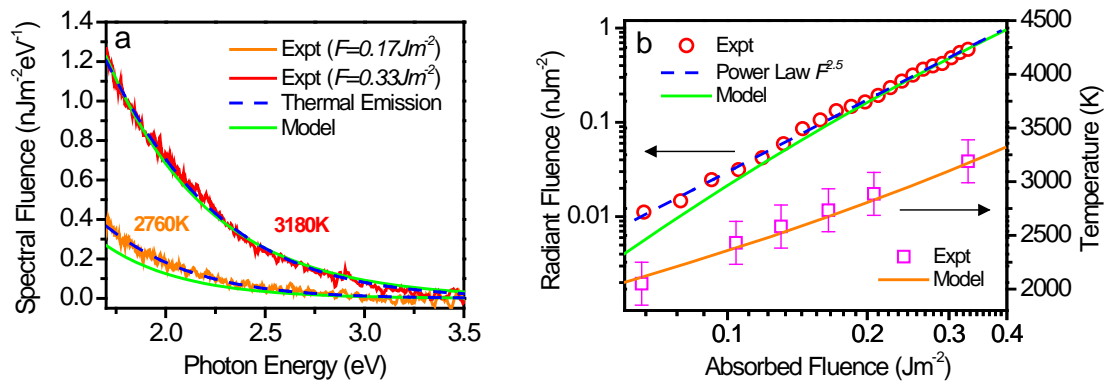
Figure 4.1 (a) Spectral fluence of light emission from graphene for excitation with 30-fs pulses of absorbed fluences of $F = 0.17$ and 0.33 Jm^{-2}. The spectra are compatible with the predictions for thermal emission (dashed blue lines), with $T_{em} = 2760$ K and 3180 K, respectively. A full calculation using the two-temperature model described in the text also gives a good agreement (solid green lines). The predicted emission fluence here and in (b) has been multiplied by a factor of ~ 0.2 to match the scale of the experimental data. **(b)** The behavior of graphene light emission as a function of absorbed laser fluence, presented on a log scale. The red circles display experimental values for the total radiant fluence for photons from 1.7 to 3.5 eV. The overall fluence dependence of data can be described phenomenologically by a power-law relation with an exponent of 2.5 (dashed blue line) and is consistent with predictions of the two-temperature model (solid green line). The magenta squares correspond to the experimental emission temperatures for different absorbed fluences, which also agree well with the prediction of the two-temperature model (orange solid line).

4.3 Light Emission by Single-Pulse Excitation

Under excitation by femtosecond laser pulses, the graphene samples produced readily observable light emission over the entire spectral range from the visible to near-ultraviolet (1.7 - 3.5 eV). The emission was unpolarized and angularly broad. Two emission spectra for different absorbed laser fluences are shown in Figure 4.1(a). Over the observed spectral range, the luminescence quantum efficiency was ~ 10^{-9}. In contrast, for continuous-wave excitation of the same photon energy (1.5 eV), we could not detect any graphene light emission over the indicated spectral range (quantum efficiency < 10^{-12}).

Another distinctive feature of the light emission process is its nonlinear dependence on the pump laser fluence. Figure 4.1(b) displays the integrated radiant fluence (red circles) over the observed spectral range (1.7 - 3.5 eV) as a function of the absorbed pump fluence. The emission varies with the absorbed fluence F as a power law of $F^{2.5}$ [dashed blue line]. For light emission in different spectral windows we find a power-law relation, but with different exponents: an exponent of 2 for photons near the lower end of our spectral range and of 3.5 for photons at its upper end.

The experimental observations above immediately preclude several mechanisms for the light emission process. The emission of photons at energies above that of the pump photons and the nonlinearity of the process imply that we are not observing a conventional hot-luminescence process. Similarly, hot luminescence driven by a two-photon absorption process can also be excluded by the strong variation of the emission spectrum with pump fluence. We see a steady decrease of light emission with increasing photon energy. This suggests comparison with the spectrum expected for thermal

emission. For a system at an effective emission temperature T_{em}, we obtain from Planck's law, a spectral radiant fluence (integrated over all angles and polarizations) of

$$\mathcal{F}\left(\hbar\omega, T_{em}\right) = \tau_{em}\varepsilon\left(\hbar\omega\right)\frac{\omega^3}{2\pi^2 c^2}\left[\exp\left(\frac{\hbar\omega}{kT_{em}}\right) - 1\right]^{-1}. \tag{4.1}$$

Here $\varepsilon(\hbar\omega)$ is the sample emissivity, which we determine directly from the measured absorption spectrum of graphene corrected for the influence of the mica substrate. Since we are describing the emitted energy, not the emitted power, the expression also contains a parameter τ_{em} to characterize the effective emission time for each laser excitation pulse.

This simple phenomenological description of the emission provides an excellent match to the experimental data [dashed blue curves in Figure 4.1(a)]. The inferred emission temperatures T_{em} for our measurements lie in the range of 2000 K to 3200 K and vary sublinearly with pump fluence [Figure 4.1(b)]. As for the absolute magnitude of the experimental radiant fluence, our data can be reproduced using Eq. 4.1) for τ_{em} in the range of 10 - 100 fs.

The analysis implies that carriers in graphene are well thermalized among themselves during the period of light emission. This finding suggests very rapid carrier-carrier scattering. The electrons and holes are initially created with a nearly monochromatic energy of 0.75 eV. During the period of light emission, which may occur on a time scale as short as that of the 30-fs excitation pulse, a largely thermalized energy distribution is apparently established for electrons and holes that contribute to the observed emission spectrum. This rapid thermalization is compatible with recent estimates of electron-electron scattering times [15,24,25]. For instance, for electron densities of $\sim 10^{12}$ cm^{-2}, the scattering times have been estimated to be tens of

femtoseconds [24,25]. Still shorter times would be expected under our experimental conditions with carrier excitation densities in the range of 10^{14} cm^{-2}.

The observed emission temperatures allow us to gain considerable insight into the emission mechanism. The emission temperature reflects the behavior of the electrons in the graphene, since they interact strongly with visible photons. Now if all absorbed laser energy were retained in the electronic system, the low electronic specific heat of graphene would lead to an electronic temperature of ~ 9000 K for the absorbed pump fluence of 0.33 Jm^{-2}. This is incompatible with the temperature of 3180 K extracted from the experimental emission spectrum. Therefore, even in this ultrafast light emission process, a significant fraction of the deposited energy must leave the electronic system. Since lateral diffusion of energy away from the excited region of the sample can be ruled out given the spatial dimensions and time scale, we conclude that efficient energy transfer to other degrees of freedom must occur. We note that in the limit of full equilibration of the excitation with *all* phonon degrees of freedom, *i.e.,* considering the full specific heat of graphene [26], we predict a temperature rise of only 380 K. Thus partial equilibration with the phonons must be considered.

The optical phonons in graphene serve as the most natural channel for energy relaxation from the excited electronic system, since electrons in graphene are strongly coupled to optical phonons near the Γ and K points in the Brillouin zone [13,27]. Investigations of phonon dynamics in graphite and carbon nanotubes by time-resolved Raman spectroscopy have directly demonstrated energy transfer from photoexcited electrons to these strongly coupled optical phonons (SCOPs) within 200 fs [28,29]. Various theoretical and experimental studies have also obtained ultrashort (< 100 fs)

emission times for optical phonons in graphene [24,30], graphite [14,16,31], and carbon

nanotubes [32,33].

4.4 Analysis by Two-Temperature Model

To analyze the results further, we introduce a model of excitations in the

electronic system and in the SCOPs, each characterized by its respective temperature, T_{el}

and T_{op}, and linked by the electron-phonon coupling:

$$\begin{cases} \dfrac{dT_{el}(t)}{dt} = \dfrac{I(t) - \Gamma\left(T_{el}, T_{op}\right)}{c_e\left(T_{el}\right)} \\[3mm] \dfrac{d_{op}(t)}{dt} = \dfrac{\Gamma\left(T_{el}, T_{op}\right)}{c_{op}\left(T_{op}\right)} - \dfrac{T_{op}(t) - T_0}{\tau_{op}}, \end{cases} \quad (4.2)$$

In this description, the graphene is excited by the absorbed irradiance $I(t)$, which initially

excites the electronic system. Energy then flows into the SCOPs at a rate described by

$\Gamma(T_{el}, T_{op})$. The specific heat of the electrons (per unit area) is denoted by c_{el}, while that

of the SCOPs is c_{op}. In addition to energy flow between the electrons and the SCOPs, we

have included a slower coupling of the SCOPs to other phonons in the system through

anharmonic decay. This channel for energy flow is described simply by a relaxation time

τ_{op}. We neglect the heating of these more numerous secondary phonons and assume that

they remain at the ambient temperature of $T_0 = 300$ K.

We model the temporal profile of the ultrafast excitation pulse using the form

$I(t) = \left(F / 2\tau_{exc}\right) \mathrm{sech}^2\left(t / \tau_{exc}\right)$, where F denotes the absorbed fluence and τ_{exc} the duration

of the exciting laser pulse. The pulse duration was determined by a second-harmonic

autocorrelation measurement and yielded a value of $\tau_{exc} = 19$ fs. The absorbed fluence

was established by measurement of the absorbed energy combined with a determination of the spatial profile of the beam.

For the electronic specific heat c_{el} (per unit area), we used the following analytical result derived from the linear dispersion of the graphene bands:

$$c_{el}\left(T_{el}\right) = \frac{18\zeta\left(3\right)}{\pi\left(\hbar\upsilon_F\right)^2}k^3 T_{el}^2 .$$

(4.3)

Here $\zeta(3) = 1.202$ is the zeta function, $\upsilon_F = 1.1 \times 10^6 ms^{-1}$ is the Fermi velocity of electrons in graphene, and k is the Boltzmann constant.

The electrons in graphene couple to only a small fraction of optical phonons in the Brillouin zone near the Γ and K points with particularly high efficiency; these are the strongly coupled optical phonons (SCOPs). The SCOPs scatter electrons from one part of the Dirac cone to another (Γ point phonons) or between the Dirac cones (K point phonons). In our model, we assumed that only these SCOPs are directly excited by the electrons through the electron-phonon interaction. The coupling of these SCOPs to other phonon modes is described by a phenomenological parameter, the lifetime of the SCOPs τ_{op}. In our analysis, we used $\tau_{op} = 1.5$ ps, based on the measured anharmonic decay rates in carbon nanotubes (1.1ps) [28] and graphite (2.2ps) [29]. Further, for simplicity, we neglected the (weak) dispersion in the phonon energy and considered all phonons to have the same energy of 200 meV as the Γ-point phonon.

The specific heat c_{op} (per unit area) of the SCOPs in graphene was determined from the time-resolved Raman studies of graphite [29]. These measurements yielded the population of the SCOPs (before any significant anharmonic decay occurred) as a function of the deposited laser excitation density per graphene layer. The SCOP

temperature extracted from the phonon population is found to increase sublinearly with the excitation power, *i.e.,* the specific heat increases nonlinearly with temperature. Figure 4.2 displays the plot of the absorbed fluence versus zone-center-phonon temperature in graphite. Fitting these data provides the following expression for the specific heat of the SCOPs as a function of T_{op} in the temperature range between 500 K and 2500 K:

$$c_{op}\left(T_{op}\right) = -4.79 \times 10^9 + 9.09 \times 10^6 T_{op} + 4453 T_{op}^2 + 1.29 T_{op}^3 \qquad (4.4)$$

(in units of eVcm^{-2}K^{-1}).
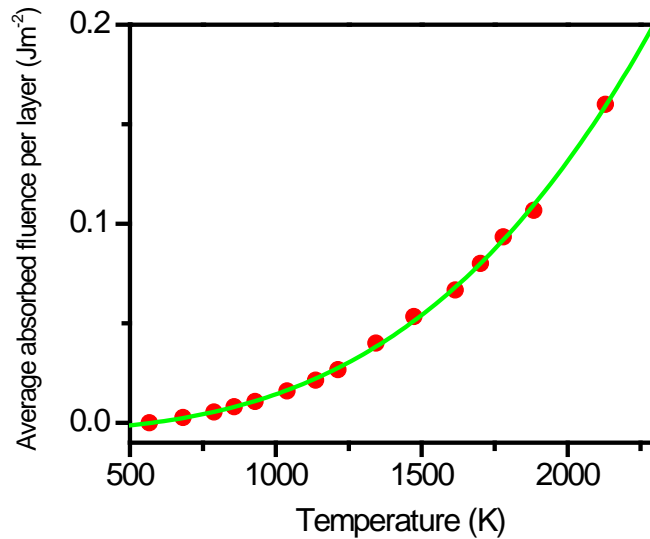
Figure 4.2 The plot of average absorbed fluence per graphene layer as a function of temperature of zone-center phonons in graphite. The red dots are experimental data and the green line is the fit by a cubic function.

We construct the electron-SCOP energy exchange rate $\Gamma(T_{el}, T_{op})$ using the available phase space for scattering of electrons near the K point of the Brillouin zone. The complete expression of $\Gamma(T_{el}, T_{op})$ includes both the emission of a phonon (the first term) and the absorption of a phonon (the second term):

$$\Gamma\left(T_{el},T_{op}\right)=\beta\left\{\left[1+n\left(T_{op}\right)\right]\int D\left(E\right)D\left(E-\hbar\Omega\right)f\left(E,T_{el}\right)\left[1-f\left(E-\hbar\Omega,T_{el}\right)\right]d\,E\right.$$
$$\left.-n\left(T_{op}\right)\int D\left(E\right)D\left(E+\hbar\Omega\right)f\left(E,T_{el}\right)\left[1-f\left(E+\hbar\Omega,T_{el}\right)\right]d\,E\right\}. \quad (4.5)$$

Here $D\left(E\right)=\left(2E/\pi\right)\left(\hbar\upsilon_{F}\right)^{2}$ is the density of states of electrons in graphene, including the spin and valley (*i.e.*, K and K' points) degeneracies. The term $n\left(T_{op}\right)=\left[\exp\left(\hbar\Omega/kT_{op}\right)-1\right]^{-1}$ represents the SCOP population at temperature T_{op}, and $f\left(E,T_{el}\right)=\left[\exp\left(E/kT_{el}\right)+1\right]^{-1}$ is the Fermi-Dirac distribution for electrons at electronic temperature T_{el}. In the later expression, we assume that the electrons and holes are in equilibrium with one another and have zero chemical potential. The only adjustable
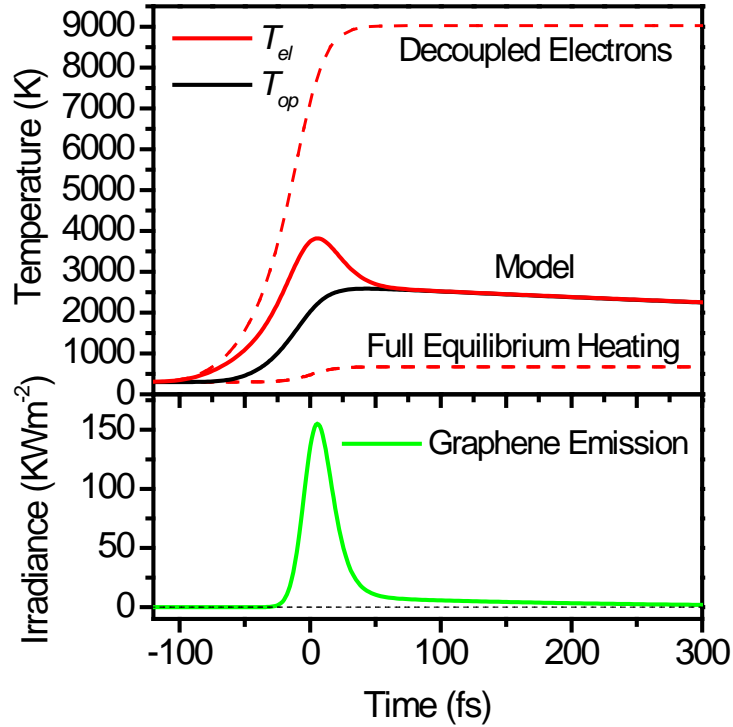
Figure 4.3 Simulations using the two-temperature model (described in the text) of the temporal evolution of the electronic temperature T_{el} (red line), the SCOPs temperature T_{op} (black line), and of the resulting graphene light emission (green line) for photon energies from 1.7 to 3.5 eV. The absorbed fluence F of the 30-fs pump pulse is 0.33 Jm^{-2}. For comparison, the upper panel also shows the calculated electronic temperatures for completely decoupled electrons and for full equilibrium of all degrees of freedom of the graphene sample (dashed red lines).

parameter in our model then is the proportionality constant β that represents the overall electron-phonon coupling strength. Throughout the analysis in this work, we have used the value of $\beta = 5 \text{ eV}^2\text{cm}^2\text{s}^{-1}$ that represents the best fit to all the data.

We note that in our model, we neglected decay channels for the electronic excitation involving the substrate. Electron scattering by substrate phonons has been invoked to explain transport data in graphene [34]. However, under excitation by high intensity ultrafast laser excitation, similar behavior for light emission was observed for graphene on different (silicon dioxide and mica) substrates, as well as from bulk graphite. This suggests that substrate coupling plays a secondary role in the relevant material response for our measurements.

Figure 4.3 displays the predicted temporal evolution for the temperatures of electrons (T_{el}) and SCOPs (T_{op}), as well as the corresponding light emission from graphene, for our experimental conditions. For comparison, we also show the electronic temperatures for the completely decoupled electronic system and for full thermal equilibrium of the graphene sample. These limits are, as discussed above, clearly incompatible with the experimental results. Within the two-temperature model, rapid energy transfer from electrons to SCOPs occurs during the laser excitation process. This results in a significant decrease in the electronic temperature compared to the case of uncoupled electrons (from a peak of ~9000 K to ~3800 K for $F = 0.33 \text{ Jm}^{-2}$). Equilibration with the SCOPs is almost complete within 50 fs, with the electronic system having lost over 95% of its energy to the SCOPs. Using the temporal evolution of T_{el}, we can calculate the expected integrated graphene emission from Eq. (4.1). We find a good agreement with experiment for the predicted spectral shape, effective emission

temperature T_{em} and emission strength [lines in Figure 4.1(a) and (b)]. We note that T_{em} approximates the peak value of the electronic temperature because of the strongly nonlinear dependence of the emission on the electron temperature [28]. The sublinear increase of T_{em} with absorbed fluence, which reflects the corresponding sublinear growth of the peak electronic temperature, arises from the quadratic temperature dependence of the electronic specific heat, as well as of the strong dependence of the electron-phonon coupling on the electronic temperature.

4.5 Role of Time Integration on the Form of Emission Spectra

In the experimental measurements, the recorded spectra for light emission from graphene were integrated over time. Within our description of the emission process, these time-integrated spectra thus correspond to light emission occurring at differing electronic temperatures of the excited graphene. However, over the observed spectral range [Figure 4.1(a)], the experimental data are found to be described quite well by thermal emission spectra at a single effective temperature. Here we discuss the origin of this behavior. The essential factor is that we are probing only the high-energy tail of the emission spectrum, which increases strongly with increasing temperature. This causes the integrated emission spectrum to weight predominantly the behavior near the peak temperature.

To examine this behavior in more detail, we consider the predicted emission for the temporal evolution of the electronic temperature $T_{el}(t)$ in Figure 4.3, as derived from the two-temperature model for our experimental parameters. We present this result over a longer time range in Figure 4.4(a). We see that T_{el} reaches the peak value of 3800 K and drops to 2700 K within 50 fs. This rapid response corresponds to the electronic

system remaining out of equilibrium with the SCOPs. Once equilibrium is established between these two subsystems, the temperature falls below 1000 K on the time scale of a few picoseconds. Using the expression for thermal emission from graphene (Eq. 4.1), we calculated the expected spectra for photon energies in the range of 1.75 - 3.5 eV integrated for different time intervals, as shown in Figure 4.4(b). We find that the emission for this range of photon energies arises primarily from emission near the peak electronic temperature. As can be seen in the figure, emission occurring after 50 fs changes the spectrum only modestly. Further, for times greater than 400 fs, hardly any emission is expected for the given spectral range. Since the range of temperatures for which strong emission occurs is relatively limited, we anticipate that a fit of the integrated spectrum to that of an effective emission temperature (by Eq. 4.1) will work rather well. This is shown to be the case in Figure 4.4(b), which yields effective temperatures of 3550 K and 3150 K, respectively, for the spectra obtained for emission over 50 fs and 10 ps intervals.
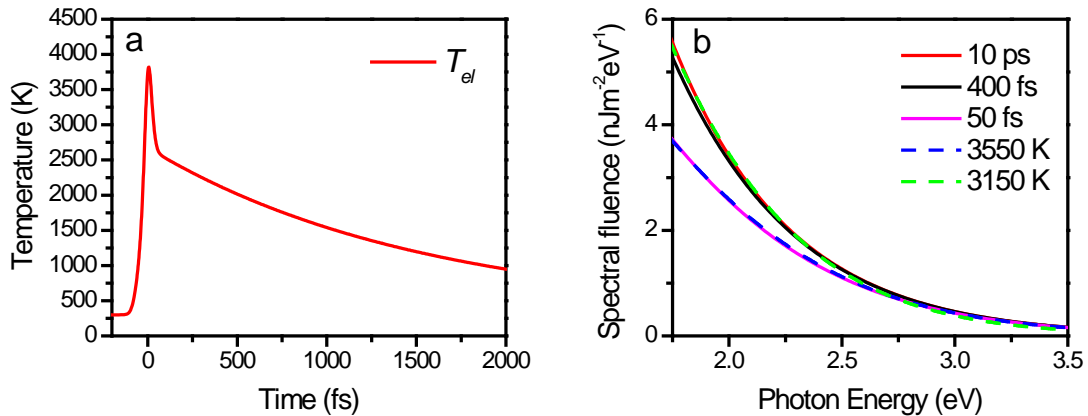
Figure 4.4 (a) The temporal evolution of the electronic temperature $T_{el}(t)$ obtained from the two-temperature model for our experimental parameters as described in the text. **(b)** Integrated emission spectra calculated for the electronic temperature profile $T_{el}(t)$ of (a) over times from -100 fs to 50 fs, 400 fs, and 10 ps. The integrated spectra at 50 fs and 10 ps are described well by thermal emission spectra, respectively, at constant effective temperatures of 3550 K and 3150 K, as shown.

4.6 Two-Pulse Correlation Measurement
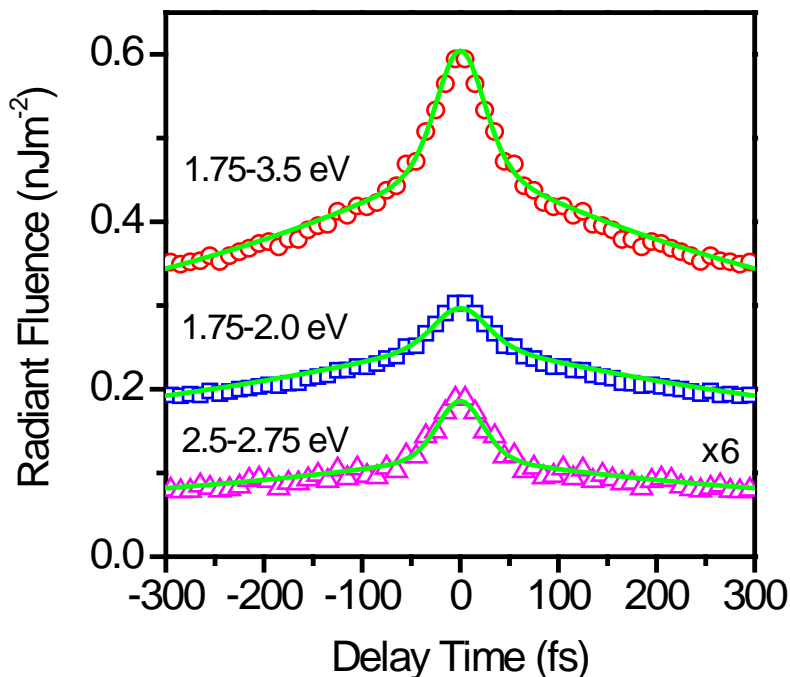
Figure 4.5 Total radiant fluence emitted by graphene over photon energies of 1.7-3.5 eV (red circles), 1.7-2.0 eV (blue squares) and 2.5-2.75 eV (magenta triangles) as a function of temporal separation between two identical laser excitation pulses. The absorbed fluence F of each pulse is 0.17 Jm^{-2}. The data for positive and negative delays were averaged to increase the signal-to-noise ratio. The data of 2.5-2.75 eV has been multiplied by a factor of 6 for clarity. The symbols are experimental data; the green lines are the predictions of the two-temperature model, multiplied by a factor of ~ 0.2 to match the magnitude of the experimental data.

To probe the dynamics of the light emission process more directly, we performed two-pulse correlation measurements in which the total radiant fluence (over photon energies in the range of 1.7 - 3.5 eV) was measured as a function of the temporal separation between a pair of laser excitation pulses. This approach has previously been applied to investigate nonequilibrium dynamics in metals by the detection of emitted electrons [35] and desorbed molecules [36]. Figure 4.5 shows the resulting correlation

trace (red circles) for an absorbed fluence of $F = 0.17$ Jm^{-2}. A dominant response on the time scale of 10's fs is observed, with a weaker, slower decay extending over 100's fs. The form of the correlation trace, with its dominant short response time, is seen under all conditions. The details, however, vary with the spectral range of the detected photons, as well as with the pump fluence. If we restrict detection to the high-energy photons (blue squares in Figure 4.5), we observe a shorter response time than that obtained by detecting only the low-energy photons (magenta triangles in Figure 4.5). This effect can be understood as a consequence of the dependence of the emission strength on the electronic temperature for different photon energies, *i.e.,* the relation is more nonlinear for higher photon energies than for lower photon energies.

We have applied the two-temperature model presented above to analyze the two-pulse correlation data. The underlying origin of the correlation feature can be understood from the calculation of the electronic temperature under two-pulse excitation (Figure 4.6). When the two pulses are sufficiently close to one another, the peak electronic temperature achieved by the second pulse exceeds that from one pulse alone. Since the light emission process is strongly nonlinear in temperature, we then observe a greater signal than for the two fully separated pulses. The enhancement is strongest at very short pulse separations, where electrons remain partially out of equilibrium with the SCOPs. A weaker enhancement of the emission persists during the slower decay of the subsystems of equilibrated electrons and SCOPs. Carrying out full calculation within the model yields good agreement with the measured two-pulse correlation function in all three spectral ranges (green lines in Figure 4.5).
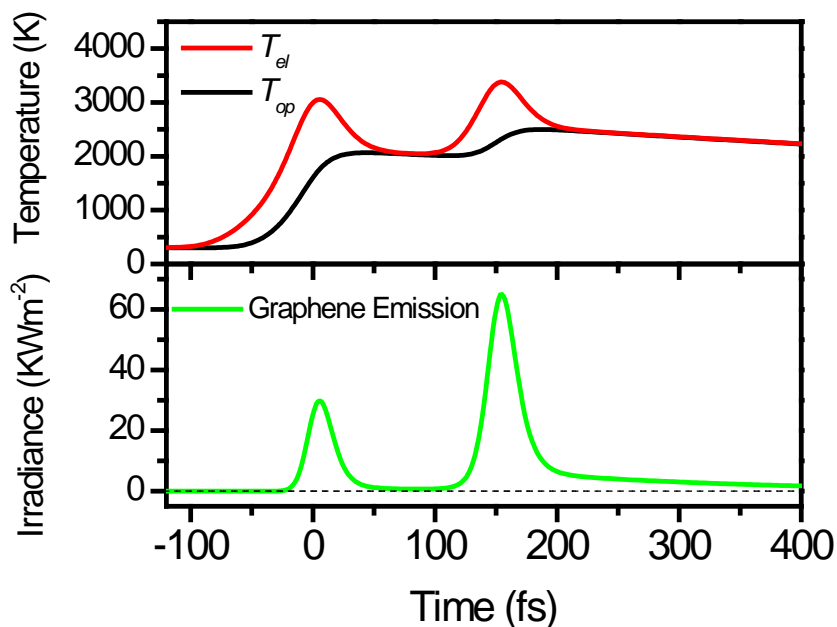
Figure 4.6 Simulations as in Figure 4.3, but with excitation by a pair of laser pulses, each yielding an absorbed fluence of $F = 0.17$ Jm^{-2} and separated in time by 150 fs.

4.7 Conclusion

In conclusion, the observed spectrally broad light emission from graphene can be understood as a direct consequence of a transient regime in which the electron distribution is driven strongly out of equilibrium with the phonons by ultrafast laser excitation. The existence of such energetic electron distributions has been reported in many different condensed-matter systems. Our work suggests that light emission may also be observable from such hot electrons in these materials. Characterization of spectra and dynamics of light emission would then provide a new and valuable window to probing electron dynamics.

References

[1]   C. H. Lui, K. F. Mak, J. Shan & T. F. Heinz. "Ultrafast Photoluminescence from Graphene", *Phys. Rev. Lett.* **105**, 4, (2010).

[2]   R. R. Nair, P. Blake, A. N. Grigorenko, K. S. Novoselov, T. J. Booth, T. Stauber, N. M. R. Peres & A. K. Geim. "Fine structure constant defines visual transparency of graphene", *Science* **320**, 1308-1308, (2008).

[3]   K. F. Mak, M. Y. Sfeir, Y. Wu, C. H. Lui, J. A. Misewich & T. F. Heinz. "Measurement of the Optical Conductivity of Graphene", *Phys. Rev. Lett.* **101**, 196405, (2008).

[4]   F. Wang, Y. B. Zhang, C. S. Tian, C. Girit, A. Zettl, M. Crommie & Y. R. Shen. "Gate-variable optical transitions in graphene", *Science* **320**, 206-209, (2008).

[5]   Z. Q. Li, E. A. Henriksen, Z. Jiang, Z. Hao, M. C. Martin, P. Kim, H. L. Stormer & D. N. Basov. "Dirac charge dynamics in graphene by infrared spectroscopy", *Nat. Phys.* **4**, 532-535, (2008).

[6]   D. Sun, Z. K. Wu, C. Divin, X. B. Li, C. Berger, W. A. de Heer, P. N. First & T. B. Norris. "Ultrafast Relaxation of Excited Dirac Fermions in Epitaxial Graphene Using Optical Differential Transmission Spectroscopy", *Phys. Rev. Lett.* **101**, 157402, (2008).

[7]   H. N. Wang, J. H. Strait, P. A. George, S. Shivaraman, V. B. Shields, M. Chandrashekhar, J. Hwang, F. Rana, M. G. Spencer, C. S. Ruiz-Vargas & J. Park. "Ultrafast relaxation dynamics of hot optical phonons in graphene", *Appl. Phys. Lett.* **96**, 081917, (2010).

[8]   J. M. Dawlaty, S. Shivaraman, M. Chandrashekhar, F. Rana & M. G. Spencer. "Measurement of ultrafast carrier dynamics in epitaxial graphene", *Appl. Phys. Lett.* **92**, 042116, (2008).

[9]   R. W. Newson, J. Dean, B. Schmidt & H. M. van Driel. "Ultrafast carrier kinetics in exfoliated graphene and thin graphite films", *Optics Express* **17**, 2326-2333, (2009).

[10]   P. A. George, J. Strait, J. Dawlaty, S. Shivaraman, M. Chandrashekhar, F. Rana & M. G. Spencer. "Ultrafast Optical-Pump Terahertz-Probe Spectroscopy of the Carrier Relaxation and Recombination Dynamics in Epitaxial Graphene", *Nano Lett.* **8**, 4248-4251, (2008).

[11]   S. Kumar, M. Anija, N. Kamaraju, K. S. Vasu, K. S. Subrahmanyam, A. K. Sood & C. N. R. Rao. "Femtosecond carrier dynamics and saturable absorption in graphene suspensions", *Appl. Phys. Lett.* **95**, 191911, (2009).

[12]   K. Seibert, G. C. Cho, W. Kutt, H. Kurz, D. H. Reitze, J. I. Dadap, H. Ahn, M. C. Downer & A. M. Malvezzi. "Femtosecond carrier dynamics in graphite", *Phys. Rev. B* **42**, 2842-2851, (1990).

[13]   T. Kampfrath, L. Perfetti, F. Schapper, C. Frischkorn & M. Wolf. "Strongly coupled optical phonons in the ultrafast dynamics of the electronic energy and current relaxation in graphite", *Phys. Rev. Lett.* **95**, 187403, (2005).

[14]   M. Breusing, C. Ropers & T. Elsaesser. "Ultrafast Carrier Dynamics in Graphite", *Phys. Rev. Lett.* **102**, 086809, (2009).

[15]   G. Moos, C. Gahl, R. Fasel, M. Wolf & T. Hertel. "Anisotropy of quasiparticle lifetimes and the role of disorder in graphite from ultrafast time-resolved photoemission spectroscopy", *Phys. Rev. Lett.* **87**, 267402, (2001).

[16]   K. Ishioka, M. Hase, M. Kitajima, L. Wirtz, A. Rubio & H. Petek. "Ultrafast electron-phonon decoupling in graphite", *Phys. Rev. B* **77**, 121402, (2008).

[17]   Z. T. Luo, P. M. Vora, E. J. Mele, A. T. C. Johnson & J. M. Kikkawa. "Photoluminescence and band gap modulation in graphene oxide", *Appl. Phys. Lett.* **94**, 111909, (2009).

[18]   T. Gokus, R. R. Nair, A. Bonetti, M. Bohmler, A. Lombardo, K. S. Novoselov, A. K. Geim, A. C. Ferrari & A. Hartschuh. "Making Graphene Luminescent by Oxygen Plasma Treatment", *ACS Nano* **3**, 3963-3968, (2009).

[19]   X. M. Sun, Z. Liu, K. Welsher, J. T. Robinson, A. Goodwin, S. Zaric & H. J. Dai. "Nano-Graphene Oxide for Cellular Imaging and Drug Delivery", *Nano Research* **1**, 203-212, (2008).

[20]   G. Eda, Y.-Y. Lin, C. Mattevi, H. Yamaguchi, H.-A. Chen, I.-S. Chen, C.-W. Chen & M. Chhowalla. "Blue Photoluminescence from Chemically Derived Graphene Oxide", *Advanced Materials* **22**, 505-509, (2010).

[21]   T. V. Cuong, V. H. Pham, Q. T. Tran, J. S. Chung, E. W. Shin, J. S. Kim & E. J. Kim. "Optoelectronic properties of graphene thin films prepared by thermal reduction of graphene oxide", *Mater. Lett.* **64**, 765-767, (2010).

[22]   T. V. Cuong, V. H. Pham, Q. T. Tran, S. H. Hahn, J. S. Chung, E. W. Shin & E. J. Kim. "Photoluminescence and Raman studies of graphene thin films prepared by reduction of graphene oxide", *Mater. Lett.* **64**, 399-401, (2010).

[23]   B. Wang, J. R. Sparks, H. R. Gutierrez, F. Okino, Q. Z. Hao, Y. J. Tang, V. H. Crespi, J. O. Sofo & J. Zhu. "Photoluminescence from nanocrystalline graphite monofluoride", *Appl. Phys. Lett.* **97**, 141915, (2010).

[24]   W. K. Tse, E. H. Hwang & D. S. Sarma. "Ballistic hot electron transport in graphene", *Appl. Phys. Lett.* **93**, 023128, (2008).

[25]   E. H. Hwang, B. Y. K. Hu & S. Das Sarma. "Inelastic carrier lifetime in graphene", *Phys. Rev. B* **76**, 115434, (2007).

[26]   T. Nihira & T. Iwata. "Temperature dependence of lattice vibrations and analysis of the specific heat of graphite", *Phys. Rev. B* **68**, 134305, (2003).

[27]   S. Piscanec, M. Lazzeri, F. Mauri, A. C. Ferrari & J. Robertson. "Kohn anomalies and electron-phonon interactions in graphite", *Phys. Rev. Lett.* **93**, 185503, (2004).

[28]   D. H. Song, F. Wang, G. Dukovic, M. Zheng, E. D. Semke, L. E. Brus & T. F. Heinz. "Direct measurement of the lifetime of optical phonons in single-walled carbon nanotubes", *Phys. Rev. Lett.* **100**, 225503, (2008).

[29]   H. G. Yan, D. H. Song, K. F. Mak, I. Chatzakis, J. Maultzsch & T. F. Heinz. "Time-resolved Raman spectroscopy of optical phonons in graphite: Phonon anharmonic coupling and anomalous stiffening", *Phys. Rev. B* **80**, 121403, (2009).

[30]   S. Butscher, F. Milde, M. Hirtschulz, E. Malic & A. Knorr. "Hot electron relaxation and phonon dynamics in graphene", *Appl. Phys. Lett.* **91**, 203103, (2007).

[31]   J. Jiang, R. Saito, A. Gruneis, G. Dresselhaus & M. S. Dresselhaus. "Electron-phonon interaction and relaxation time in graphite", *Chemical Physics Letters* **392**, 383-389, (2004).

[32]   A. Javey, J. Guo, M. Paulsson, Q. Wang, D. Mann, M. Lundstrom & H. J. Dai. "High-field quasiballistic transport in short carbon nanotubes", *Phys. Rev. Lett.* **92**, 106804, (2004).

[33]   J. Y. Park, S. Rosenblatt, Y. Yaish, V. Sazonova, H. Ustunel, S. Braig, T. A. Arias, P. W. Brouwer & P. L. McEuen. "Electron-phonon scattering in metallic single-walled carbon nanotubes", *Nano Lett.* **4**, 517-520, (2004).

[34]   J.-H. Chen, C. Jang, S. Xiao, M. Ishigami & M. S. Fuhrer. "Intrinsic and extrinsic performance limits of graphene devices on SiO2", *Nat Nano* **3**, 206-209, (2008).

[35]   X. Y. Wang, D. M. Riffe, Y. S. Lee & M. C. Downer. "Time-resolved electron-temperature measurement in a highly excited gold target using femtosecond thermionic emission", *Phys. Rev. B* **50**, 8016-8019, (1994).

[36]   F. Budde, T. F. Heinz, M. M. T. Loy, J. A. Misewich, F. Derougemont & H. Zacharias. "Femtosecond time-resolved measurement of desorption", *Phys. Rev. Lett.* **66**, 3024-3027, (1991).

Chapter 5

Imaging Stacking Order in Few-Layer Graphene

The previous two chapters have been devoted mainly to investigation of single-layer graphene (SLG). In our experiments, we find that adding extra graphene layers on SLG can bring forth new interesting properties to the material. The rest of the thesis will be devoted to investigation of Few-layer graphene (FLG). FLG has been predicted to exist in various crystallographic stacking sequences, which can strongly influence the material's electronic properties. In this chapter, I present an accurate and efficient method to characterize stacking order in FLG using the distinctive features of the Raman 2D-mode [1]. Raman imaging allows us to visualize directly the spatial distribution of Bernal (ABA) and rhombohedral (ABC) stacking in tri- and tetra-layer graphene. We find that 15% of exfoliated graphene tri- and tetra-layers is comprised of micrometer-sized domains of rhombohedral stacking, rather than of usual Bernal stacking. These domains are stable and remain unchanged for temperatures exceeding 800 ºC.

5.1 Introduction

Graphene-based materials have stimulated intense interest because of their remarkable electronic properties and potential for novel applications. With the impressive progress in research on graphene mono- and bi-layers, recent attention has also turned to graphene's few-layer counterparts [2-8]. In few-layer graphene (FLG), the crystallographic stacking of the individual graphene sheets provides an additional degree

of freedom [5,9-12]. The distinct lattice symmetries associated with different stacking orders of FLG have been predicted to strongly influence the electronic properties of FLG [4,5,9-24], including the band structure [9,11,13-20], interlayer screening [21], magnetic state [23,24], and spin-orbit coupling [22]. Experimentally, the strong influence of stacking order on the low-energy electronic structure of FLG was recently demonstrated by infrared (IR) spectroscopy [5]. For graphene trilayers, two stable crystallographic configurations are predicted: ABA and ABC stacking order [9-11,13,14] (Figure 5.1). In the absence of direct evidence of ABC stacking order in trilayers, ABA stacking order has generally been presumed in most studies of exfoliated materials, as this structure is believed to be slightly more stable thermodymically than the ABC stacking order. Recent studies [4,9-11,13,15,17,18,20,21,25], indicate, however, distinct properties for these two types of graphene trilayers. ABA trilayers are semi-metals with an electrically tunable band overlap [4,11,13,17-19], while ABC trilayers are predicted to be semiconductors with an electrically tunable band gap [11,13,16,20]. In view of these differences, research on FLG requires the development of convenient and accurate methods for characterizing stacking order and its spatial distribution.

While IR spectroscopy provides a means of identifying stacking order in FLG [5], it requires somewhat specialized instrumentation and cannot provide high spatial resolution. Raman spectroscopy, on the other hand, has the potential to overcome these limitations and serves as an effective general approach for characterization and spatial imaging of stacking order. The technique has already proved to be a reliable and efficient method for determining many physical properties of graphene layers [7,26]. The intensity of D-mode indicates the defect density [26]; the peak position and lineshape of G-mode

reflect the doping [26,27] and strain level [28,29]. In addition, the 2D (G') mode, arising from a double-resonant electronic process [7,26,30,31], is sensitive not only to the vibrational features of graphene, but also to its electronic structure. As such, its lineshape provides an accurate signature of graphene mono- and bi-layers [7,26,32,33].

In this chapter, we demonstrate that stacking order in tri- and tetra-layer graphene samples can be readily identified by means of Raman spectroscopy [1]. We find that both Bernal (ABA) and rhombohedral (ABC) stacking order are present in exfoliated samples and the different structures are associated with distinctive lineshapes in the Raman 2D mode. The rhombohedral samples show a more asymmetric 2D feature with an enhanced peak and shoulder, compared with the feature seen in Bernal samples. Taking advantage of this difference in lineshape, we were able to visualize stacking domains in exfoliated tri- and tetra-layer graphene with micrometer spatial resolution. Even in samples of completely homogeneous layer thickness, we observed domains of different stacking order, with approximately 15% of the total area displaying rhombohedral stacking.
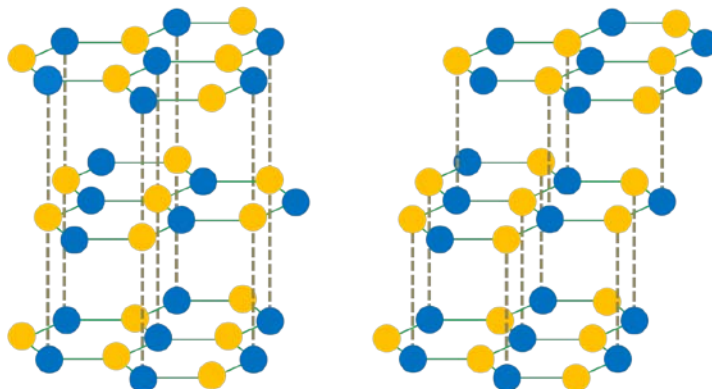
Figure 5.1 Lattice structure of trilayer graphene with ABA (left) and ABC (right) stacking sequence. The yellow and blue dots represent carbon atoms in the A and B sub-lattices of the graphene honeycomb structure.

5.2 Experiment

In our experiment, we prepared FLG samples by mechanical exfoliation of kish graphite (Toshiba) on both bulk SiO_2 (Chemglass, Inc) and Si substrates covered with a 300-nm-thick oxide layer. The substrates were cleaned by etching in piranha (sulfuric acid and hydrogen peroxide) solution. The typical area of our graphene samples varied from several hundreds to thousands of μm^2. We first examined the samples by IR spectroscopy. This technique permits accurate determination of layer thickness in FLG and, through the differences in the low-energy electronic structure, also of the stacking order [5]. We observed two distinct groups of IR spectra both for the trilayer and tetralayer graphene, corresponding to Bernal (ABA) and rhombohedral (ABC) stacking. We then performed Raman measurement on the same FLG samples. Raman spectra were collected in a backscattering geometry using linearly polarized laser radiation at wavelengths (photon energies) of 633 nm (1.96 eV), 597 nm (2.09 eV), 514 nm (2.41 eV), and 458 nm (2.71 eV). The laser beam was focused to a spot size of ~1 μm on the graphene samples. We obtained Raman spatial maps for an excitation wavelength of 514 nm by raster scanning with a precision two-dimensional stage having a step size of 0.5 μm or 1 μm[34]. For such spatial mapping of the Raman response, we generally used a spectral resolution of ~8 cm^{-1} (obtained with a 600 grooves/mm grating). For the measurement of key spectra, however, a spectral resolution of ~2 cm^{-1} (1800 grooves/mm grating) was chosen to elucidate the details of the lineshape.

5.3 Identifying Stacking Order by Infrared Spectroscopy

In our experiment, the exfoliated FLG samples on bulk SiO_2 (quartz) and Si/SiO_2 substrates were first examined by IR spectroscopy. The measurements were performed in both reflection and transmission geometry using a micro-Fourier Transform Infrared spectrometer with a globar source and a HgCdTe detector. As the intrinsic IR response of FLG on bulk SiO_2 and Si/SiO_2 substrates is the same, here we only present results for the bulk SiO_2 substrate since the analysis of the optical measurements is simpler. To determine the optical sheet conductivity σ of the FLG samples as a function of photon energy $\hbar\omega$, we follow the same method as our previous work in monolayer [35] and tetralayer [5] graphene. We recorded the reflectance spectra of both the FLG films on the quartz substrate (R_{FLG}) and of the bare substrate (R_{sub}). We obtain the optical conductivity $\sigma(\hbar\omega)$ directly from the fractional change of the reflectance as

$$\delta_R = \frac{R_{FLG} - R_{sub}}{R_{sub}} = \frac{4}{n_{sub}^2 - 1}\frac{4\pi}{c}\sigma .$$

(5.1)

Here c denotes the speed of light in vacuum and n_{sub} is the frequency-dependent refractive index of the quartz substrate. The IR optical conductivity provides an effective probe to the electronic structure of FLG. While the low-energy (< 0.7 eV) conductivity reflects the details of electronic structure and doping level, the high-energy (> 0.7 eV) part provides a precise identification of layer thickness. For photon energies well above the interlayer coupling (~ 0.4 eV), FLG graphene behaves much like independent graphene monolayers and its optical conductivity is nearly independent of the stacking sequence. Since graphene monolayer has an optical conductivity of $\pi e^2/2h$ in this spectral

range, we can identify the trilayer graphene by the expected conductivity value of $3 \times \pi e^2/2h$. Taking this as guidance, we found in total 45 trilayer graphene samples.

We observed two distinctive groups of IR response in the optical conductivity spectra of trilayer graphene, as shown in Figure 5.2 (a). The first kind of spectrum (green line) shows an absorption peak at 0.53 eV, which matches the result of ABA trilayer graphene [3]. The second kind of spectrum (red line) exhibits two narrow peaks at 0.33 and 0.39 eV. This distinct IR response spectrum of trilayer graphene, which is found in ~ 10% of our samples, has not been reported previously. It indicates the presence of a low-energy electronic structure different from that of ABA trilayer graphene. In addition, we have also observed IR spectra with both the features of the previous two kinds of spectra. This third type of spectrum, found in ~30% of our trilayer samples, can be described as a linear combination of the first two kinds of spectra [Figure 5.2 (b)].

These observations immediately lead to the consideration of the different crystallographic stacking sequences in trilayer graphene. The possible low-energy arrangements of adjacent layers of graphene are obtained by displacement of one layer
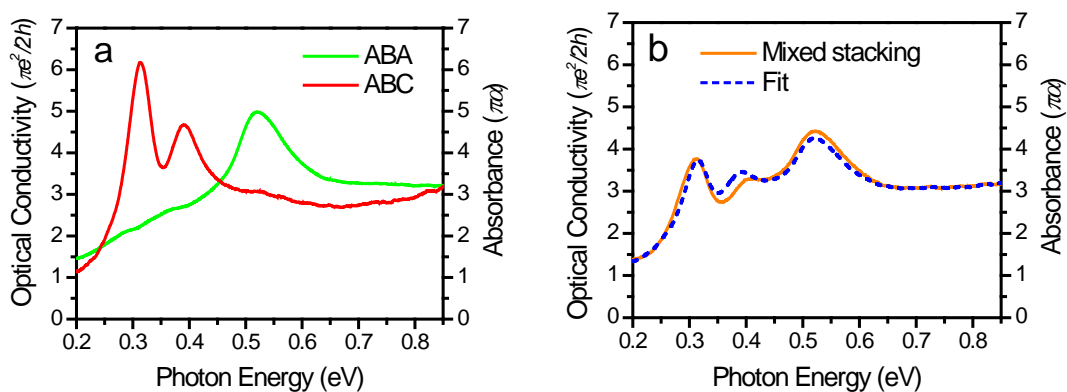
Figure 5.2 Optical conductivity of different trilayer graphene samples. **(a)** Spectra of trilayer with ABA (green line) and ABC (red line) stacking order. **(b)** The spectrum of a trilayer sample with mixed stacking order (orange line). The spectrum can be described as a linear combination of 67% ABA stacking and 33% ABC stacking (dashed blue line). The slight discrepancy may reflect different doping and strain levels.

along the direction of the honeycomb lattice by a carbon-carbon bond length. We associate these two basic types of spectra with the two distinct low-energy crystallographic structures of trilayer graphene [11]: ABA (Bernal) or ABC (rhombohedral) stacking (Figure 5.1). The existence of different stacking order in FLG and its strong impact on electronic structure have been demonstrated experimentally by IR spectroscopy [5]. Following this work we assign the first and second kind of spectrum to trilayer graphene with ABA and ABC stacking order. The third kind of spectrum is attributed to the trilayer samples with mixed stacking order.

For tetralayer graphene, we also observed two distinctive groups of IR response in the optical conductivity spectra, as shown in Figure 5.3. The first kind of spectrum (green line) shows two absorption peak at 0.25 and 0.60 eV, which matches the result of ABAB tetralayer graphene [3]. The second kind of spectrum (red line) exhibits two narrow and strong peaks at 0.26 and 0.36 eV. This distinct IR response spectrum of tetralayer graphene is associated with the ABCA-stacked tetralayer according to our previous IR study on tetralayer graphene [5].
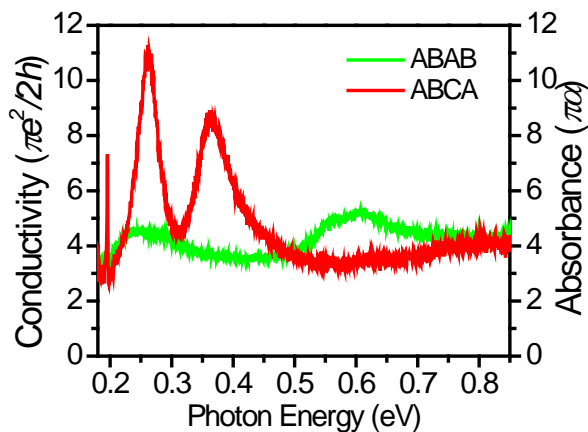
Figure 5.3 Optical conductivity spectra of tetralayer graphene samples with ABAB (green line) and ABCA (red line) stacking order. The shape line of the ABCA spectrum near 0.2 eV is due to Fano resonance of zone-center G-mode phonon with the continuum electronic transitions.

5.4 Imaging Stacking Order in Trilayer Graphene

5.4.1 Raman 2D-Mode of ABA and ABC Trilayer

We observed consistent differences in the lineshape of the Raman 2D-mode between samples with Bernal and rhombohedral stacking. Figure 5.4 displays results for trilayer samples. For all excitation photon energies, the ABC trilayers displayed more asymmetric and broader lines than ABA trilayers. In particular, we observed a sharp peak and an enhanced shoulder in the ABC spectra for all excitation photon energies. This signature of stacking order is clear in all pristine trilayer samples. (We note that chemically processed samples may exhibit broadened 2D-mode spectra from doping and disorder. This may obscure the stacking-order signature.)
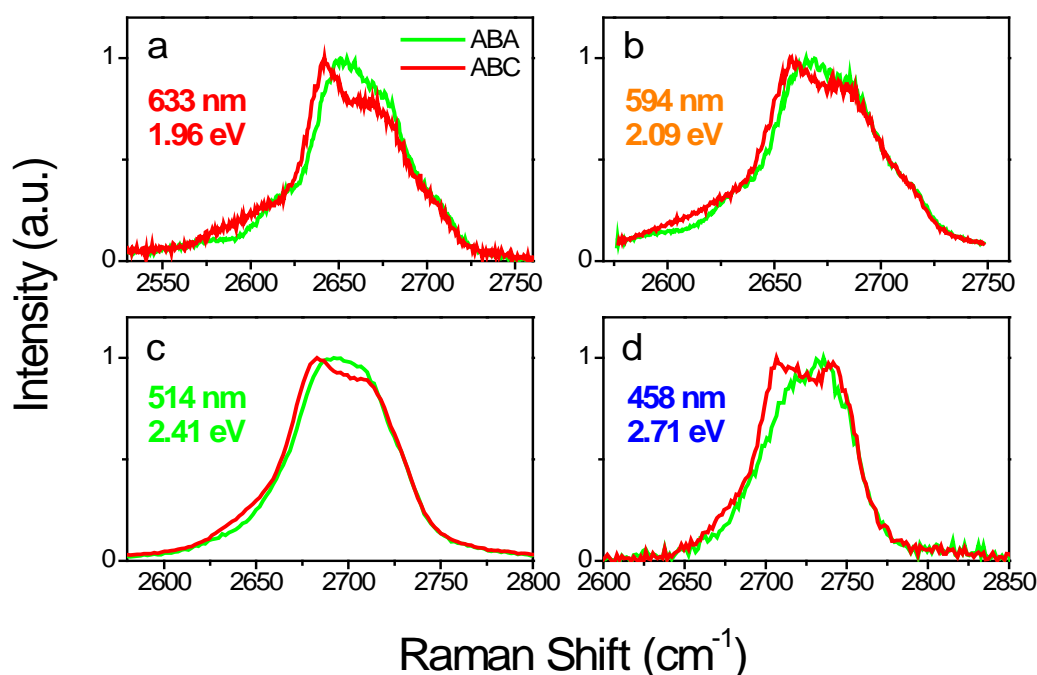
Figure 5.4. Raman spectra of the 2D-mode of ABA (green line) and ABC (red line) trilayer graphene samples at four different laser excitation wavelengths. The increase in the average Raman shift with excitation photon energy is an expected consequence of the double-resonance process that selectively couples phonons with different momenta around the *K*-point.

The 2D band arises from a double-resonance process that involves inter-valley (i.e. between the K and K' point) scattering in the Brillouin zone and resonant electronic transitions. As trilayer graphene has three valence and three conduction bands, many electronic transitions can contribute to the 2D band. A recent study by group theory shows that up to 15 peaks in the 2D band are possible in ABA trilayer graphene [36]. In practice, however, we may consider fewer transitions, since many of them have close energy separations. We have fit the 2D-mode Raman spectra of ABA and ABC trilayer graphene with multiple Lorentzian functions. The FWHM of all the Lorenztian functions are fixed to be the same as that of the 2D band of monolayer (~25cm^{-1}). We only vary the peak positions and intensities. We found that a good fit can be achieved with 6 Lorentzian functions. Figure 5.5 (a-h) shows such for both ABA and ABC trilayer graphene samples for all excitation energies. The differences in the spectra and, correspondingly, in the fitting parameters, become more prominent as the excitation photon energy decreases. This trend presumably reflects the more pronounced differences in electronic structure at low energies for the two stacking orders. We have also considered the shift of the 2D band as a function of the excitation energy. We extract the mean Raman shift by averaging the 2D band spectra weighted with the spectral intensity. As shown in Figure 5.6, ABA trilayer graphene has a higher mean 2D-band Raman shift than ABC trilayer, but a very similar dispersion.

While the 2D mode has been applied widely to identify mono- and bi-layer samples [7,26,32,33], its application to analysis of trilayers has been more limited because of the lack of consensus on the 2D lineshape of different trilayer samples. This mode was found to have a more asymmetric shape in some studies [7,36,37] and a less

asymmetric shape in others [33]. Our results suggest that such variation may arise from the difference in stacking order among samples.
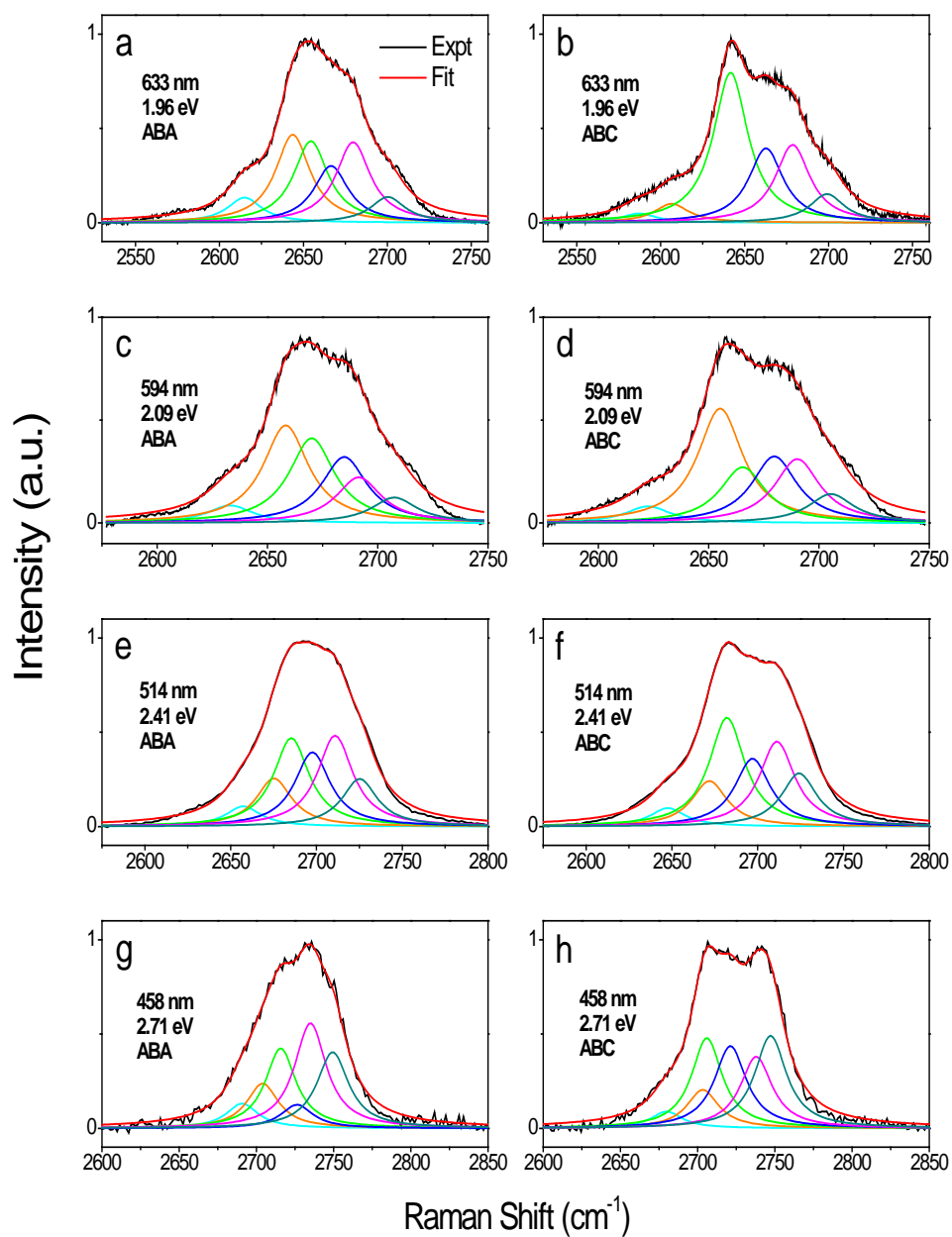
Figure 5.5. 2D-mode Raman spectra of graphene trilayers with ABA (left) and ABC (right) stacking order at different excitation energies. The black lines are experimental data. The red lines are fits by 6 Lorentzian functions, all with a FHWM of 25 cm^{-1}. The lines of other colors are the Lorentzian components of the fits.
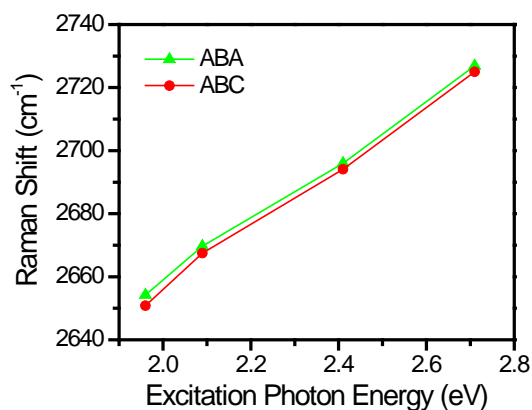
Figure 5.6 Mean Raman shift of the 2D-mode features for graphene trilayer with ABA (green triangles) and ABC (red dots) stacking order for different excitation laser energies. The data are obtained by averaging the Raman shifts weighted by the corresponding spectral intensity in the 2D-mode spectra.

5.4.2 Raman G-Mode of ABA and ABC Trilayer

We have also examined the Raman G-mode of ABA and ABC trilayer graphene (Figure 5.7). The spectra were taken in ABA and ABC stacking domains of a single trilayer sample to maintain similar doping and strain condition. (Detailed information about the coexistence of such stacking domains is discussed below.) Only slight differences are observable in the G-mode frequency and lineshape, as well as in the 2D/G ratio. As G-mode is not influenced by electronic resonances, we ascribe the small red shift (~1 cm^{-1}) of the G-mode frequency of ABC trilayer compared to ABA trilayer to the slight difference of their phonon band structures [38]. In addition, the very weak D-mode feature [D/G<0.005, as shown in the inset of Figure 5.7 (b)] indicates the high crystalline quality in the trilayer areas of either stacking order.

The similarity of the G-mode features in ABA and ABC trilayers implies that the greater sensitivity of the 2D mode to stacking order is the result of differences in electronic structure. The Raman 2D mode is expected to be affected by the electronic
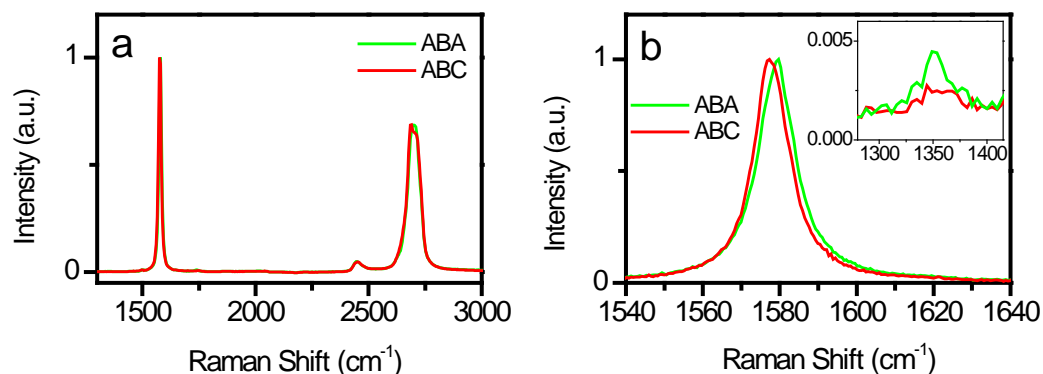
Figure 5.7 Raman spectra of graphene trilayers with ABA (green line) and ABC (red line) stacking order. **(a)** Raman spectra over a broad energy range. **(b)** Details of G-mode and D-mode (inset) spectra. The excitation laser wavelength is 514 nm.

properties since it arises from a double-resonance process that involves transitions among various electronic states [7,26,30,31]. It is this sensitivity that has rendered the 2D-mode a fingerprint for mono- and bi-layer graphene samples [26,32].

5.4.3 Raman Imaging by 2D-Mode Line Width

In order to visualize the spatial distribution of the stacking domains, we implemented a method for Raman mapping. To this end, we needed to define a quantity that could effectively encode the differences between the Raman spectra for the two different stacking orders. We examined several schemes, including ones based on changes in the centroid and asymmetry of the Raman spectrum. We found, however, that using the spectral width of the 2D mode captured the differences in a simple and robust fashion. To extract the width, we fit the spectrum at each pixel in the spatial mapping to a single Lorentzian function. We then produced spatial images by displaying the full width at half maximum (FWHM) of the fit function for each pixel in the image. A direct
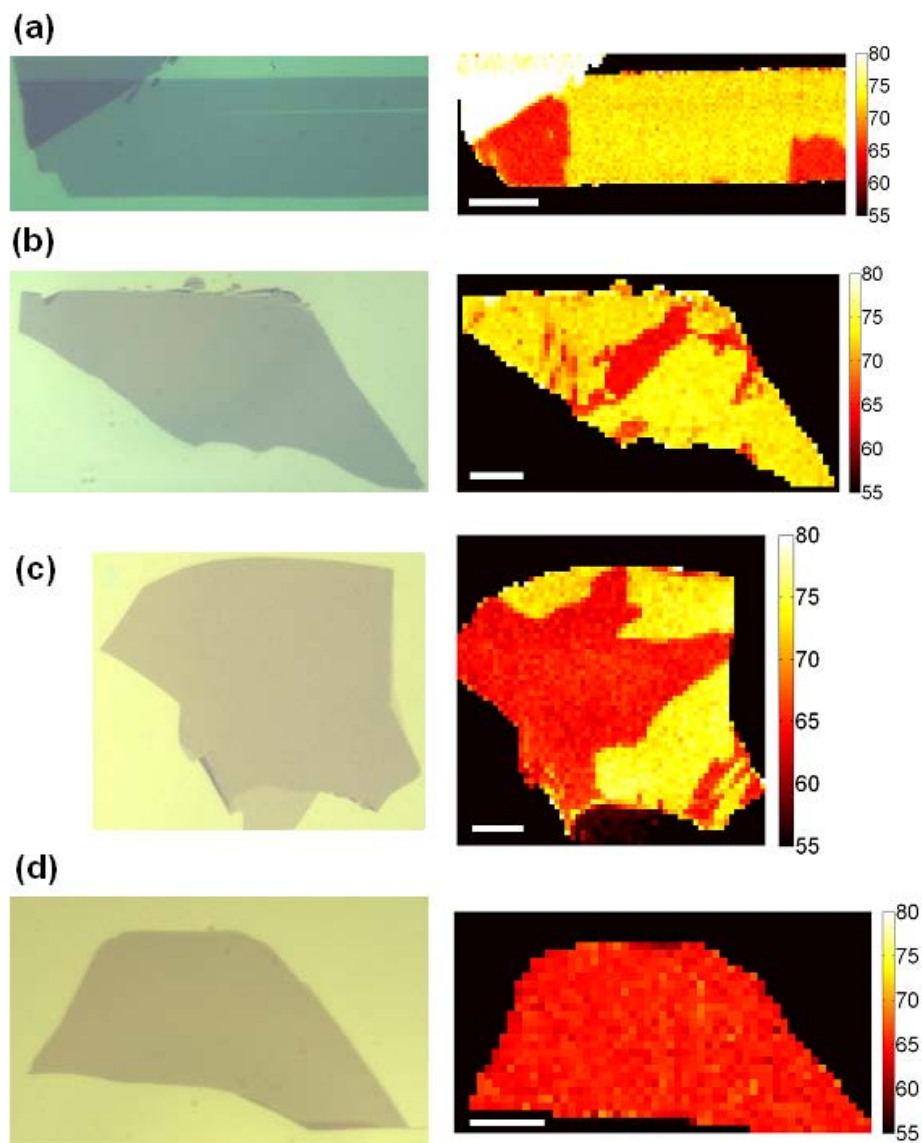
Figure 5.8 Optical images (left column) and spatial maps of the spectral width of Raman 2D-mode feature (right column) for trilayer graphene samples. The homogeneity of the optical images shows the uniformity of the layer thickness of the four samples. The Raman images, taken with 514-nm excitation, are color coded according to the width of the Raman feature (FWHM in units of cm^{-1}). The red and yellow regions in the images correspond, respectively, to ABA and ABC trilayer graphene domains. The step size in the scans is 0.5 μm for (a), and 1 μm for (b)-(d). The scale bars are 10 μm in length. Similar results can be obtained using other wavelengths for the excitation laser.

determination of the width from the spectra can also be used to generate spatial maps. This procedure led, however, to noisier images.

Figure 5.8 presents examples of Raman mapping of the trilayer graphene samples that exhibit domains of differing stacking order. For comparison, we also show optical

images of these samples. No difference in the optical contrast is observed across the full area of the samples, indicating that each sample is entirely homogeneous in thickness. We have further performed IR measurements to confirm the results of the Raman mapping. The IR spectra obtained in the different regions of these four samples corresponds precisely to those of ABA and ABC trilayers (Figure 5.2).

5.4.4 Doping Effect on 2D-Mode Line Width

We note that exfoliated graphene samples exhibit spatially inhomogeneous carrier doping effects when deposited on typical insulating substrates [34,39]. Could this charging effect influence our Raman data? To address this issue, we performed the Raman measurements on free-standing ABC trilayer graphene samples. The samples are prepared by mechanical exfoliation of kish graphite on quartz substrates with pre-patterned trenches. Some parts of the ABC trilayer graphene covering the trenches are suspended. They are thus isolated from any perturbation induced by the substrates. Figure 5.9 shows the Raman 2D-mode spectra recorded for supported and suspended parts of a single ABC trilayer sample. Apart from a slight shift of frequency, both spectra show essentially the same lineshape. The difference of FWHM obtained by single-Lorentzian fits is within 1cm^{-1}. According to the literature [34,39-41], such substrates typically induce an unintentional doping of $n \sim 5 \times 10^{12}$ cm^{-2} in graphene, which varies from sample to sample and is also inhomogeneously distributed on a submicrometer scale within a given graphene sample. Our results show that the corresponding changes in the 2D-mode lineshape are very slight and do not impair our ability to distinguish between ABA and ABC stacking order.
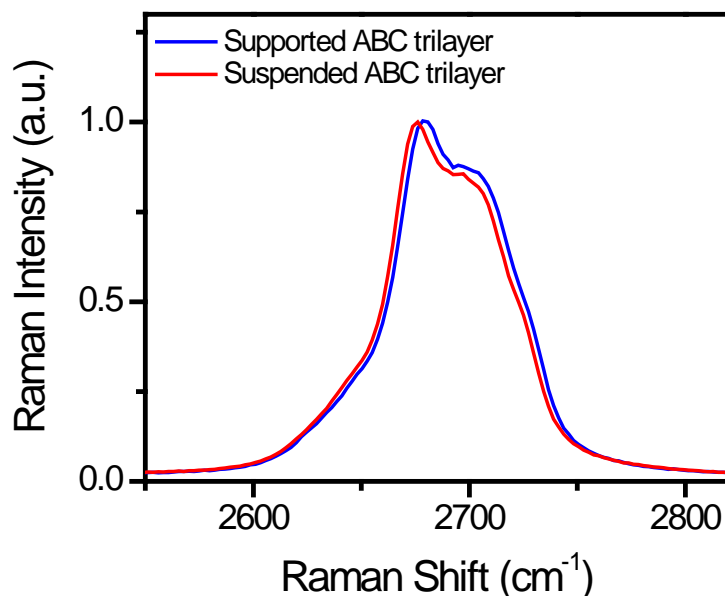
Figure 5.9 Raman 2D-mode spectra from an ABC trilayer sample supported on a quartz substrate (blue line) and suspended over a trench. The two spectra show very similar lineshapes and widths. The difference of FWHMs obtained by the single-Lorentzian fits is less than 1 cm^{-1}. The excitation laser wavelength is 532 nm.

5.4.5 Statistics of ABA and ABC Areas in Trilayers

The coexistence of ABA and ABC stacking order is striking. Among the 45 trilayer samples that we prepared, 26 exhibited purely ABA stacking, while 19 displayed mixed ABA and ABC stacking. None of the samples showed purely ABC stacking. In the 19 samples of mixed stacking order, only 5 samples contain large (>200 μm^2), homogeneous regions of ABC-stacking order, as in Figure 5.8 (a), (c). If we consider the total area associated with the two different stacking orders, we find that ~ 85% area of our samples corresponds to ABA stacking and ~ 15% to ABC stacking. This result is comparable to that obtained in earlier x-ray diffraction studies of graphite [42,43], which

indicate that graphite typically contains 80% of the Bernal structure, 14% of the rhombohedral structure, and 6% of a disordered structure [42]. The similarity of our results suggests that the different stacking orders observed in trilayer graphene originate from the pristine structure of the graphite used in the exfoliation process, which is not modified during the exfoliation of the layers. This claim is supported by the complicated patterns of stacking domains in our samples. One would not expect these patterns to be produced by mechanical processing.

5.5 Imaging Stacking Order in Tetralayer Graphene

The method of imaging stacking order by Raman spectroscopy can be generalized to investigations of FLG of greater thickness. Here we show the results for tetralayer graphene. Figure 5.10 shows the 2D-mode Raman spectra for ABAB (green line) and ABCA (red line) tetralayer graphene (Detailed information on the stability and IR spectroscopy of these two types of tetralayer graphene can be found in the references [5,11]). By carefully examining the spectra, we observed distinct lineshapes for the two stacking orders. ABCA tetralayers show more structured, asymmetric lines with greater widths than the ABAB tetralayers. In particular, we observed a sharp peak and an enhanced shoulder in the ABCA spectrum at 2680 cm^{-1} and 2640 cm^{-1}. Such distinctions in the 2D-mode spectra are observed in all ABAB and ABCA tetralayer samples. We note that both the ABC trilayer [Figure 5.4(c)] and the ABCA tetralayer exhibit similar 2D-mode lineshapes, indicating that the asymmetric and broadened features are characteristics of this stacking order.
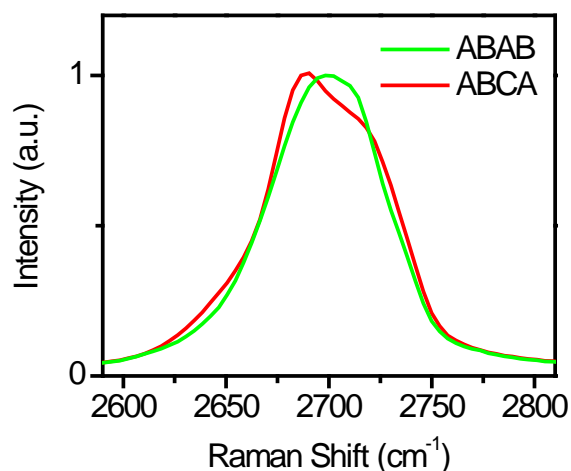
Figure 5.10 Raman 2D-mode spectra for the tetralayer graphene samples of ABAB (green line) and ABCA (red line) stacking order.
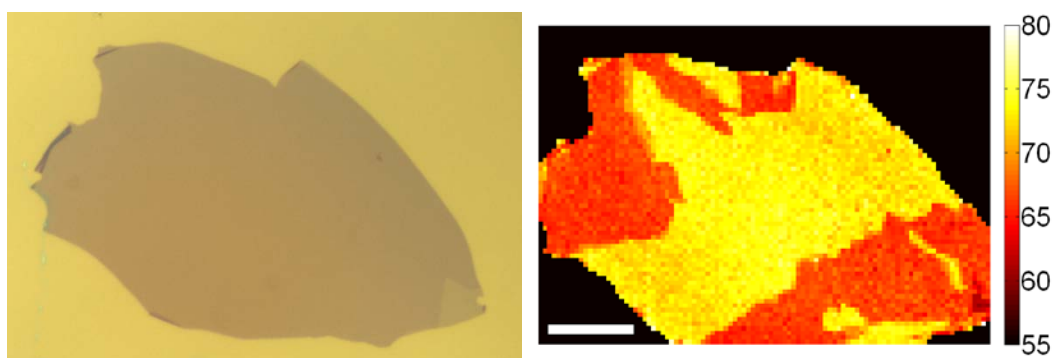
Figure 5.11 Optical (left) and Raman images (right) of a specific tetralayer graphene sample. The optical image shows the uniformity of the layer thickness of the sample. The Raman map of the spectral width of Raman 2D-mode exhibits domains with different stacking order. The Raman images, obtained with 514-nm excitation, are color coded according to the FWHM of the Raman feature (in units of cm^{-1}). The red and yellow regions in the images correspond, respectively, to tetralayer graphene with ABAB and ABCA stacking. The step size for the Raman mapping was 1 μm. The length of the scale bar is 20 μm.

Fig. 5.11 (a) and (b) show, respectively, the optical image and Raman image of a tetralayer graphene sample with mixed (ABAB and ABCA) stacking order. The homogeneous optical image indicates that the sample is entirely graphene of 4 layers in thickness. The Raman image, which encodes the 2D-mode spectral width (FWHM)

extracted from a single Lorentzian fit, shows sharp contrast for regions of different stacking order. The stacking sequences determined by Raman spectroscopy in these domains were further confirmed by IR spectroscopy.

The characteristics of the stacking domains based on an analysis of 56 samples, were found to be similar to those for trilayer graphene. In particular, the ratio of the area of ABAB to ABCA stacking was 85:15. The similarity of the domains in tetralayer and trilayer graphene confirms the common origin of the different stacking sequences, namely, the stacking order of the kish graphite, which remains unchanged during the exfoliation process.

5.6 Thermodynamic Stability of ABC Stacking Order

The ability to directly visualize the domains of stacking order provides a means of assessing the thermodynamic stability of the different structures. Our Raman images show that Bernal and rhombohedral stacking order can coexist in micron-sized domains of trilayer thickness at room temperature. In addition, we investigated the thermodynamic stability of the ABC stacking order in trilayer graphene by annealing the samples to high temperatures. We first chose a piece of pristine trilayer sample with mixed stacking order and examined its domains of stacking by the Raman mapping of the FWHM of the Raman 2D mode [Figure 5.12 (a), which is the same as Figure 5.4 (c)]. The ABA and ABC domains are clearly encoded as the red and yellow colored regions in the Raman image. We then annealed the same sample in an argon environment at different temperatures and subsequently examined the structure of the domains by Raman mapping. We found that the domains of ABC stacking remained stable up to 800 ºC, the maximum

(a)　　　　　　　　　　　　　　　　(b)
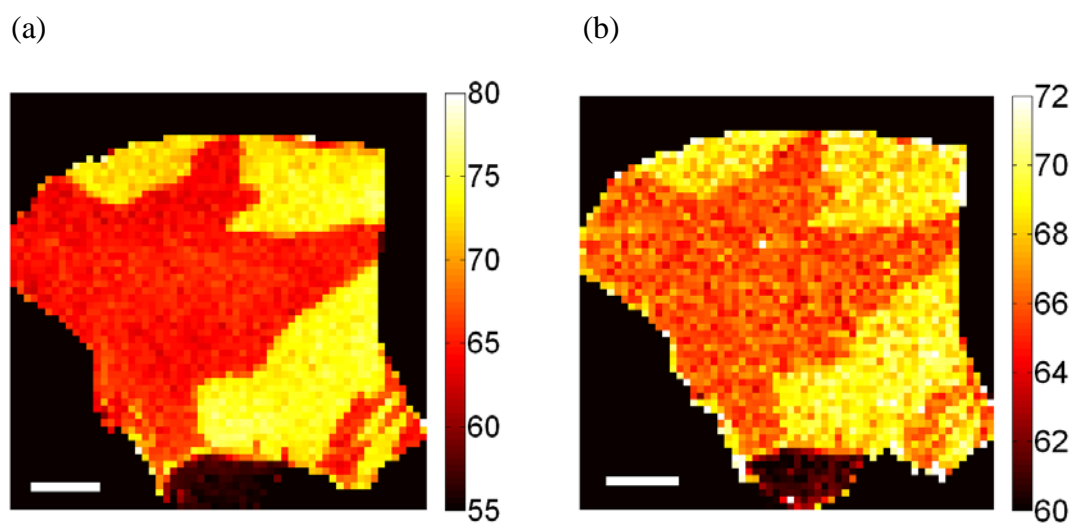
Figure 5.12 Influence of thermal annealing on the domains of different stacking order in trilayer graphene. Panels (a) and (b) display spatial maps of the spectral width of Raman 2D-mode feature for a pristine trilayer graphene sample (a) and for the same sample after thermal annealing in an argon environment at 500 ºC for 10 hours (b). The Raman images are color coded according to the width of the Raman feature (FWHM in units of cm^{-1}). The red and yellow regions in the images correspond, respectively, to ABA and ABC trilayer graphene domains. The scale bars are 10 μm in length.

annealing temperature in our experiment. Figure 5.12 (b) displays the Raman image after annealing the sample at 500 ºC for 10 hours. The domains of ABA and ABC stacking, still recognizable as the red and yellow regions, are unaltered. We note that the image contrast in the Raman mapping between the domains of ABA and ABC stacking is reduced by the thermal processing cycle. We attribute this to the introduction of excess doping and disorder in the sample, leading to broadening of the Raman 2D feature. We further confirmed the stacking order by IR spectroscopy. This result is consistent with the stability of bulk rhombohedral graphite to over 1000 ºC [44,45]. Our result shows that this stability is retained even for *atomically thin* rhombohedrally stacked crystallites

5.7 Conclusion

In conclusion, we have demonstrated Raman spectroscopy to be an effective tool for the characterization of stacking order in few-layer graphene. Bernal (ABA) and rhombohedral (ABC) tri- and tetra-layer graphene samples exhibit clear differences in the lineshape and width of the Raman 2D line. By Raman spatial mapping, we find that for typical exfoliated tri- and tetra-layer samples about 15% of the area has rhombohedral stacking rather than the usual Bernal stacking. The domains of rhombohedral stacking are generally only of micron length. The Raman technique presented in this paper should accelerate the research on FLG. For instance, various studies [11,13,16,20] have predicted that a significant and electrically tunable band gap can be opened in rhombohedral trilayer graphene by the application of an electric field. However, for Bernal trilayers with their differing symmetry, this effect will be much smaller. With the Raman technique presented here, we can readily identify the domains of stacking in FLG and can test these predictions experimentally by constructing an appropriate gated device. In addition to assuring the desired crystal structure of samples, the Raman mapping capabilities allow identification of domain boundaries. This information should permit detailed exploration of the structural and electronic properties at these interfaces.

References

[1]   C. H. Lui, Z. Li, Z. Chen, P. V. Klimov, L. E. Brus & T. F. Heinz. "Imaging Stacking Order in Few-Layer Graphene", *Nano Lett.* **11**, 164-169, (2010).

[2]   T. Ohta, A. Bostwick, J. L. McChesney, T. Seyller, K. Horn & E. Rotenberg. "Interlayer Interaction and Electronic Screening in Multilayer Graphene Investigated with Angle-Resolved Photoemission Spectroscopy", *Phys. Rev. Lett.* **98**, 206802, (2007).

[3]   K. F. Mak, M. Y. Sfeir, J. A. Misewich & T. F. Heinz. "The evolution of electronic structure in few-layer graphene revealed by optical spectroscopy", *Proc. Natl. Acad. Sci. U. S. A.* **107**, 14999, (2010).

[4]   M. F. Craciun, S. Russo, M. Yamamoto, J. B. Oostinga, A. F. Morpurgo & S. Thrucha. "Trilayer graphene is a semimetal with a gate-tunable band overlap", *Nat. Nanotechnol.* **4**, 383, (2009).

[5]   K. F. Mak, J. Shan & T. F. Heinz. "Electronic Structure of Few-Layer Graphene: Experimental Demonstration of Strong Dependence on Stacking Sequence", *Phys. Rev. Lett.* **104**, 176404, (2010).

[6]   M. Bruna & S. Borini. "Observation of Raman G -band splitting in top-doped few-layer graphene", *Phys. Rev. B* **81**, 125421, (2010).

[7]   L. M. Malard, M. A. Pimenta, G. Dresselhaus & M. S. Dresselhaus. "Raman spectroscopy in graphene", *Physics Reports* **473**, 51, (2009).

[8]   N. Jung, N. Kim, S. Jockusch, N. J. Turro, P. Kim & L. Brus. "Charge Transfer Chemical Doping of Few Layer Graphenes: Charge Distribution and Band Gap Formation", *Nano Lett.* **9**, 4133, (2009).

[9]   S. Latil & L. Henrard. "Charge carriers in few-layer graphene films", *Phys. Rev. Lett.* **97**, 036803, (2006).

[10]   H. K. Min & A. H. MacDonald. "Electronic Structure of Multilayer Graphene", *Progress of Theoretical Physics Supplement* **176**, 227, (2008).

[11]   M. Aoki & H. Amawashi. "Dependence of band structures on stacking and field in layered graphene", *Solid State Commun.* **142**, 123, (2007).

[12]   W. Norimatsu & M. Kusunoki. "Selective formation of ABC-stacked graphene layers on SiC(0001)", *Phys. Rev. B* **81**, 161410, (2010).

[13]   F. Guinea, A. H. C. Neto & N. M. R. Peres. "Electronic states and Landau levels in graphene stacks", *Phys. Rev. B* **73**, 245426, (2006).

[14]   F. Guinea, A. H. Castro & N. M. R. Peres. "Electronic properties of stacks of graphene layers", *Solid State Commun.* **143**, 116, (2007).

[15]   C. L. Lu, C. P. Chang, Y. C. Huang, J. H. Ho, C. C. Hwang & M. F. Lin. "Electronic properties of AA- and ABC-stacked few-layer graphites", *J. Phys. Soc. Jpn.* **76**, 024701, (2007).

[16]   C. P. Chang, J. Wang, C. L. Lu, Y. C. Huang, M. F. Lin & R. B. Chen. "Optical properties of simple hexagonal and rhombohedral few-layer graphenes in an electric field", *J. Appl. Phys.* **103**, 103109, (2008).

[17]   A. A. Avetisyan, B. Partoens & F. M. Peeters. "Electric-field control of the band gap and Fermi energy in graphene multilayers by top and back gates", *Phys. Rev. B* **80**, 195401, (2009).

[18]   A. A. Avetisyan, B. Partoens & F. M. Peeters. "Electric field tuning of the band gap in graphene multilayers", *Phys. Rev. B* **79**, 035421, (2009).

[19]   M. Koshino & E. McCann. "Gate-induced interlayer asymmetry in ABA-stacked trilayer graphene", *Phys. Rev. B* **79**, 125443, (2009).

[20]   A. A. Avetisyan, B. Partoens & F. M. Peeters. "Stacking order dependent electric field tuning of the band gap in graphene multilayers", *Phys. Rev. B* **81**, 115432, (2010).

[21]   M. Koshino. "Interlayer screening effect in graphene multilayers with ABA and ABC stacking", *Phys. Rev. B 81*, 125304, (2010).

[22]   E. McCann & M. Koshino. "Spin-orbit coupling and broken spin degeneracy in multilayer graphene", *Phys. Rev. B 81*, 241409, (2010).

[23]   M. Otani, M. Koshino, Y. Takagi & S. Okada. "Intrinsic magnetic moment on (0001) surfaces of rhombohedral graphite", *Phys. Rev. B 81*, 161403, (2010).

[24]   M. Otani, Y. Takagi, M. Koshino & S. Okada. "Phase control of magnetic state of graphite thin films by electric field", *Appl. Phys. Lett. 96*, 242504, (2010).

[25]   M. Nakamura & L. Hirasawa. "Electric transport and magnetic properties in multilayer graphene", *Phys. Rev. B 77*, 045429, (2008).

[26]   A. C. Ferrari. "Raman spectroscopy of graphene and graphite: Disorder, electron-phonon coupling, doping and nonadiabatic effects", *Solid State Commun. 143*, 47, (2007).

[27]   A. Das, S. Pisana, B. Chakraborty, S. Piscanec, S. K. Saha, U. V. Waghmare, K. S. Novoselov, H. R. Krishnamurthy, A. K. Geim, A. C. Ferrari & A. K. Sood. "Monitoring dopants by Raman scattering in an electrochemically top-gated graphene transistor", *Nat. Nanotechnol. 3*, 210, (2008).

[28]   M. Y. Huang, H. G. Yan, C. Y. Chen, D. H. Song, T. F. Heinz & J. Hone. "Phonon softening and crystallographic orientation of strained graphene studied by Raman spectroscopy", *Proc. Natl. Acad. Sci. U. S. A. 106*, 7304, (2009).

[29]   T. M. G. Mohiuddin, A. Lombardo, R. R. Nair, A. Bonetti, G. Savini, R. Jalil, N. Bonini, D. M. Basko, C. Galiotis, N. Marzari, K. S. Novoselov, A. K. Geim & A. C. Ferrari. "Uniaxial strain in graphene by Raman spectroscopy: G peak splitting, Gruneisen parameters, and sample orientation", *Phys. Rev. B 79*, 205433, (2009).

[30]   C. Thomsen & S. Reich. "Double resonant Raman scattering in graphite", *Phys. Rev. Lett. 85*, 5214, (2000).

[31]   R. Saito, A. Jorio, A. G. Souza Filho, G. Dresselhaus, M. S. Dresselhaus & M. A. Pimenta. "Probing Phonon Dispersion Relations of Graphite by Double Resonance Raman Scattering", *Phys. Rev. Lett. 88*, 027401, (2001).

[32]   A. C. Ferrari, J. C. Meyer, V. Scardaci, C. Casiraghi, M. Lazzeri, F. Mauri, S. Piscanec, D. Jiang, K. S. Novoselov, S. Roth & A. K. Geim. "Raman spectrum of graphene and graphene layers", *Phys. Rev. Lett. 97*, 187401, (2006).

[33]   J. S. Park, A. Reina, R. Saito, J. Kong, G. Dresselhaus & M. S. Dresselhaus. "G ' band Raman spectra of single, double and triple layer graphene", *Carbon 47*, 1303, (2009).

[34]   S. Berciaud, S. Ryu, L. E. Brus & T. F. Heinz. "Probing the Intrinsic Properties of Exfoliated Graphene: Raman Spectroscopy of Free-Standing Monolayers", *Nano Lett. 9*, 346, (2009).

[35]   K. F. Mak, M. Y. Sfeir, Y. Wu, C. H. Lui, J. A. Misewich & T. F. Heinz. "Measurement of the Optical Conductivity of Graphene", *Phys. Rev. Lett. 101*, 196405, (2008).

[36]   L. M. Malard, M. H. D. Guimaraes, D. L. Mafra, M. S. C. Mazzoni & A. Jorio. "Group-theory analysis of electrons and phonons in N-layer graphene systems", *Phys. Rev. B 79*, 125426, (2009).

[37]   D. Graf, F. Molitor, K. Ensslin, C. Stampfer, A. Jungen, C. Hierold & L. Wirtz. "Spatially resolved raman spectroscopy of single- and few-layer graphene", *Nano Lett. 7*, 238, (2007).

[38]   J. A. Yan, W. Y. Ruan & M. Y. Chou. "Phonon dispersions and vibrational properties of monolayer, bilayer, and trilayer graphene: Density-functional perturbation theory", *Phys. Rev. B 77*, 125401, (2008).

[39]   C. Stampfer, F. Molitor, D. Graf, K. Ensslin, A. Jungen, C. Hierold & L. Wirtz. "Raman imaging of doping domains in graphene on SiO2", *Appl. Phys. Lett. 91*, 241907, (2007).

[40]   J. Martin, N. Akerman, G. Ulbricht, T. Lohmann, J. H. Smet, K. Von Klitzing & A. Yacoby. "Observation of electron-hole puddles in graphene using a scanning single-electron transistor", *Nature Physics 4*, 144, (2008).

[41]   C. Casiraghi, S. Pisana, K. S. Novoselov, A. K. Geim & A. C. Ferrari. "Raman fingerprint of charged impurities in graphene", *Appl. Phys. Lett.* **91**, 233108, (2007).

[42]   H. Lipson & A. R. Stokes. "The structure of graphite", *Proc. R. Soc. A* **181**, 0101, (1942).

[43]   H. A. Wilhelm, B. Croset & G. Medjahdi. "Proportion and dispersion of rhombohedral sequences in the hexagonal structure of graphite powders", *Carbon* **45**, 2356, (2007).

[44]   E. Matuyama. "Rate of transformation of rhombohedral graphite at high temperatures", *Nature* **178**, 1459, (1956).

[45]   E. J. Freise & A. Kelly. "The deformation of graphite crystals and the production of the rhombohedral form", *Philos. Mag.* **8**, 1519, (1963).

Chapter 6

Electric-Field Induced Changes in the Band Structure of Trilayer Graphene: The Effect of Crystallographic Stacking Order

After characterizing the stacking domains in few-layer graphene (FLG) with the infrared (IR) and Raman techniques presented in the previous chapter, we go forward to investigating the influence of stacking order on the electronic properties of FLG. In this chapter, we study the influence of a strong perpendicular electric field on the band structure of ABA and ABC graphene trilayers by means of IR spectroscopy. Distinct IR response is observed in the two types of trilayer with different stacking order. We observe an electrically tunable band gap of over 100 meV in ABC trilayers, while no band gap is found for ABA trilayers.

6.1 Introduction

Graphene trilayers are promising materials for both basic science and technological innovation. While keeping the high carrier mobility and two-dimensional electronic characters of graphene monolayer, the trilayers have more flexibility in the electronic structure. They can exist in two stable crystallographic forms: ABA (Bernal) and ABC (rhombohedral) stacking sequences (Figure 5.1). The distinct crystal structures associated with these two stacking orders have been predicted to strongly influence

various electronic properties of trilayer graphene [1-11], in particular the possibility of opening a wide controlled band gap with the application of an electric field perpendicular to the graphene plane [1,3,9,10,12]. In this aspect, ABC trilayers are gapless semiconductors. Their low-energy conduction and valence bands touch one another at a single Fermi point (or triple Fermi points if trigonal warping is considered) due to the discrete symmetries (translational invariance, time reversal and space inversion) in ABC trilayers [13,14]. Calculations by tight-binding (TB) model [3,8,10] and density functional theory (DFT) [13] have shown that a perpendicular electric field can break the inversion symmetry of ABC trilayer and induce a band gap that increases monotonically with the field strength. This makes ABC trilayer an attractive candidate for novel electronic devices with a wide tunable band gap. While such band-gap opening is also possible in graphene bilayer [15,16], ABC trilayer can produce a larger band gap under the same field strength due to their larger thickness [8]. On the other hand, ABA trilayers are semimetals with a finite band overlap [17,18]. TB calculations have predicted essentially no band gap in ABA trilayers for any strength of uniform electric field [9]. Though a small band gap was predicted in ABA trilayer under a strong non-uniform electric field [1], it has only minimal influence on the transport and optical properties because the Fermi level is well above the band edge due to excess doping introduced by non-uniform field. These predictions are consistent with a recent transport measurement that showed a tunable band overlap in gated ABA trilayers [18]. Therefore at all practical points of view, ABA trilayers are essentially semimetals under external potential. While these distinct properties of ABA and ABC trilayer has been intensively studied

theoretically, experimental evidences of these stacking order effects have, however, been lacking up to date.

In this chapter, we carry out a detailed experimental study of the electronic response of trilayer graphene, both of ABA and ABC stacking order, to a strong perpendicular electric field ~0.2 V/nm. The electric field is applied by using an electrolyte top gate or SiO_2 back gate that induce high density of doping and different potential in each graphene layer. The resultant change of the band structure is probed by infrared (IR) conductivity measurements. Our results show direct spectroscopic signatures of the opening of a large and tunable band gap up to ~120 meV on ABC trilayer graphene. Such a band gap is not observable ABA trilayer graphene under an electric field of similar strength. On the other hand, we observed a significant asymmetry in the optical conductivity upon electrostatic doping of electrons and holes in ABA trilayer, which is stronger than those observed in bilayer and ABC trilayer. These findings directly reveal the critical role played by crystallographic structure on the band-gap-opening capability as well as the band structure asymmetry in trilayer graphene.

6.2 Experiment and Analysis

6.2.1 Sample Preparation and Characterization

In our experiment, we investigated graphene trilayer samples that were prepared by mechanical exfoliation of kish graphite (Toshiba) on silicon substrates coated with a 300-nm oxide layer. We characterized the samples by both IR and Raman spectroscopy, as described in details in Chapter 5. The IR measurements were made by the U12 IR beam line of the National Synchrotron Light Source at Brookhaven national Laboratory.

The optical radiation passing through or reflected by the sample was detected with a micro-Fourier Transform Infrared apparatus equipped with an MgCdTe detector under nitrogen purge. The beam size on the sample is about 10 μm. The transmission and reflectance spectra of the sample were obtained by normalizing the sample spectrum with that from the bare substrate. The optical conductivity in the spectral range of 0.2-1.2 eV was then extracted. The high-energy part (>0.8 eV) of the conductivity allows us to determine the sample thickness and the low-energy part (< 0.7 eV) determines the stacking order. The trilayer samples were later examined by Raman spectroscopy as described in chapter 5. Using the stacking-order signature of the 2D-mode feature, we can visualize the spatial distribution of the ABA and ABC stacking domains in trilayer samples. We then chose samples with large (>200 μm^2) homogeneous domains of ABA or ABC stacking order to fabricate devices for gating measurements.

6.2.2 Device Fabrication

Electrical contacts to the samples were made by electron-beam lithography and electron-beam evaporation of Au (50 nm). The measurements were carried out either with SiO_2 back gate or polymer electrolyte top gate. For the top gate measurement, a large Au electrode was deposited within 100 μm of the trilayer samples to serve as a top gate through a transparent polymer matrix. The polymer electrolyte (poly(ethylene oxide)(PEO): $LiClO_4$, 8:1, dissolved in methanol) was cast onto the sample and dried at 110 ℃ in ambient [16]. The optical image and schematic drawing of a trilayer graphene device with PEO top gate is displayed in Figure 6.1. The capacitance of the top gate was ~1.0 μFcm^{-2} and allowed us to induce a charge density of ~10^{13} cm^{-2}. We used the

electrolyte top gate for ABA trilayer samples due to their high gating efficiency. For ABC samples that showed main absorption features in a lower energy ~0.3 eV, we preferred using SiO_2 back gate because the polymer top gate caused some background absorption in this lower-energy range. SiO_2 back gate had, however, a lower gating efficiency and we therefore could only make the measurement on the hole side. On the electron side, we used the polymer top gate and removed the background absorption from the polymer by comparing the spectra at the charge neutrality (*CN*) point with that in SiO_2 back gate.
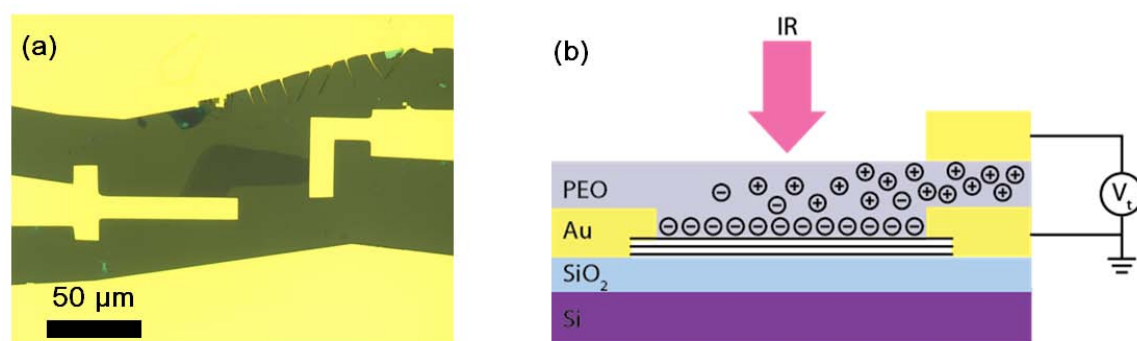
Figure 6.1 **(a)** Optical images of a trilayer graphene device. **(b)** Schematic drawing of the experimental setup. The arrow represents the incident IR beam and the circles represent the ions in the PEO top gate.

6.2.3 Extraction of Optical Conductivity

For the graphene trilayer devices, we measured the transmission spectrum by normalizing the sample spectrum with that from the bare substrate. We then obtained the real part of the optical conductivity (σ) in the spectral range of 0.2-1.0 eV from the transmission spectra by solving the optical problem concerning a thin film on the SiO_2(300-nm)/Si substrate. In our calculation, we neglected the interference at the

sample/PEO interface and considered only the much stronger interference at the SiO_2/Si interface. We also neglected the contribution of the imaginary part of the optical conductivity. The above simplifications were estimated to induce 10% errors in σ, mainly in the spectral range below 0.3 eV, which had negligible influence on the peak positions of σ.

6.2.4 Self-Consistent Calculation of Potentials at Individual Layers

We followed the self-consistent approach of Avetisyan *et al* [1,9,10] to calculate the charge density at each layer of the ABA and ABC graphene trilayers for different total charge density with the consideration of only γ_0 and γ_1. A full calculation with γ_4 and δ showed that the influence of γ_4 and δ on the self-consistent result was negligible. For a single-gate configuration, the potential difference between 1st and 2nd layer and between 2nd and 3rd layer as a function of total charge density *n* and charge density at 2nd (n_2) and 3rd (n_3) layer were $\Delta_{12}(n)=\alpha(n_2+n_3)$ and $\Delta_{23}(n)=\alpha n_3$, where $\alpha=e^2 c_0/\varepsilon_0 \kappa$, with c_0=0.335 nm as the interlayer distance in trilayer. We used the dielectric constant of SiO_2 in the calculation ($\kappa=2.3$). By including these potential differences in the ABA or ABC trilayer Hamiltonian, we calculated the band structure and the associated eigenfunctions, from which we obtained the charge density at each layer again. The calculation was iterated with the new charge distribution until a self-consistent result was reached.

6.3 Optical Conductivity of Gated ABA and ABC Trilayers

Figure 6.2 displays the optical conductivity $\sigma(\hbar\omega)$ of trilayer graphene samples with ABA and ABC stacking order under different gating conditions. For the ABA

trilayer on electrolyte top gate [Figure 6.2 (a)], its conductivity spectrum σ($\hbar\omega$) exhibits

two peak-like features at $\hbar\omega$ = 0.53 and 0.60 eV at the charge neutrality point V_{CN} = -0.65

V. As we increase the bias V (electron side), the amplitude of the higher-energy transition

(0.60 eV) grows and the peak position red shifts, while the lower-energy transition (0.53

eV) subsides and disappears for V - V_{CN} > 0.2 V. As we decrease V (hole side), the lower-

energy peak was enhanced with slight shift of the peak position, while the higher-energy

peak subsides. We observe that the electron and hole transition peaks evolve differently

with the gate voltage [Figure 6.2 (a) and 6.4(a)].
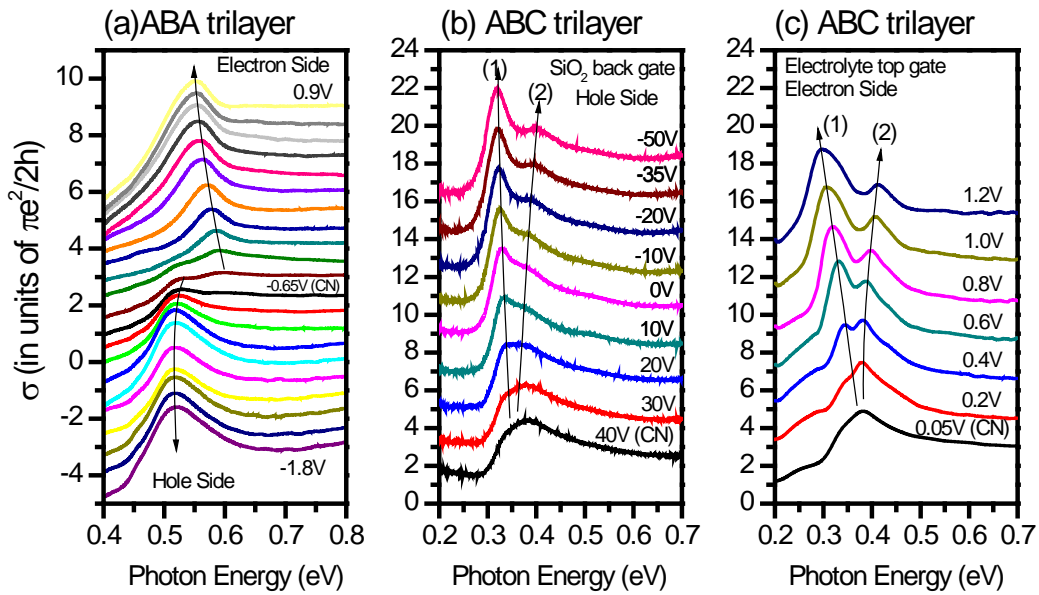
Figure 6.2 Optical conductivity σ($\hbar\omega$) of graphene trilayers at different gate voltages. **(a)** σ($\hbar\omega$) of ABA trilayer graphene by electrolyte top gate. The spectra are displaced for 0.3 units. The charge neutrality (*CN*) point is at V = -0.65 V. The gate voltage V varies from top to bottom as: 0.9, 0.7, 0.5, 0.3, 0.1, -0.1, -0.3, -0.4, -0.5, -0.6, -0.65(*CN*), -0.7, -0.75, -0.8, -0.9, -1.0, -1.1, -1.2, -1.4, -1.6 and -1.8 V. **(b)** ABC trilayer graphene by SiO$_2$ back gate with *CN* point at V = 40 V. **(c)** ABC trilayer graphene by electrolyte top gate with *CN* point at V = 0.05 V. In (b) and (c), the spectra are displaced for 2 units, with the gate voltages V denoted on the spectra. The arrows are guides of peak positions.

In contrast, ABC trilayer shows very different conductivity spectra and distinct

electric-field response [Figure 6.2(b, c)]. At V_{CN}, ABC trilayer conductivity σ($\hbar\omega$) shows

a single peak at $\hbar\omega = 0.35$ eV, which is of much lower energy than the main transition energies $\hbar\omega = 0.53$ and 0.60 eV in ABA trilayer. This reflects the different low-energy band structures in ABA and ABC trilayers due to the distinct nature of their interlayer interactions. As we increase V (electron side) in ABC trilayer, its behaviors stand in sharp contrast with those of ABA trilayers. We observed that the amplitude of transition increases and the main peak splits into two peaks *P1* and *P2*. The two new peaks shift in opposite directions and broaden with increasing the gating bias. Corresponding effects are also observed in the hole side [Figure 6.2(b)]. We note that the transition peaks in ABC trilayer is much narrower than those observed in bilayer [16] due to the singularity of density of state at the band edges of ABC trilayer.

6.4 Analysis based on Tight-Binding Models

6.4.1 Simulation of Conductivity in ABC Trilayer

The observed distinct infrared response from ABA and ABC trilayers indicates that the applied field modifies their band structure and electronic excitations in different ways. We have analyzed our data in the framework of TB model with suitable hopping parameters. Figure 6.2(a) presents a schematic description of the electronic structure of ABC trilayer graphene under electric field based on a TB calculation with γ_0 and γ_1. In the absence of an applied field (dashed red line), the ABC trilayer has three valence (*v1, v2, v3*) and conduction (*c1, c2, c3*) bands near the K point in the Brillouin zone. Two of them (*v1, c1*) lie in the low energy range and touch one another at a Fermi point, while the other bands are separated away by ~300 meV. The transitions between the two low-lying bands (*v1, c1*) and the four other bands (*v2, v3, c2, c3*) give the main peak of

conductivity at $\hbar\omega$=0.35 eV. With the application of a strong electric field, the electronic structure of ABC trilayer graphene changed significantly (green solid line). A gap develops between valence band *v1* and conduction band *c1*. The absorption peak *P1* and *P2* observed in experiment are readily understood as originated from the transition 1 and 2 in the modified band structure.

For a quantitative comparison with the experiment, we have calculated the ABC band structure at different doping charge density *n*. We considered by a self-consistent calculation the different potentials at different layers induced by the uneven charge distribution in graphene trilayer under a single gate. In the TB calculation, we considered only the dominant terms γ_0 = 3.4 eV (corresponds to υ_F=1.1x10^6 ms^{-1}) and γ_1 = 377 meV, because by carrying out a full-parameter TB calculation we did not find any significant influence of other TB parameters in explaining the main features of our data. In this case the electron-hole symmetry was implicitly assumed. To obtain a best fit on the data, we assumed a capacitance of the electrolyte top gate C = 1.3 μFcm^{-2}. In our calculation, the predicted band gap E_g and the energy gap at the *K* point ΔE_k agreed well with the band gap extracted from experimental data [Figure 6.3(b)]. For more detailed and direct comparison, we simulated the IR conductivity spectra by means of Kubo formula. A phenomenological broadening of 20 meV was adopted. The simulation [Figure 6.3(c)] is seen to capture the main features of the experimental spectra [Figure 6.2(b,c)]. We also show for comparison the predicted conductivity under the neglect of any induced modification of the electronic structure or band gap opening [Figure 6.3(d)]. The behavior is completely inconsistent with experiment.
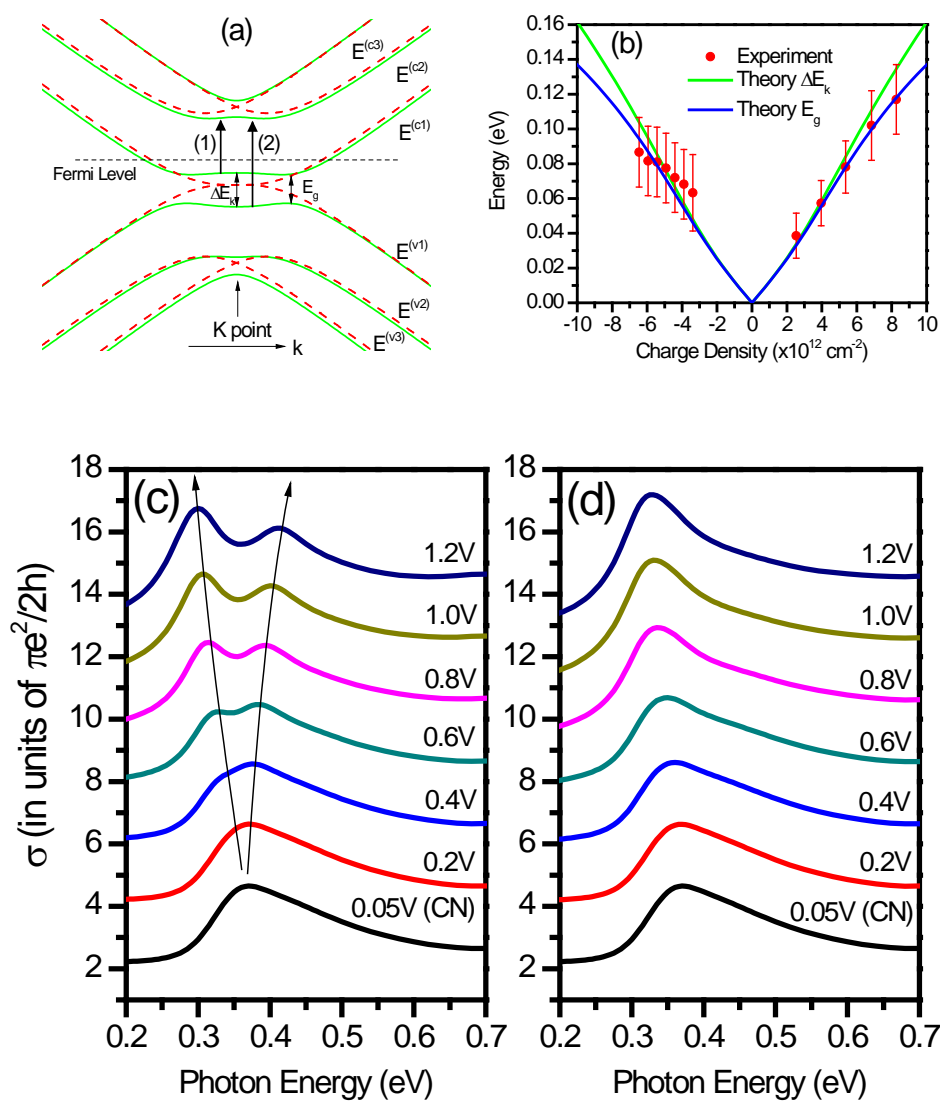
Figure 6.3 Band structure, energy gap and optical conductivity spectra of ABC trilayer graphene. **(a)** Band structure of ABC trilayer graphene with (green) and without (red) the presence of a perpendicular electric field as calculated within the TB model described in the text. Transitions 1 and 2 are the strongest optical transitions near the *K* point for electron doping. **(b)** Dependence of the energy gap at the *K* point (symbols) on the charge doping density of the ABC trilayer graphene. The error bars arise primarily from uncertainties in determining the peak position of the broad absorption features. The results of TB model for both ΔE_K and the band gap E_g are plotted as well to compare with the experimental data. The inset is a schematic of the ABC trilayer crystal structure. **(c,d)** Simulated spectra of the optical conductivity $\sigma(\hbar\omega)$ of gated ABC graphene trilayers with (c) and without (d) the band gap. The spectra are obtained from the Kubo formula for ABC graphene trilayer under the same doping as in Figure 6.2 (c). Panel (c) show the results obtained with the predictions of TB model for the electronic structure described in the text. For comparison, panel (d) is a reference calculation in which the ABC trilayer graphene band structure is assumed to remain unchanged (without an induced gap). In both panel (c) and (d), the spectra are displaced for 2 units, with the gate voltages *V* denoted on the spectra. The arrows are guide of peak positions.
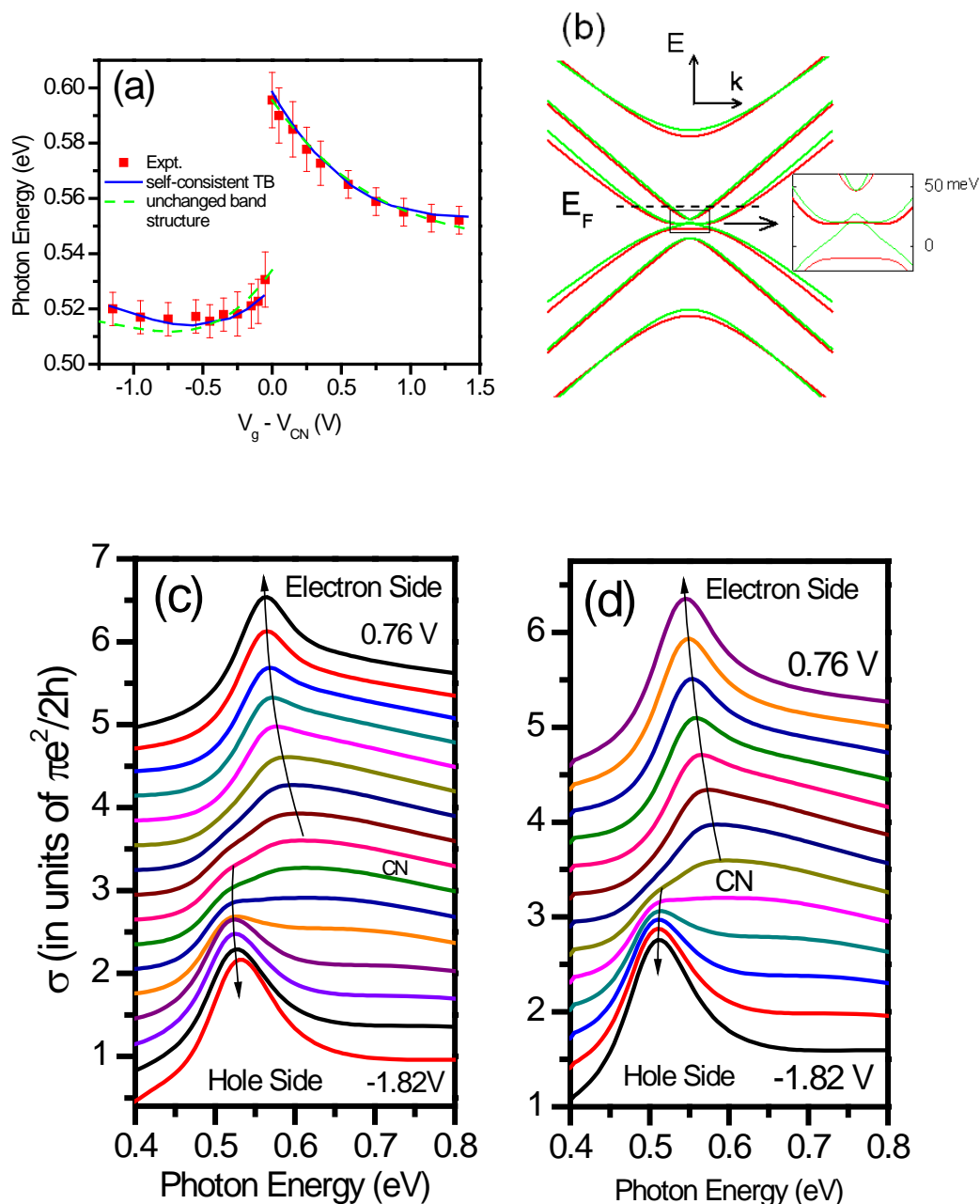
Figure 6.4 Comparison of optical conductivity $\sigma(\hbar\omega)$ with theory for ABA graphene trilayers at different gate voltages. **(a)** The conductivity peak positions as a function of gate voltage. The blue and green lines are peak positions extracted from the calculated spectra in (c) and (d), respectively. **(b)** The inset is the ABA trilayer graphene band structure with (green) and without (red) considering the parameters δ and γ_4. **(c)** The calculated conductivity spectra $\sigma(\hbar\omega)$ by the Kubo formula. The spectra are displaced for 0.3 units. The gate voltage V varies from top to bottom as: 0.76, 0.52, 0.21, 0.06, -0.08, -0.34, -0.47, -0.59, -0.65 (*CN*), -0.71, -0.83, -0.96, -0.80, -1.36, -1.51 and -1.82 V. The arrows are guides of peak positions. **(d)** Similar plot as in (c), but with an unchanged band structure in all applied gate voltages.

6.4.2 Simulation of Conductivity in ABA Trilayer

The simple TB description with only γ_0 and γ_1 is not sufficient, however, to describe the ABA trilayer IR conductivity spectra that exhibit a significant electron-hole (*e-h*) asymmetry. We attribute the *e-h* asymmetry to the difference between the valence and conduction bands, as previously shown in the study of bilayer [19,20]. According to the TB diagram of ABA trilayer (Figure 1.12), the sites A1, B2, A3 and B1, A2, B3 possess different on-site energies (δ) due to the different crystal field environment. This leads to different transition energies at the electron and hole side. Also, the interlayer next-nearest-neighbor coupling parameter γ_4 induces different dispersions for the conduction and valence bands, which are responsible to the different evolutions of the electron and hole transition peaks with the gate voltage. The effects of δ and γ_4 on the ABA trilayer energy bands are demonstrated in the inset of Figure 6.4 (b).

The observed *e-h* asymmetry in ABA trilayer can be understood quantitatively by a TB model with γ_0, γ_1, δ and γ_4. We have simulated the ABA trilayer IR conductivity by means of Kubo formula with a 20-meV phenomenological broadening and the self-consistent charge distribution. We found that the main features of the experimental conductivity spectra and the transition energies can be reproduced by γ_1=370 meV, δ=37meV and γ_4=170 meV [Figure 6.4 (a, c)]. These values are determined, respectively, by the transition peak position, peak separation and the peak shift with an assumed value of γ_0=3.4 eV. We have used a top-gate capacitance $C = 0.9$ μFcm^{-2} to obtain the best description of the data. The band structure in Figure 6.4 (b) corresponds to a gate voltage of $V = 0.9$ V. The energy bands shows essentially no gap (<2meV) for the case with γ_4 and δ. For comparison, we also did the simulation with an unchanged band structure of

ABA trilayer using the same TB parameters [Figure 6.4 (d)], *i.e.* assuming zero potential at all graphene layers for all gate voltages. The prediction did not show any significant deviations from the experimental data and the previous simulation [green lines in Figure 6.4 (a)], indicating our experimental results did not reveal any significant change in the band structure of ABA trilayer.

6.4.3 Comparison of Band Gap Opening in ABA and ABC Trilayers

Our analysis revealed markedly different capability of opening a band gap in ABA and ABC trilayers. We have derived the electric field between the 1st and 2nd layer E_{12} and between 2nd and 3rd layer E_{23}. The gate voltage V=1.2 V (n=8.3x10^{12} cm^{-2}) in the ABC sample produces E_{12}=0.25 V/nm and E_{23}=0.14 V/nm, and V = 0.9 V (n = 7.2 x 10^{12} cm^{-2}) in the ABA sample produces E_{12}=0.26 V/nm and E_{23}=0.08 V/nm. While the applied electric fields are of similar strength on both samples, the ABC trilayer shows a sizable band gap of ~ 120 meV and measurements in the ABA trilayer does not reveal any signature of band-gap opening.

We may understand the different behaviors of ABA and ABC trilayer graphene by considering their distinct crystal structures (Figure 1.11). Their tendency to open a band gap can be evaluated by considering the energy states near the *K* point in the Brillouin zone, where the intralayer coupling is small and can be neglected (Figure 1.12) [12]. For ABA trilayer with mirror symmetry, in a simply TB description with only γ_0 and γ_1, the energy states at the *K* point can be described as a combination of one trimer (the blue atoms) and three non-bonding monomers, *i.e.*, isolated atoms (yellow atoms). The trimmer has three states, the bonding and anti-bonding states with finite energy, and

the non-bonding state with zero energy. The zero energy level in ABA trilayer is then four-fold degenerate (three monomer states and one non-bonding trimer state). With the application of an electric field, the degeneracy of the two monomer states at A1 and A3 are lifted as they have different potentials. The degeneracy of the non-bonding trimer state and the monomer state at B2 is, however, hardly affected because their energies remained unchanged in a uniform electric field. The degeneracy may only be slightly lifted up for non-uniform electric field, because the asymmetric perturbation on the trimer causes the energy of the non-bonding trimer state to shift. The robustness of the degeneracy against the electric field makes the band gap opening difficult. The case in ABC trilayer with inversion symmetry is different. As shown in the TB diagram of ABC trilayer (Figure 1.12), the zero-energy K-point states consist of two non-bonding monomers (yellow atoms). The two-fold degeneracy can be readily lifted up with the application of an electric field because the two monomers are located at different potentials. This explains the sizable band gap induced in ABC trilayer.

6.4.4 Comparison of Electron-Hole Asymmetry in ABA and ABC Trilayers

Finally we comment on the significant band structure asymmetry in ABA trilayer graphene. We observed a 70-meV difference between the electron and hole transition peaks at the charge neutrality point V_{CN}, which corresponds to $\delta = 37$ meV in the TB calculation. On the other hand, we observed only a single peak in ABC trilayer at V_{CN}. From the width of the peak (~44 meV), we can restrict the value of δ to be < 22 meV in ABC trilayer, which is comparable to that observed in bilayer ($\delta = 18\text{-}25$ meV) [16,19]. The different e-h asymmetry of ABA and ABC trilayer should arise from their different

crystal structures. Since the on-site energy difference δ arises from the change of local crystal field by the interlayer coupling, a trimer with two interlayer bonds should have a larger value of δ than a dimer with only one interlayer bond. The ABA trilayer with a trimer therefore has a larger *e-h* asymmetry than bilayer and ABC trilayer that have the dimers.

6.5 Conclusion

In conclusion, we observed distinct IR response on ABA and ABC trilayer graphene under the application of a strong electric field. ABC trilayers exhibited a sizable band gap, which was not observable in ABA trilayer. On the other hand, ABA trilayer showed a more prominent band structure asymmetry than ABC trilayer. These behaviors could be explained by considering their different crystallographic structures. Our work revealed the significant effect of stacking order on the properties of trilayer graphene and demonstrated the opening a band gap in trilayer graphene. It should inspire new research on FLG that has more flexibility in electronic structure due to the large variations of their stacking sequences.

References

[1] A. A. Avetisyan, B. Partoens & F. M. Peeters. "Electric field tuning of the band gap in graphene multilayers", *Phys. Rev. B 79*, 035421, (2009).

[2] H. K. Min & A. H. MacDonald. "Electronic Structure of Multilayer Graphene", *Progress of Theoretical Physics Supplement 176*, 227, (2008).

[3] F. Guinea, A. H. C. Neto & N. M. R. Peres. "Electronic states and Landau levels in graphene stacks", *Phys. Rev. B 73*, 245426, (2006).

[4] F. Guinea, A. H. Castro & N. M. R. Peres. "Electronic properties of stacks of graphene layers", *Solid State Commun. 143*, 116, (2007).

[5] T. Ohta, A. Bostwick, J. L. McChesney, T. Seyller, K. Horn & E. Rotenberg. "Interlayer interaction and electronic screening in multilayer graphene investigated with angle-resolved photoemission spectroscopy", *Phys. Rev. Lett. 98*, (2007).

[6] E. McCann & M. Koshino. "Spin-orbit coupling and broken spin degeneracy in multilayer graphene", *Phys. Rev. B 81*, 241409, (2010).

[7] S. Latil & L. Henrard. "Charge carriers in few-layer graphene films", *Physical Review Letters 97*, 036803, (2006).

[8] M. Koshino. "Interlayer screening effect in graphene multilayers with ABA and ABC stacking", *Phys. Rev. B 81*, 125304, (2010).

[9] A. A. Avetisyan, B. Partoens & F. M. Peeters. "Electric-field control of the band gap and Fermi energy in graphene multilayers by top and back gates", *Phys. Rev. B 80*, 195401, (2009).

[10] A. A. Avetisyan, B. Partoens & F. M. Peeters. "Stacking order dependent electric field tuning of the band gap in graphene multilayers", *Phys. Rev. B 81*, 115432, (2010).

[11] J. L. Manes, F. Guinea & M. A. H. Vozmediano. "Existence and topological stability of Fermi points in multilayered graphene", *Phys. Rev. B 75*, 6, (2007).

[12] M. Aoki & H. Amawashi. "Dependence of band structures on stacking and field in layered graphene", *Solid State Commun. 142*, 123, (2007).

[13] F. Zhang, B. Sahu, H. Min & A. H. MacDonald. "Band structure of ABC -stacked graphene trilayers", *Phys. Rev. B 82*, 035409, (2010).

[14] Ma, ntilde, J. L. es, F. Guinea, M. Vozmediano, iacute & A. H. a. "Existence and topological stability of Fermi points in multilayered graphene", *Physical Review B 75*, 155424, (2007).

[15] Y. B. Zhang, T. T. Tang, C. Girit, Z. Hao, M. C. Martin, A. Zettl, M. F. Crommie, Y. R. Shen & F. Wang. "Direct observation of a widely tunable bandgap in bilayer graphene", *Nature 459*, 820, (2009).

[16] K. F. Mak, C. H. Lui, J. Shan & T. F. Heinz. "Observation of an Electric-Field-Induced Band Gap in Bilayer Graphene by Infrared Spectroscopy", *Phys. Rev. Lett. 102*, 256405, (2009).

[17] M. Koshino & E. McCann. "Gate-induced interlayer asymmetry in ABA-stacked trilayer graphene", *Phys. Rev. B 79*, 125443, (2009).

[18] M. F. Craciun, S. Russo, M. Yamamoto, J. B. Oostinga, A. F. Morpurgo & S. Thrucha. "Trilayer graphene is a semimetal with a gate-tunable band overlap", *Nat. Nanotechnol. 4*, 383, (2009).

[19] Z. Q. Li, E. A. Henriksen, Z. Jiang, Z. Hao, M. C. Martin, P. Kim, H. L. Stormer & D. N. Basov. "Band Structure Asymmetry of Bilayer Graphene Revealed by Infrared Spectroscopy", *Phys. Rev. Lett. 102*, 4, (2009).

[20] L. M. Zhang, Z. Q. Li, D. N. Basov, M. M. Fogler, Z. Hao & M. C. Martin. "Determination of the electronic structure of bilayer graphene from infrared spectroscopy", *Phys. Rev. B 78*, 11, (2008).

Chapter 7

Probing Out-of-Plane Vibrations in Few-Layer Graphene using Combinational and Overtone Raman Modes

In the previous chapter, we have investigated how the stacking order influences the electronic band structure as well as the electric-field response of few-layer graphene (FLG). In this chapter, we investigate the influence of stacking order on the out-of-plane Raman response in FLG. As the out-of-plane phonons are usually of low energy, which makes the measurements difficult, we probe the vibrations through their overtone and combinational Raman modes. We observed higher-order Raman features, appearing at ~ 1660, 1730 and 1760 cm^{-1}, in FLG for both Bernal and rhombohedral stacking. Using double-resonance theory, we have identified the features, respectively, as the LO+ZA, LO+ZO' combinational modes and the 2ZO overtone mode, where LO, ZA, ZO, and ZO' denote, respectively, the in-plane longitudinal optical mode, the out-of-plane acoustic, optical and layer-breathing modes. All the Raman features are absent in single-layer graphene (SLG), which lacks ZO' mode and ZA and ZO modes are not Raman active. The LOZO' Raman spectra depend on the stacking order of the layers and thus serve for identifying stacking order in FLG.

7.1 Introduction

Raman spectroscopy has been a powerful tool to investigate the vibrational and electronic properties of graphene. Most of the Raman research has been directed to exploration of the in-plane phonon modes such as the G, 2D (or G') and D modes [1,2], since the corresponding Raman signals are strong. In particular, 2D band spectra are useful for characterizing the layer thickness of FLG since several different wave numbers q are selected for a dispersive phonon mode so as to satisfy the double resonance Raman condition for FLG. However, in-plane phonon dispersion is not sensitive to the stacking order of FLG because of the weak interlayer interaction. An analysis of stacking order on FLG with layer number greater than four is not well established. On the other hand, since out-of-plane phonon dispersion is sensitive to stacking order such as the layer-breathing mode (ZO') in which the distance between the adjacent graphene layers is vibrating, Raman spectroscopy for the out-of-plane phonon modes is of interest though the signal is generally weak. Although the out-of-plane vibrations of a SLG are not Raman active, we can observe weak Raman signal when the symmetry of lattice structure is lowered. For example, in the case of carbon nanotube (CNT) [3], because of the curvature of cylindrical surface, the overtone of the out-of-plane optical (ZO or iTO) phonon which they call M-mode at ~1750 cm^{-1} has been observed. In the case of FLG, since Bernal (ABA) or rhombohedra (ABC) stacking or turbostratic structure for folded graphene has lower symmetry than that for SLG, we expect Raman signal of out-of-plane phonon modes which is useful for characterizing graphene sample.

In this chapter, we identify the out-of-plane acoustic (ZA), optical (ZO) and layer-breathing (ZO') modes in graphene layers using their Raman overtone and combination modes in double resonance conditions. We observed three prominent Raman lines at

~1660, 1730 and 1760cm^{-1} with the excitation of 532-nm laser. In particular, we confirmed that these Raman features are absent in SLG. Their frequencies show a significant dispersion with the excitation laser energy. By detailed analysis based on double-resonance theory, these three Raman features are assigned as the LO+ZA, LO+ZO' combinational mode and 2ZO overtone mode, respectively, where LO denotes the longitudinal optical mode. The bilayer graphene (BLG) layer-breathing mode (ZO') dispersions extracted from the combinational LOZO' mode and from the overtone 2ZO' mode are found to match well with one another and with the theoretical predictions. This demonstrates that the combinational and overtone modes in graphene can be used as effective probes to the low-energy out-of-plane phonon branches. For FLG with thickness from 3 to 6 layers, the LOZO' lines in samples with Bernal (ABA) and rhombohedral (ABC) stacking order show unique spectral shapes. In fact, the LOZO' band in ABA samples is split into several well-separated narrow bands in ABC samples. Thus the LOZO' Raman mode can be used as an accurate means of identifying the stacking order in FLG.

7.2 Experiment

The graphene samples which was exfoliated from kish graphite (Toshiba) were deposited on quartz substrates with pre-patterned trenches (width and depth of 4 μm) [4]. The suspended parts over the trenches were thus isolated from any perturbations of the substrates. For comparison, we have also studied graphene samples supported on bulk SiO$_2$ and SiO$_2$(300nm)/Si substrates. The samples were characterized first by infrared spectroscopy to determine the layer thickness and stacking order [5,6]. In this experiment,

we made use of graphene samples with layer number from 1 to 6 with both Bernal and rhombohedral stacking order. The Raman measurements were carried out in ambient conditions, using a Horiba Raman confocal microscope equipped with a spectrometer and a cooled charged-coupled-device (CCD) array. We used laser excitation with photon energies over a wide spectral range from visible to near-infrared, including wavelengths (energies) at 488 nm (2.54 eV), 532 nm (2.33 eV), 594 nm (2.09 eV), 633 nm (1.96 eV) and 785 nm (1.58 eV). In order to obtain weak signals, we measured the signal for over one hour with the laser power below 3mW in order to avoid the heating effect. In fact, Raman shift changed within 1 cm^{-1} for laser power from 0.3 to 3 mW for samples supported on bulk SiO_2. Figure 7.1 shows the G- and 2D-mode Raman spectra of free-standing SLG, BLG and bulk graphite with laser excitation wavelength at 532 nm. Due to the absence of any substrate-induced doping and impurity scattering, the SLG spectrum has a larger 2D/G ratio, a broader G mode and an asymmetric 2D mode compared to the spectrum of supported SLG samples [4]. The free-standing samples also allow us to see clearly the multiple peaks in the 2D mode of BLG.
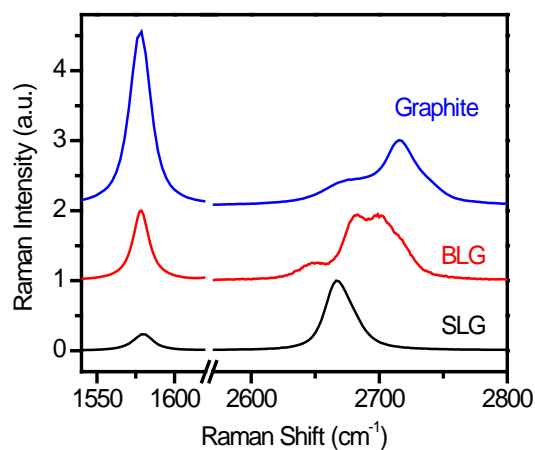

Figure 7.1 G- and 2D-mode Raman lines of free-standing SLG, BLG and bulk graphite.
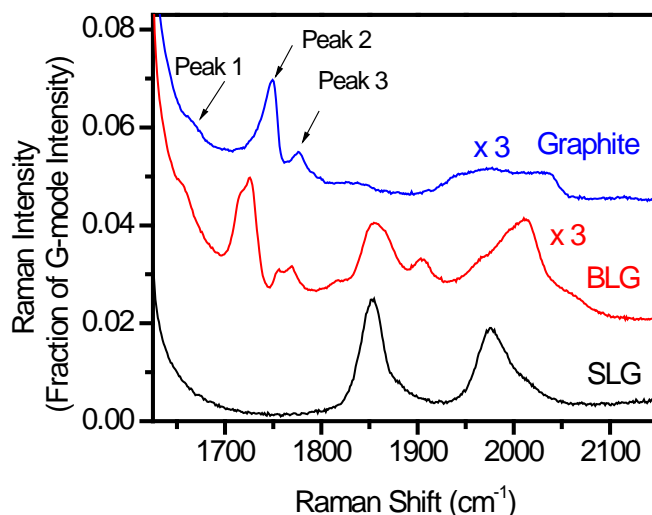
Figure 7.2 Raman modes in the frequency range of 1625 to 2150 cm^{-1} for free-standing SLG and BLG and bulk graphite with 532-nm excitation. The spectra are normalized with the respect to the G-mode peak intensity. The spectra of BLG and graphite are magnified by a factor of 3 and displaced by 0.02 for clarity.

7.3 Graphite

In Figure 7.2 we show Raman features which are normalized by G-band intensity for SLG and BLG and graphite samples, in the frequency range of 1625 to 2100 cm^{-1}. The Raman intensity in this frequency range is two orders of magnitude smaller than that for G mode. Their lineshapes differs significantly in samples with different layer thickness. In graphite, we observe a multi-featured band at 1750 cm^{-1} that shows an "M" shape, and a broad band at 1900-2050 cm^{-1}. They have been previously denoted as the M mode and the combinational ZO+LA mode, respectively [3]. In addition, we observe a small peak at 1660 cm^{-1}, which has not been reported before. This peak, while subtle in supported FLG and graphite samples, becomes more prominent on suspended FLG. For

convenience, we temporally denote the small peak at 1660 cm^{-1} and the low- and high-energy peaks of the "M"-shape feature as Peak 1, 2 and 3, respectively.
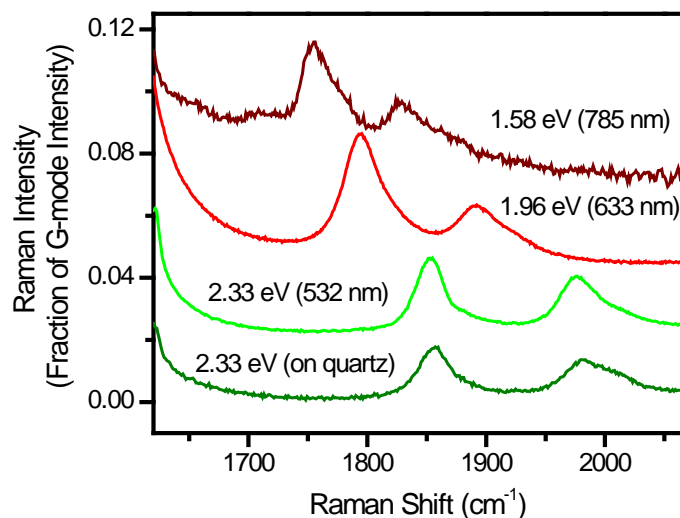

Figure 7.3 Raman modes in the frequency range of 1625 to 2050 cm^{-1} for free-standing SLG at excitation photon energies (wavelengths) of 2.33 eV (532 nm), 1.96 eV (633 nm) and 1.58 eV (785 nm). The spectra are normalized with the respect to the G-mode peak intensity. To evaluate the substrate effect, the spectrum of an SLG sample supported on quartz surface at 532-nm excitation is also plotted. As the substrate broadens the G-mode feature, this spectrum is normalized so that its G line has the same integrated intensity as that of the free-standing SLG. The spectra are displaced by 0.04 for clarity.

7.4 Single-Layer Graphene

As shown in Figure 7.2, the Raman peaks 1-3 are not observable for SLG. One may argue that Peaks 1-3 may have been shifted and hidden in the two peaks at 1800-2050 cm^{-1}, or perhaps the later two peaks are themselves the shifted "M"- feature. To this end, we have examined the spectra of free-standing SLG with different excitation photon energies (Figure 7.3). As the laser energy increases from 1.58 eV (785 nm) to 2.33 eV (532 nm), the two peaks blue-shift from 1755 to 1853 cm^{-1} and from 1827 to 1976 cm^{-1},

which correspond to an energy dependence of 130 and 200 cm^{-1}/eV, respectively. Such significant dispersions indicate that these two peaks are not related to the Raman Peaks 1-3, which exhibit much weaker dispersions as we will show later. From their dispersive behavior, we can indeed assign the high and low energy peaks as the combinational modes of TO (or LO) phonon and the LA and TA phonon, respectively [7,8]. With these two peaks shifted away, we do not observe any other peaks in 1800-2050 cm^{-1} range. We can therefore safely exclude the existence of Peaks 1-3 in free-standing SLG. Furthermore, we do not observe significant deviations between the spectra of free-standing SLG and supported SLG on quartz substrates, indicating that the absence of Peaks 1-3 is robust with the presence of a substrate.

7.5 Bilayer Graphene

While Peaks 1-3 are absent in SLG, they are observed in Bernal-stacked BLG (Figure 7.2). Since these higher-frequency Raman modes are understood as overtone or combinational modes, we can apply a double-resonance theory in which Raman signal can be seen on the phonon dispersion relation by changing the excitation photon energy [9,10]. In the measurement, we adopted samples supported on SiO$_2$ surface to avoid the laser heating effect. We find that the frequencies of Peaks 1-3 exhibit moderate dependence on the excitation photon energy [Figure 7.4 (a,b)]. Their dispersive behaviors, however, show unique slope for each peak. The frequency of Peak 3 remains largely unchanged for excitation energies below 2.09 eV, and red shifts slightly for higher energies. A linear fit shows an average energy dependence of -9 cm^{-1}/eV. In contrast,

Peak 1 and Peak 2 blue-shift significantly with increasing excitation photon energy, with average energy dependence of 39 and 30 cm^{-1}/eV, respectively.
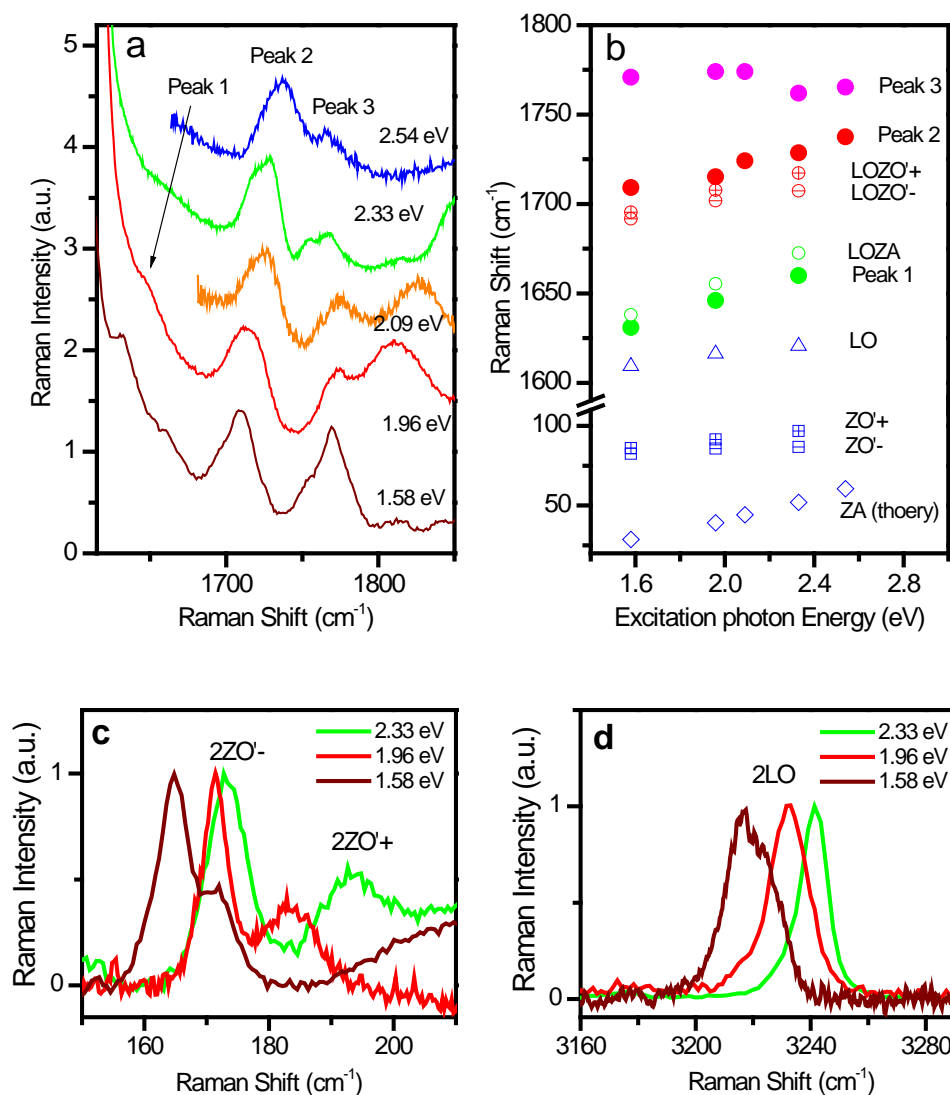

Figure 7.4 **(a)** Raman spectra of BLG in the range of ~1630 to 1850 cm^{-1} for different laser excitation energies. The spectra are displaced for clarity. The spectra show significant dispersions for the two peaks at ~1660 and 1750 cm^{-1}. We note that the strongly dispersed LO+TA band (~1810 cm^{-1} at 1.96-eV excitation) overlaps with Peak 1 at excitation photon energy of 1.58 eV. **(b)** The frequency of different peaks at (a) as a function of excitation photon energy. The solid dots are peak positions extracted from (a). Open dots are comparisons based on the combination of different lower-energy phonon modes. Open triangles and squares are the LO and ZO' phonon frequencies extracted by experiment. The open diamonds are ZA phonon frequency by theory. **(c,d)** The 2ZO'-mode (c) and 2LO(2D')-mode (d) Raman spectra of BLG for different laser excitation energies. The two peaks in the 2ZO' spectra are denoted as 2ZO'+ and 2ZO'-.

Peak 3 is assigned to the overtone of ZO (or oTO) phonon ($\sim$885cm^{-1}) because both its frequency and energy dependence match the ZO phonon branch that shows a slight negative dispersion with increasing phonon momentum from the Γ-point. The same assignment has been made on the corresponding Raman mode in CNT (the so-called M-mode) [3]. On the other hand, we assign Peak 1 and Peak 2 as the LO+ZA, LO+ZO' combinational modes of near-Γ-point phonons (intra-valley scattering), respectively. If we use this combination of two phonons, we can explain dispersive nature of the three peaks adequately. In the case of SLG, we cannot see LO+ZA or 2ZO mode because ZA and ZO phonons are not Raman active. Furthermore, LO+ZO' should not be observed in SLG because ZO' mode requires more than two graphene layers.

In order to confirm the phonon dispersion of ZO' mode experimentally, we have measured the overtone of ZO' mode (2ZO' mode) and the overtone of LO mode (the so-called 2D' mode) in BLG [Figure 7.4 (c,d)]. The 2ZO' mode was measured by using free-standing BLG samples in an argon-purged environment, which avoided the large Raman background of the substrate and the rotational Raman lines of air molecules in the frequencies below 200 cm^{-1}. We find that both 2ZO' and 2LO modes exhibit excitation-energy dependence due to the double-resonance mechanism. In particular, we observe two components (2ZO'+ and 2ZO'-) in the 2ZO' line, which we attribut to resonances between different electronic bands in BLG. We obtain the LO and ZO' phonon energies as half of their overtone values [triangles and squares in Figure 7.4(b)]. We find that the combination of a LO phonon and a ZO' phonon [open red dots in Figure 7.4(b)] matches well with the frequency and dispersion of Peak 2, therefore confirming our assignment of Peak 2 as the LO+ZO' mode. The peak 3 is assigned to the combination LO+ZA mode.

Since the ZA phonon overtone mode is not accessible in our Raman experiment due to its low energy, we make use of the theoretical value of ZA phonon energy [11]. As shown in Figure 7.4(b), the LO+ZA combination (open green dots) matches well with the frequency and excitation-energy dependence of Peak 3 (solid green dots).

To substantiate the analysis, we have plotted the LO, ZO, and ZO' and ZA phonon energies obtained from their overtone modes as a function of phonon momentum, and compared them with the theoretical predictions (Figure 7.5) [11]. Because the
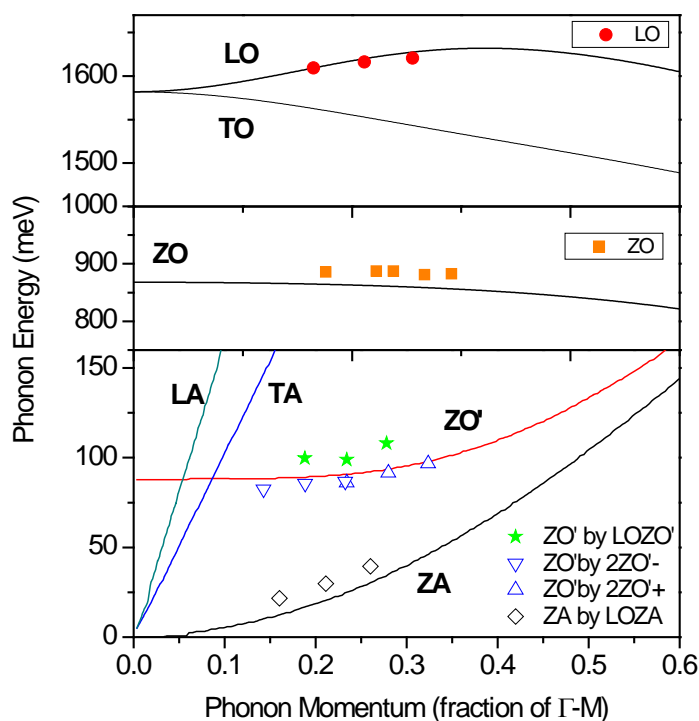

Figure 7.5 Comparison with experimental (symbol) and theoretical (lines) values of out-of-plane phonon dispersions. The red dots (orange squares) are LO (ZO) phonon dispersion from measurements of their overtone modes. The stars are the ZO' phonon energies obtained by subtracting the LO phonon frequencies (red dots) from the measured LOZO' phonon energies (Peak 2 in the Figure 7.4). The phonon momenta are taken as the average of the dominant intraband transition momenta in both the high and low lying electronic conduction bands in BLG. The open triangles are ZO' phonon dispersion derived from the 2ZO' overtone mode in BLG [Figure 7.4(c)]. The phonon momenta for ZO'+ and ZO'- are taken as the dominant transition momenta in the low and high lying electronic bands, respectively.

double-resonance process in BLG involved intra- and inter-valley transitions in both the low and high lying electronic conduction bands, we estimate the effective phonon momenta by averaging the transition momenta in different resonance processes for LO and ZO mode. For ZO' mode, we use intra-band transition momenta in low- and high-lying conduction bands as the phonon momenta for the ZO'+ and ZO'- bands, respectively. We also present the ZO' phonon dispersion obtained by subtracting the LO phonon energies from the LOZO'-mode energies. We obtain a good agreement between the experimental and theoretical values of these out-of-plane phonon modes.

7.6 Few-Layer Graphene

Since the 2ZO, LOZO' and LOZA lines are absent in SLG and activated by interlayer coupling, their behaviors should be sensitive to the nature of the interlayer interaction. To this end, we have measured and compared their spectra for graphene samples with layer thickness $N = 2$ to 6, with both Bernal (ABA) and rhombohedral (ABC) stacking sequence (green and red lines, respectively, in Figure 7.6). While the 2ZO mode remains largely unchanged in all the samples, we find the LOZO' mode exhibits distinct lineshapes for samples with different layer thickness and stacking order.

For ABA FLG, the frequency of LOZO' line increases systematically with the layer thickness and approaches the bulk limit of graphite. In particular, the LOZO' frequency of BLG is much lower (~15 cm^{-1}) than those of other FLG. In addition, we observe the development of small sub-bands in FLG. As the layer number increases, the number of sub-bands increases, with frequencies blue-shifted towards the main peak, and the LOZO' lineshape eventually converges to the asymmetric lineshape in graphite.
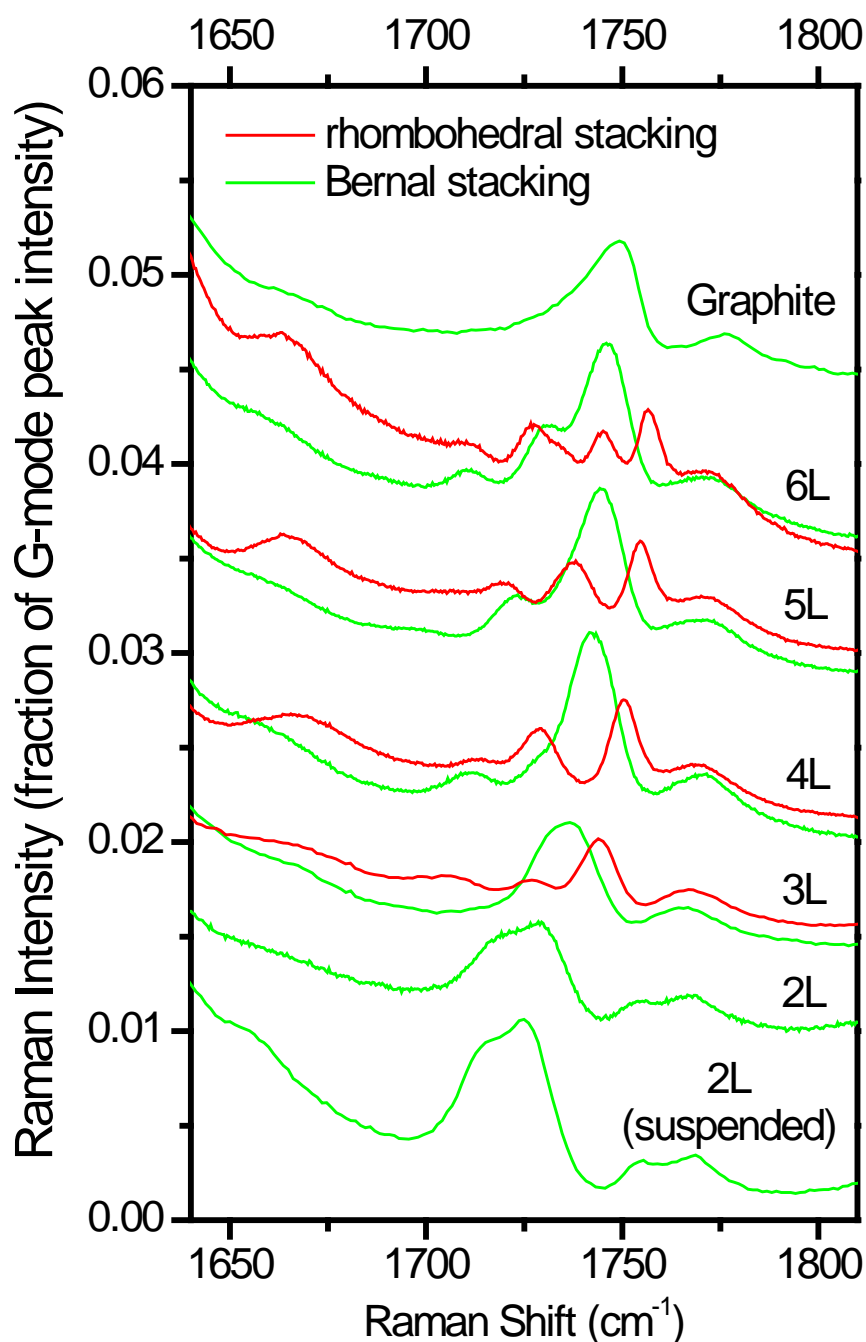
Figure 7.6 Raman spectra in the frequency range of 1640 to 1810 cm^{-1} for graphene samples of different layer thickness with Bernal (green line) and rhombohedral stacking order (red lines). The laser excitation wavelength is 532 nm. The samples were supported on SiO$_2$/Si substrates. The spectra were normalized with respect to the G-mode peak intensity. To evaluate the substrate effect, we also plot the spectrum for a suspended BLG. Because the G mode line becomes narrower in suspended samples, we normalize the suspended BLG spectrum so that the G-mode has the same integrated intensity as that of the supported BLG.

For ABC FLG, the LOZO' lines exhibit distinct lineshapes from those of ABA FLG. While the LOZO' mode appears to be a single band in ABA FLG, it is split into multiple bands in ABC FLG. The number of peaks tends to increase with the layer number. Their frequencies are found to evolve systematically as the layer number increases. On the other hand, the LOZA line at ~1660cm^{-1}, which is largely suppressed in ABA FLG, appears to be prominent in ABC FLG. These observations show that the LOZO' mode and LOZA mode are sensitive probes to the nature of interlayer interactions in FLG and provide us effective means to characterize the thickness and stacking order of FLG samples.

7.7 Substrate and Curvature Effects

Finally, we want to comment on the substrate and curvature effects on these Raman features. We have compared the 2ZO, LOZO' and LOZA lines on supported and suspended BLG samples (Figure 7.6). While their frequencies are not influenced by the substrate, the intensity drops significantly with the presence of a substrate. For instance, the LOZA mode at 1660 cm^{-1} is strongly suppressed in supported samples but prominent in suspended samples. We attribute this to the damping effect of substrate on the out-of-plane vibrations. Also, we want to note that the 2ZO mode has also been observed in single-wall CNTs, i.e. a rolled SLG [3], and its intensity is found to increase with decreasing CNT diameter. Therefore, beside inter-layer interaction, the out-of-plane Raman modes can also be activated by curvature on the graphene plane. These observations indicate that the out-of-plane Raman modes can be sensitive probes to both the interlayer coupling and curvature in the graphene plane.

7.8 Conclusion

In conclusion, we have assigned three dominant Raman features in the frequency range of 1630-1800 cm^{-1} as 2ZO, LOZO' and LOZA mode. These out-of-plane combination and overtone Raman modes were found to be absent in SLG due to its particularly crystal symmetry and lack of layer-breathing vibrations. The lineshape of LOZO' mode in FLG show dramatic dependence on the layer thickness and stacking order, and hence, can serve as an accurate stacking order indicator for FLG.

References

[1]   A. C. Ferrari. "Raman spectroscopy of graphene and graphite: Disorder, electron-phonon coupling, doping and nonadiabatic effects", *Solid State Commun. **143***, 47, (2007).

[2]   L. M. Malard, M. A. Pimenta, G. Dresselhaus & M. S. Dresselhaus. "Raman spectroscopy in graphene", *Physics Reports **473***, 51, (2009).

[3]   V. W. Brar, G. G. Samsonidze, M. S. Dresselhaus, G. Dresselhaus, R. Saito, A. K. Swan, Uuml, nl, M. S., B. B. Goldberg, A. G. Souza Filho & A. Jorio. "Second-order harmonic and combination modes in graphite, single-wall carbon nanotube bundles, and isolated single-wall carbon nanotubes", *Phys. Rev. B **66***, 155418, (2002).

[4]   S. Berciaud, S. Ryu, L. E. Brus & T. F. Heinz. "Probing the Intrinsic Properties of Exfoliated Graphene: Raman Spectroscopy of Free-Standing Monolayers", *Nano Lett.* **9**, 346-352, (2008).

[5]   K. F. Mak, M. Y. Sfeir, J. A. Misewich & T. F. Heinz. "The evolution of electronic structure in few-layer graphene revealed by optical spectroscopy", *Proc. Natl. Acad. Sci. U. S. A. **107***, 14999, (2010).

[6]   K. F. Mak, J. Shan & T. F. Heinz. "Electronic Structure of Few-Layer Graphene: Experimental Demonstration of Strong Dependence on Stacking Sequence", *Phys. Rev. Lett. **104***, 176404, (2010).

[7]   R. Rao, R. Podila, R. Tsuchikawa, J. Katoch, D. Tishler, A. M. Rao & M. Ishigami. "Effects of Layer Stacking on the Combination Raman Modes in Graphene", *ACS Nano*, preprint, (2011).

[8]   C. Cong, T. Yu & R. Saito. "Second-order Overtone and Combinational Raman Modes of Graphene Layers in the Range of 1690 cm^{-1} to 2150 cm^{-1}", *arXiv:1010.3391v1*, (2010).

[9]   C. Thomsen & S. Reich. "Doable resonant Raman scattering in graphite", *Phys. Rev. Lett. **85***, 5214, (2000).

[10]   R. Saito, A. Jorio, A. G. Souza Filho, G. Dresselhaus, M. S. Dresselhaus & M. A. Pimenta. "Probing Phonon Dispersion Relations of Graphite by Double Resonance Raman Scattering", *Phys. Rev. Lett.* **88**, 027401, (2001).

[11]   L. J. Karssemeijer & A. Fasolino. "Phonons of graphene and graphitic materials derived from the empirical potential LCBOPII", arXiv:1010.5594v1011, (2010).